Turbulence Generated in a Multi-Fan Wind Tunnel

Austin L'Ecuyer

Department of Mechanical Engineering

McGill University
Montreal, Canada

December 2021

A thesis submitted to McGill University in partial fulfilment of the requirements of the degree of Master of Science.

Acknowledgements

First and foremost, I would like to thank my supervisor Professor Jovan Nedić for believing in my ability to conduct research and for his continued support during the completion of my degree. Thank you for guiding and pushing me to be better these past few years.

I would also like to express my gratitude toward the McGill Fluids Lab, Stephanie, Dimitri, Raphaël, Anushka, Dylan and Rubert for their assistance with the construction of the wind tunnel facility and being a fantastic lab group.

Moreover, I need to say a huge thank you to Pierre, Teresa, and Kara, my beloved family. I would also like to specifically thank Marie L'Ecuyer for her excellent abstract translation used in this thesis.

I would have never had the confidence to undertake this master's degree without the support of my best friends Adam, Justin, and Cory; you three have helped to make me the person I am today. I also want to give a big thank you to Charles and Annie for their kindness, and to the Champagne Cossette family for sharing their home during the completion of this thesis.

Finally, I wish to thank my loving girlfriend Jasmin for always being there for me and for being my rock throughout this thesis and during the strange time of COVID-19.

Financial support for this thesis work was provided by the *Fonds de Recherche du Québec – Nature et Technologies*, and the *Arbour Foundation*. Thank you.

Abstract

With the rise in popularity of unmanned aerial vehicles (UAVs), there is a need to test these vehicles in a laboratory setting. A Multi-fan wind tunnel (MFWT) facility has been developed and built at McGill for this purpose, and comprises of 81 small fans arranged in a 9-by-9 grid. A MFWT allows the user to create tailored flows with minimal pressure losses, due to the absence of screens and grids. The small fans used in the MFWT also have a fast dynamic response which can be modulated to mimic wind gusts or other naturally occurring wind phenomenon.

Before UAVs can be tested in the facility, the flow characteristics of the tunnel must be well documented, with the goal of creating well defined tailored flow fields. The scope of this study is to examine the baseline flow characteristics in the development region of the flow (the region near the wall of fans) and how the inlet conditions of the tunnel can be varied to create different conditions in the flow field.

Although dynamic modulation of the wind tunnels fans is possible, this study focuses on the static case where individual fans do not change speed while in operation. In addition to the baseline case with all fans on, different shear ratios of fans configured in a checkerboard pattern have been tested. The fans were wired in an alternating pattern and sent one of two inputs; with signal one and signal two wired to the fans in this alternating pattern, the fan wall resembles a checkerboard. The shear ratio is defined as the ratio of the velocities produced by the two fan signals, $S_r = U_{\text{high}}/U_{\text{low}}$, with the larger signal as the numerator (shear ratio is always greater to or equal to one).

A two-component hot-wire anemometer probe was mounted to a 3D traversing system inside of the tunnel to obtain the streamwise and transverse velocity components. Shear ratios from 1.00 to 3.50 were investigated, as well as the on-off case; all cases had a bulk

flow velocity of $5\,\mathrm{m\,s^{-1}}$. It is found that shear ratios larger than 1.00 produced a noticeable increase in the turbulence intensity, turbulent kinetic energy and integral length scale. At the closest and farthest measured points to the fan wall, an increase of 25.09 % and 14.75 % in turbulence intensity, respectively, was noted as the shear ratio was increased from 1.00 to 3.50 at each location. Critically, turbulence in the vicinity of the fans was found to exhibit *non-equilibrium* turbulent properties, whereby the non-dimensional dissipation coefficient C_ε was found to be approximately inversely proportional to the Taylor-scale based Reynolds number Re_λ (as opposed to *equilibrium* turbulence where C_ε = constant). Suggested scalings are proposed for the increase in turbulence intensity, and a similarity with traditional grid turbulence scaling is presented for the decay of the turbulent kinetic energy.

Résumé

Étant donné l'utilisation grandissante des drones, il devient nécessaire de tester ceux-ci en laboratoire. Dans ce but, une soufflerie à ventilateurs multiples a été conçue et construite à l'Université McGill. Cette installation comprend 81 petits ventilateurs disposés selon un montage matriciel 9 par 9. Une soufflerie à ventilateurs multiples permet de créer et d'adapter des écoulements dans lesquels les pertes de pression sont réduites au minimum par l'absence d'écrans et de grilles de préconditionnement. De plus, les petits ventilateurs utilisés dans ce type de soufflerie ont une réponse dynamique rapide qu'il est possible de moduler pour reproduire des rafales ou d'autres phénomènes naturels du vent.

Avant de pouvoir tester des drones dans la soufflerie, il faut d'abord déterminer les caractéristiques d'écoulement de l'installation, et ce, dans le but de créer des écoulements adaptés qui soient bien définis. La présente étude a pour objet d'examiner les caractéristiques initiales de l'écoulement dans la région où l'écoulement est généré (la région près du mur de ventilateurs) et de faire varier les conditions d'admission de la soufflerie pour créer diverses conditions dans l'écoulement.

Bien que les souffleries permettent de réaliser une modulation dynamique, cette étude se concentre sur le cas statique où la vitesse de chaque ventilateur ne varie pas en cours de fonctionnement. Le système a été testé à l'état initial où tous les ventilateurs sont en marche, ainsi qu'à différents degrés de cisaillement obtenus au moyen d'une configuration dans laquelle les ventilateurs ont reçu l'un de deux signaux (signal 1 ou signal 2) dans une alternance réalisant une figure en damier. Le rapport de cisaillement correspond au rapport des vitesses produites par les deux signaux imposés aux ventilateurs, $S_r = U_{\text{high}}/U_{\text{low}}$, le signal le plus fort étant le numérateur (le rapport de cisaillement est donc toujours égal ou supérieur à 1).

Une sonde anémométrique à fil chaud à deux composantes a été montée sur un dispositif de déplacement en 3D qui a été installé à l'intérieur de la soufflerie pour mesurer les composantes longitudinale et transversale de la vitesse. Le système a été testé à des valeurs de rapport de cisaillement allant de 1,00 à 3,50, ainsi que dans le cas où le signal 1 est émis et le signal 2 n'est pas émis; dans tous les cas, la vitesse d'écoulement est d'environ $5\,\mathrm{m\,s^{-1}}$. Les valeurs de rapport de cisaillement supérieures à 1,00 entraînent une augmentation notable de l'intensité de la turbulence, de l'énergie cinétique de la turbulence et de l'échelle intégrale longitudinale. Au point de mesure situé le plus près et au point de mesure situé le plus loin du mur de ventilateurs, une augmentation respective de 25,09 % et de 14,75 % de l'intensité de la turbulence est observée lorsque le rapport de cisaillement passe de 1,00 à 3,50 à chacun de ces deux points. Fait important, la turbulence à proximité des ventilateurs présente des propriétés hors équilibre; ce phénomène montre que le coefficient de dissipation adimensionnel C_ε est environ inversement proportionnel au nombre de Reynolds fondé sur l'échelle de Taylor «Re_λ»(par opposition à la turbulence en équilibre où C_ε est constant). Une équation adimensionnelle est donc proposée pour le calcul de l'augmentation de l'intensité de la turbulence, et une autre équation adimensionnelle, celle-ci fondée sur une équation existante, est proposée pour le calcul de la décroissance de l'énergie cinétique de la turbulence.

Contents

List of Figures

List of Tables

Chapter 1

Introduction

1.1 Background and Motivation

Jet arrays, and multi-fan wind tunnels (MFWTs) have been developed to afford the user the possibility of controlling the turbulent flows they create (Nishi et al., 1993; Teunissen, 1975). Traditional wind tunnels are driven by one large fan and contain flow-conditioning devices, such as a honeycomb or a mesh, to produce the desired flow characteristics; a particular goal in the majority of wind tunnels is for them to have as low a turbulence intensity as possible (Mehta and Bradshaw, 1979). Wind tunnel testing is especially useful for unmanned aerial vehicles (UAVs), since their complex geometries, paired with the proximity of their propellers, make drones difficult to model using computational fluid dynamics (CFD); wind tunnel testing is therefore an excellent alternative when CFD cannot be used (Barlow et al., 1999). In the case of UAVs, dynamic testing is needed when developing control algorithms. Owing to their large size, the large ramp-up and ramp-down time of large fans make them less suited for dynamic modulation of the wind, and thus can not be used to create unsteady wind conditions. Moreover, adding flow conditioning devices create pressure losses which can hinder the magnitude of the produced flow. Jet arrays and MFWTs avoid such issues by using many small flow generating sources that can be adjusted very fast. MFWTs have been chosen over jet arrays in this study because of their cost effectiveness, the fact that the fans RPM can be easily monitored through a built in tachometer, and because MFWTs have shown great promise in the literature.

In recent years unmanned aerial vehicles (UAVs), or informally drones, have exploded in popularity and the industry behind drones has been estimated to be worth over $100 billion (Goldman Sachs, 2018). In urban environments drones will experience sudden velocity changes as they pass by tall buildings, which act as bluff bodies, creating wakes, updrafts from exhaust vents, and other highly turbulent flow, changing flow conditions. The urban boundary layer (UBL) is the portion of the atmospheric boundary layer (ABL) which is influenced by an urban environment, such as a city. UAVs will experience high turbulence intensities when flying above rooftops in the UBL (Adkins et al., 2020). The presence of changing bluff body wakes and high turbulence intensities suggest there is a need for a method of testing UAVs to fly in these conditions. A MFWT is an ideal candidate to be used for testing drones under such conditions in a laboratory setting. The conditions of a produced flow field can be dynamically changed without bulky flow conditioning devices.

The majority of studies published to date on MFWTs have primarily focused on replicating the conditions seen in the atmospheric boundary layer (ABL) (Nishi et al., 1993). Replicating the ABL is critical in a variety of civil engineering applications, since tall building are exposed to the large turbulent length scales and high turbulence intensities present in the ABL. A significant body of research has been conducted in this field at the University of Miyazak into MFWTs (Nishi et al., 1997, 1999; Nishi and Miyagi, 1995; Ozono and Ikeda, 2018; Ozono et al., 2006), however, the turbulence generated in most of these studies is non stochastic, and has a time varying mean velocity profile. Further details on this will be presented in Chapter 2.

This study is concerning itself with creating 'calm' atmospheric conditions for testing UAVs. The conditions of interest are the large scale intensities and length scales present in the atmosphere. Experiments using this tunnel have indicated the tunnel is capable of generating decaying turbulence similar to the decaying grid turbulence that has been studied since the mid 1930's. Because grid turbulence has been very well studied, the decaying case would provide ample data for bench marking the test results once the measurements in the tunnel are taken. Usually simple grids of various sizes are used to generate simple isotropic turbulence; one goal of this study is to find out if this type of turbulence can be created in a MFWT without an obstruction of the flow i.e., the use of grids.

The main hypothesis of the present work is as follows; if a multi-fan wind tunnel is

configured in a checkerboard pattern (alternating the speed to one of two values between adjacent fans), it should be possible to generate tailored turbulence without blockages in the flow by simply increasing or decreasing the velocity ratio between the high and low signals given to the fan wall. It should then be possible to create a scaling that relates the turbulence parameters to the ratio of the initial velocities given to a fan wall configured in a checkerboard pattern.

1.2 Objectives of present work

The motivation for the present work started with the desire to create a UAV testing facility, whereby UAVs can be tested in both turbulent and dynamic/unsteady wind conditions. Although dynamic conditions are more prevalent when vehicles are flying in close formation or in the near wake of buildings, the case of a decaying turbulence can be used to characterise the vehicles' performance when flying in a head wind in the atmosphere. This study, being the first to use such a facility at McGill University, will focus on characterising the turbulence produced under steady conditions, with the hope of laying the groundwork for future studies on dynamic wind cases.

Because decaying turbulence has been well studied academically, this type of turbulence will be the starting point in classifying the type of turbulence the MFWT can produce. This is because the results obtained from the decaying case can be easily compared to the available literature on decaying grid turbulence which allows for the validation of the results. Up to this point, there has been very little information on a MFWTs ability to create decaying turbulence, with most studies focusing on the dynamic case, creating wind gusts and dynamics flows. This study hopes to fill this gap in knowledge while practically identifying the type of stochastic turbulence the tunnel can create at given initial fan settings. The initial conditions are quantified by the shear ratio, $S_r = U_{\text{high}}/U_{\text{low}}$, and is the ratio of the higher over the lower velocities produced by the fans receiving. The fans therefore receive one of two signals, and are wired in an alternating pattern to produce a checkerboard pattern as shown in Figure 3.11; the dark squares produce U_{high}, and the lighter squares produce U_{low}.

The thesis aims at addressing the following aspects:

1. Determine the mean flow properties McGill's newly constructed MFWT.
2. Evaluate the stream wise evolution of the turbulent field.
3. Determine what effect a change in shear ratio will have on the flow.
4. Determine a scaling law for the turbulent parameters as a function of the initial conditions.

1.3 Thesis Organization

This thesis is structured as follows. In Chapter 2, the basic theory of turbulent flows is presented, as well as an overview of some of the methods used to generate decaying turbulence. In Chapter 3 the equipment, measurement techniques and facilities used in this thesis are presented. Chapter 4 will provide an overview of the results, provide discussion on the key observations, and offer a potential scaling that can be used to help predict how changing the initial conditions of the fans will modify the resulting flow. Finally, Chapter 5 will present suggestions as to how research using the MFWT facility can progress, whilst Chapter 6 will summarize the results obtained in this study.

Chapter 2

Background & Literature Review

Creating a unified theory of turbulent flow has been puzzling physicists and engineers for decades. It is theorized that a better understanding of turbulence could help unify fluid dynamics and aid in proving that there exists a smooth solution to the Navier-Stokes equations, an unsolved Millennium Prize problem. Through an engineering lens, an application of interest is predicting the onset of turbulence, another problem the scientific community has yet to be completely solved. These problems are the motivation for researching turbulence in an experimental setting. The background knowledge explained here will be relied on for the presentation and discussion of the results obtained in the MFWT facility, as discussed in Chapter 4.

2.1 Statistical Nature of Turbulent Flow

Turbulent flows are random and chaotic in nature, and these flows represent the majority of flows observed in the natural world, (Tennekes and Lumley, 1972). The reason engineers in particular are interested in turbulence is because most fluids the population interacts with, such as air and water, are turbulent. Some examples of how turbulence effects modern engineering design can be seen in bridges, planes and cars. Bridges interact with turbulent water at their bases and turbulent air higher above, they need to account for vortex shedding from air passing over the structure and the energy of the water eroding the

bridges base. Airplanes interact with non laminar air flowing over their wings and turbulence has an effect on the comfort of the passengers on board. Lastly, modern F1 cars are very concerned with the levels of turbulence they see during a race, the cars create a wake race engineers call “dirty air”, this air with high levels of turbulence negatively affects the aerodynamics of cornering cars trapped behind the wake of other cars.

There is no complete definition of turbulence; the characteristics and properties of turbulent flows are generally agreed upon, and identifying turbulence is a case of "knowing it when you see it". Randomness, diffusive and dissipative are some of the characteristics of turbulent flows, (Tennekes and Lumley, 1972). If a flow is laminar, as the velocity increases, so do the instabilities of the flow. Once these instabilities overcome the viscous dissipation, the flow will become turbulent. In general, the Reynolds number, defined as

$$\mathrm{Re} = \frac{\overline{u}L}{\nu}\,, \tag{2.1}$$

is a good indicator of whether or not a flow is turbulent, with turbulence occurring at large Reynolds numbers. Note that the Reynolds number can be viewed as the ratio between inertial forces and viscous forces in a flow, where $\overline{u}$ is the mean velocity of the flow, L is some characteristic length scale, and ν is the viscosity of the fluid. For example, a mean air speed of $\overline{u}$ =5 m s^{-1} in a wind tunnel of 750 mm-by-750 mm($L = 0.75$m) would have a Reynolds number of $\approx 249,000$ at Normal Temperature and Pressure (NTP). There are a variety of Reynolds numbers one can define based on a variety of length and velocity scales that are pertinent to the flow under consideration. Some of these dimensionless numbers aid in the study of turbulence and will be explained later in this section. From this section onwards,when Reynolds number is referred to, assume either the Taylor-scale Reynolds number Re_λ, or the turbulence Reynolds number, Re_L is being referenced. These different Reynolds numbers will be explained later in this section but can be seen as a way of comparing different turbulent flows to one another, and how lab generated turbulent flows compare to flows seen in nature.

Several measurement techniques exist for measuring the velocity of a flow. Pitot tubes, for example, are very good at measuring the mean flow at a point in the flow field. The drawback of this technique is the damping of the velocity fluctuations as the pressure propagates from the pitot tube to the pressure sensor, usually connected by flexible tubing.

For the study of turbulence, the rapid fluctuations of a flow field must be measured to capture the small length-, and time-, scales present in the flow. A commonly used method for rapidly sampling the velocity of a flow is hot-wire anemometry, which consists of a thin, short wire supplied with a particular voltage to maintain a constant temperature via Joule heating. The wire is connected to a Wheatstone bridge configuration with a feedback amplifier that adjusts the voltage to maintain the temperature. As a fluid flows over the wire, energy is lost due to the heat transfer between the wire to the fluid and hence the temperature of the wire changes. This then results in the voltage being supplied to the bridge to change so as to maintain the wire at the designated temperature. The change in voltage being supplied to the wire is proportional to the velocity of the fluid flowing over it - the higher the velocity, the higher the heat transfer between the wire and the fluid, and hence the higher the voltage that the circuit needs to supply to the wire to keep it at constant temperature. One is therefore able to directly relate the velocity of the fluid to the voltage being supplied to the wire. Hot-wire anemometry offers the ability to sample the velocity signal at a very high sampling rate (order of kHz), and provides accurate measurements of flow velocity, if proper calibration procedures are followed. The resulting time series from hot-wire anemometry can be analysed to reveal the statistical properties of the flow. More details on hot-wire anemometry and post processing are presented in Chapter 3.

For a turbulence analysis, it is desirable to obtain the velocity fluctuations from the velocity time series, the output of hot-wire anemometry. To obtain a time series of the turbulent fluctuations a simple decomposition is used on a time series velocity, $u(t)$ which is the output of hot-wire anemometry. The decomposition separates the average component, $\overline{u}$, from the fluctuating component $u'(t)$. Equation Equation (2.2) shows the streamwise x, and planar, y and z components of this decomposition. It is possible to measure one or multiple velocity components of a given flow using hot-wire anemometry.

$$\begin{aligned} u(t) &= \overline{u} + u'(t) \\ v(t) &= \overline{v} + v'(t) \\ w(t) &= \overline{w} + w'(t) \end{aligned} \tag{2.2}$$

Because of the random nature of a turbulent signal, one must employ various statistical approaches to characterise and analyze it. One can, however, make certain assumptions

about the nature of the turbulent signal in order to simplify the analysis; for example, assuming the flow is statically stationary, homogeneous and isotropic flows yield simplified expressions that can be used to describe the motion of the turbulent flow. These definitions will be explained briefly. For a time series of velocity data, the flow would be statistically stationary if the statistics of the time series do not change when the time series data is shifted by some amount, i.e. its autocorrelation, as defined by Equation (2.12), is zero. A process is statistically homogeneous if its statistical properties do not depend on the position of the flow being measured i.e. $\frac{\partial}{\partial x} = 0$. Lastly a flow would be isotropic if the velocities being measured are independent of coordinate reflections and rotations.

The use of probability density functions (PDFs) are another way one can characterize turbulent flows. A PDF is a histogram that indicates the relative probability of a measurement taking on a value within a certain interval. For example, there is a high probability that a single velocity sampled in a flow with an average speed of $5\,\mathrm{m\,s^{-1}}$ flow will be close to $5\,\mathrm{m\,s^{-1}}$. Note that

$$\int_{-\infty}^{\infty} P(u)\mathrm{d}u = 1\ , \tag{2.3}$$

where u is the velocity, which itself is a random variable.

If a PDF is Gaussian, only two parameters, the mean and variance, are therefore needed to describe the random variable being investigated. Higher moments of the PDF, specifically the skewness

$$S = \frac{\overline{(u-\overline{u})^3}}{\overline{(u-\overline{u})^2}^{3/2}}\ , \tag{2.4}$$

and the kurtosis

$$K = \frac{\overline{(u-\overline{u})^4}}{\overline{(u-\overline{u})^2}^2}\ , \tag{2.5}$$

provide insights into the behaviour of turbulent fluctuations. Skewness is a measure of how symmetric the fluctuations are with respect to the mean, whilst the kurtosis measures the influence of the extreme values of the PDF, the "tails" of the distribution. For a Gaussian, or normal distribution, the skewness is zero and the kurtosis has a value of 3.

Given that velocity fluctuations are present in a turbulent flow, one can define an en-

ergy of the fluid based on these fluctuations; the turbulent kinetic energy (per unit mass), is shown in Equation (2.6). The equation can be simplified by assuming the flow is irrotational, where the two planar velocity fluctuations are approximately equal $v' = w'$.

$$k = \frac{1}{2}\left[\overline{(u')^2} + \overline{(v')^2} + \overline{(w')^2}\right] \approx \frac{1}{2}\left[\overline{(u')^2} + 2\overline{(v')^2}\right] \tag{2.6}$$

As well as having a kinetic energy, turbulent flows contain a wide array of eddies of different length scales and a wide range of time scales. The largest scales, the integral scales, are dictated by the geometry of flow and the smallest scales depend on how the energy in the flow is dissipated. These length and times scales all coexist on a continuum. Generally, energy will enter the flow at the largest scales, after which the energy is transferred to eddies of smaller sizes, until it is finally dissipated at the smallest scales, where viscosity is a dominant force, and the friction due to viscosity dissipates energy to heat. This energy transfer process is called the energy cascade. It is important to remember that turbulent flows can only occur in 3D space. A 2D turbulent flow would not transfer energy down an energy cascade since vortex stretching (a 3D phenomenon) is critical to this transfer of energy, (Pope, 2000). Although many approximations assume isotropy or reduce the amount of variables involved, it is important to remember turbulence is always a 3D phenomenon and these assumptions only aid in its analysis.

The smallest turbulent scales, or Kolmogorov scales, are statically independent of the large scales. At this small scale it is reasonable to assume the size of the small eddies only depend on the viscosity of the fluid and the dissipation rate of the TKE, commonly referred to as the dissipation, ε. The dissipation is estimated from the large scales of the flow, using a simple energy balance; the energy provided by the large scales of the flow equals the energy dissipated by viscosity in the small scales of the flow. Using the dissipation and the viscosity of a flow, it is possible to determine the smallest lengths η, velocities υ and time

scales present τ in a flow, collectively known as the Kolmogorov scales.

$$\eta \equiv \left(\frac{\nu^3}{\varepsilon}\right)^{\frac{1}{4}} \tag{2.7}$$

$$\tau \equiv \left(\frac{\nu}{\varepsilon}\right)^{\frac{1}{2}} \tag{2.8}$$

$$\upsilon \equiv (\nu\varepsilon)^{\frac{1}{4}} \tag{2.9}$$

Kolmogorov stated in his first similarity hypothesis that at sufficiently high Reynolds number, the small scales of the flow are statically isotropic and have a universal form that only depends on ν and ε, as shown in Equation (2.7)-Equation (2.9) (Kolmogorov, 1941a,b).

The variation of energy across the different length-scales in a turbulent flow are represented by the energy spectrum, comprised of three main sections. The first and largest section would be called the *energy-containing range* which provides the flow with energy, followed by the *inertial sub-range* which transfers energy down to the smaller scales, finally the *dissipation range*, where the energy is dissipated to viscosity. See Figure 2.1 for a visual representation of the energy cascade. The energy spectrum from a velocity signal can be obtained via the use of a fast Fourier Transform, where the frequencies are converted into wavenumbers as shown in Equation (2.10).

$$\mathscr{F}\{f(t)\} \equiv \frac{1}{2\pi}\int_{-\infty}^{\infty} f(t)e^{-i\omega t}\mathrm{d}t \tag{2.10}$$

These wavenumbers correspond to the reciprocal of the length scale of the energy containing eddies.

Kolmogorov's second similarity hypothesis states that for Reynolds numbers in the limit of infinity, the inertial subrange and dissipation range will have a profile that depends only on a single variable, the dissipation ε, and not on the viscosity ν; this holds true for all turbulent flows. From the first similarity hypothesis, both the viscosity and dissipation are required to describe the small scales of the flow. It is in these small scales where the energy of the flow is dissipated. The profile of the inertial subrange only depends on the one variable ε and not the other ν. From the second similarity hypothesis, it was shown that the inertial subrange will follow a $-\frac{5}{3}$ power law as shown in Equation (2.11) for values of

κ in the inertial subrange, where C is a universal constant. This power law is a consequence of the second similarity hypothesis and is a universal characteristic of turbulence.

$$E(\kappa) = C\varepsilon^{\frac{2}{3}}\kappa^{-\frac{5}{3}} \tag{2.11}$$

The energy cascade can therefore be viewed as follows: energy enters at the large scales which depend on the geometry of the produced flow field. The energy is then transferred down the energy cascade at a rate proportional to a $-\frac{5}{3}$ power law. Eventually the energy is dissipated due to viscosity in the dissipation range of the flow; the entire process is graphically represented in Figure 2.1. It is important to stress that the $-\frac{5}{3}$ power law describes the rate at which the energy is transferred through the energy cascade, not the rate at which energy is lost.

Generally, as the Reynolds number of a flow increases, so does the width (in terms of the frequency range it occupies in the spectrum) of the inertial subrange, which therefore implies that there is a wider range of scales within the flow. This, therefore, also implies that there is a wider $-\frac{5}{3}$ power law fit on the velocity spectra, as seen in Figure 2.1.

Although the spectrum conveys the amount of energy that resides within a range of length-scales within the flow, one typically focuses on three particular length-scales that give the user a heuristic view of the spectrum. These three scales are, in descending order, the integral length scale L_{ij}, the Taylor-microscale λ, and the Kolmogorov microscale η, where $L_{ij} \gg \lambda \gg \eta$. The Taylor-microscale exists within the inertial subrange there exists a Taylor-microscale and has no physical interpretation, but is useful nonetheless since it is a characteristic length scale of turbulence. In order to gain an understanding of this Taylor-microscale, one must first understand the autocorrelation function. An autocorrelation applied to a data set is a measure of how preceding data points are related to later data points, and over what time interval that relation exists; it can be seen as a test of whether the data is statistically stationary. For a 1D fluctuating time series, the autocorrelation is defined as

$$\rho(s) = \frac{\langle u'(t)u'(t+s)\rangle}{\langle u'(t)^2\rangle}\,, \tag{2.12}$$

which is a correlation between a time series, and the same time series shifted by s. Integrating this function from $t = 0$ to $t = \infty$ will yield the integral time scale, $\overline{\tau}$. This time

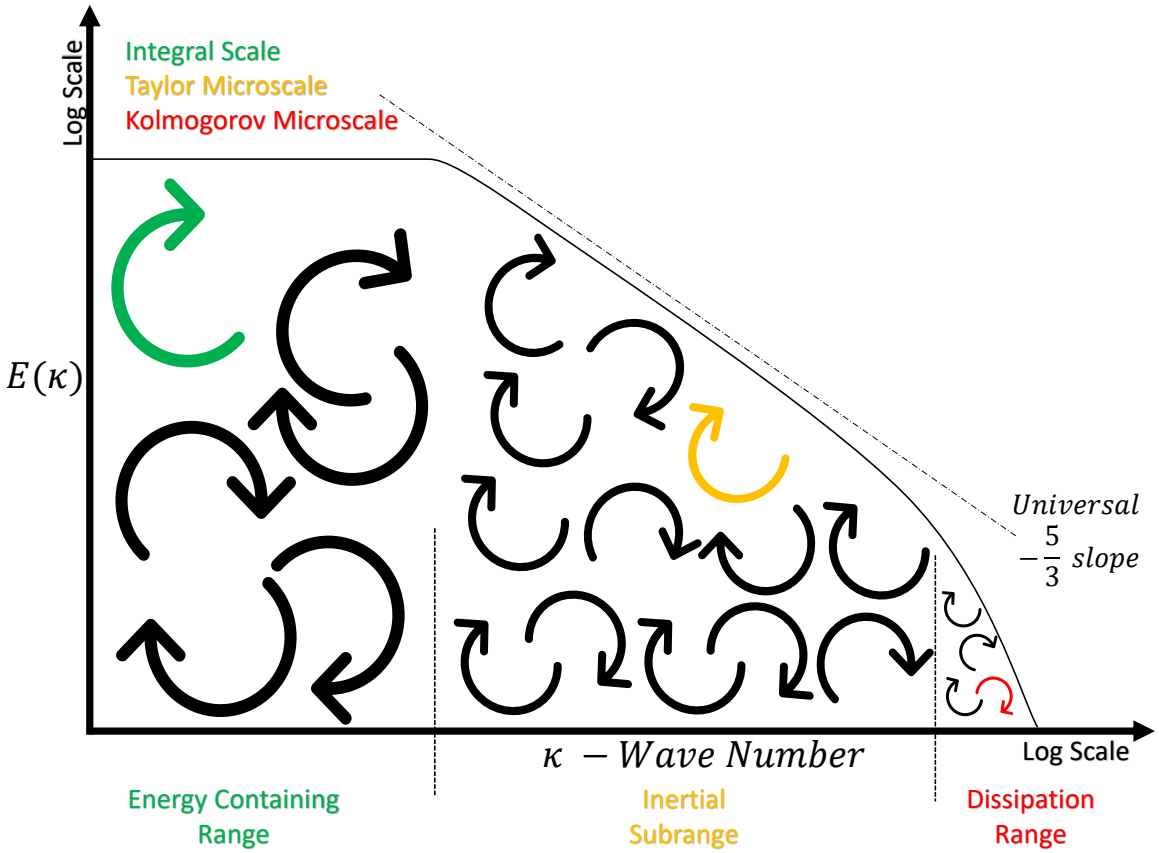

Figure 2.1: Theoretical model spectra.

scale can be converted to a length scale using Taylor's frozen-field hypothesis; if $u' \ll U$, then an approximation of the streamwise integral length scale, of the streamwise velocity component, is

$$L_{11,1} = \overline{\tau}\overline{U} \, . \tag{2.13}$$

Note that the subscripts are denoted as follows, using the example of $L_{11,1}$ as reference: the first two subscripts indicate which two vectors are correlated, in this case it is the streamwise velocity component correlated with itself. The last subscript indicates the direction of the vector separating the correlated velocities, which in this instances denotes the streamwise direction. In a similar manner, $L_{22,1}$ denotes the streamwise integral length scale of the transverse velocity components.

Another method of determining the integral length scale is to apply the autocorrela-

tion to space, not time. For homogeneous, isotropic turbulence, the two point correlation

$$R_{ij}(\mathbf{r},t) \equiv \langle u_i(\mathbf{x}+\mathbf{r},t)u_j(\mathbf{x},t)\rangle \tag{2.14}$$

can be simplified to

$$R_{ij}(\mathbf{r},t) = u'^2\left(g(r,t)\delta_{ij} + [f(r,t)-g(r,t)]\frac{r_i r_j}{r^2}\right) . \tag{2.15}$$

Similarly to the temporal autocorrelation function, $\mathbf{r}$ is a small shift in space for a spatially varying function, where $g(r,t)$ in Equation (2.15) is the transverse autocorrelation function and $f(r,t)$ is the longitudinal autocorrelation. One can therefore define the longitudinal integral length scale as

$$L_{11}(t) \equiv \int_0^\infty f(r,t)\mathrm{d}r . \tag{2.16}$$

It should be noted that from a practical point of view, to determine the integral length scale, the temporal autocorrelation and Taylor's hypothesis is typically utilised, as it requires a single sensor to measure the velocity data in time, as opposed to requiring two sensors spaced a distance r apart to obtain the function $f(r,t)$, the latter being more challenging to obtain experimentally.

The transverse Taylor-microscale can be obtained from $f(r,t)$ as

$$\lambda_f = [-\frac{1}{2}f''(0,t)]^{-\frac{1}{2}} , \tag{2.17}$$

and similarly, for the transverse Taylor-microscale,

$$\lambda_g = [-\frac{1}{2}g''(0,t)]^{-\frac{1}{2}} . \tag{2.18}$$

It is possible to relate the Taylor-microscale to the measured velocity. Pope (2000), shows how $f''(0,t)$ can be converted to a velocity derivative,

$$-\overline{u'^2}f''(0,t) = -\overline{u'^2}\lim_{r\to 0}\frac{\partial^2}{\partial r^2}f''(r,t) = \overline{\left(\frac{\partial u}{\partial x}\right)^2} . \tag{2.19}$$

Rearranging Equation (2.17) it is possible to write $\frac{-2}{\lambda^2} = f''(0,t)$ then multiplying

both sides by $\overline{u'^2}$ gives $\frac{2\overline{u'^2}}{\lambda^2} = -\overline{u'^2}2f''(0,t)$. The Taylor-microscale can be related to the velocity derivative of u as

$$\frac{2\overline{u'^2}}{\lambda_f^2} = \overline{\left(\frac{\partial u}{\partial x}\right)^2}\,, \tag{2.20}$$

Therefore, one is able to directly determine the Taylor-microscale from the streamwise velocity gradient, which can be obtained with a single sensor and the use of Taylor's frozen field hypothesis. For isotropic turbulence, it is useful to note that

$$\lambda_g = \frac{\lambda_f}{\sqrt{2}}\,. \tag{2.21}$$

Given these length scales, it is therefore possible to define a Reynolds numbers related to them. Using the definition, $L \equiv k^{3/2}/\varepsilon$, whose origin will be discussed later in this chapter, the turbulent Reynolds number can be written as,

$$Re_L \equiv \frac{k^{1/2}L}{\nu} = \frac{k^2}{\varepsilon\nu}\,, \tag{2.22}$$

which can be seen as a measure of the influence of large eddies (integral scales) on the flow. The Taylor-scale Reynolds number

$$Re_\lambda \equiv \frac{\overline{u'^2}^{1/2}\lambda_g}{\nu}\,, \tag{2.23}$$

can be seen as a measure of the influence of the inertial subrange on the flow. Generally, a flow with a large Re_λ will show characteristics that match Kolmogorov's predicted universal turbulence characteristics.

As mentioned previously, the dissipation, ε plays a major role in determining some of these scales. The dissipation is the rate at which the turbulent kinetic energy (TKE), Equation (2.6), is transferred through the energy cascade. For different flows, TKE can be lost or transferred in various ways. Using the Reynolds decomposition of the Navier-Stokes

equation, the turbulent kinetic energy budget is

$$\underbrace{\frac{\partial k}{\partial t}}_{\substack{\text{Local}\\ \text{Derivative}}} + \underbrace{\overline{u_k}\frac{\partial k}{\partial x_k}}_{\text{Advection, } A} = \underbrace{-\frac{1}{\rho_o}\frac{\partial \overline{u_k' p'}}{\partial x_k}}_{\substack{\text{Pressure}\\ \text{Transport}}} \underbrace{-\frac{1}{2}\frac{\partial \overline{u_i' u_i' u_k'}}{\partial x_k}}_{\substack{\text{Advective}\\ \text{Turbulent}\\ \text{transport, } T}} + \underbrace{2\nu\overline{\frac{\partial u_i s_{ik}}{\partial x_k}}}_{\substack{\text{Diffusion by}\\ \text{viscosity}}} \underbrace{-\overline{u_i' u_k'}\overline{\int_{ik}}}_{\text{Production, } P} - \underbrace{2\nu\overline{s_{ik}s_{ik}}}_{\text{Dissipation, } \varepsilon} \tag{2.24}$$

where

$$\int_{ik} = \frac{1}{2}\left(\frac{\partial \overline{u_i}}{\partial x_k} + \frac{\partial \overline{u_k}}{\partial x_i}\right) \tag{2.25}$$

is the mean rate of strain,

$$s_{ik} = \frac{1}{2}\left(\frac{\partial u_i'}{\partial x_k} + \frac{\partial u_k'}{\partial x_i}\right) \tag{2.26}$$

is the fluctuating rate of strain, and

$$k = (\frac{1}{2}\overline{u_i' u_i'}) \tag{2.27}$$

is the turbulent kinetic energy. For the case of homogeneous, isotropic, stationary flow the dissipation term simplifies to,

$$\varepsilon = 2\nu\overline{s_{ik}s_{ik}} = 15\nu\overline{\left(\frac{\partial u}{\partial x}\right)^2}\,. \tag{2.28}$$

The only remaining term for such a flow is the advection term

$$A = \overline{u_k}\frac{\partial k}{\partial x_k}\,, \tag{2.29}$$

and hence, since the mean flow is uniform in all directions, the turbulent kinetic energy budget can be simplified to

$$A = -\varepsilon\,. \tag{2.30}$$

Relationship Between Reynolds Numbers

One can relate the Reynolds number based on the integral scale to the Taylor-scale Reynolds numbers. Combining Equation (2.28) and Equation (2.20) one obtains

$$\varepsilon = 15\nu\frac{\overline{u'^2}}{\lambda_g^2}\ , \tag{2.31}$$

Squaring both sides of Equation (2.23) and inserting the above expression, one gets

$$Re_\lambda^2 = \frac{\overline{u'^2}15\nu\overline{u'^2}}{\nu^2\varepsilon}\ .$$

For isotropic flow, the turbulent kinetic energy is $k = \frac{3}{2}\overline{u'^2}$. Squaring and rearranging gives $\overline{u'^2}^2 = \frac{4}{9}k^2$, which we insert into the above expression to get

$$Re_\lambda^2 = \frac{4k^2 15\nu}{9\nu^2\varepsilon} = \frac{20k^2}{3\nu\varepsilon}\ .$$

Finally, using Equation (2.22),

$$Re_\lambda = \sqrt{(20/3)Re_L} \tag{2.32}$$

which is a relationship between the integral scale and the Taylor-scale Reynolds numbers for isotropic turbulent flow. This is one way to show how the intermediate scales of the flow are related to the large scales of the flow.

A simple scaling argument, along the lines of G.I. Taylor and G. Batchelor, (Batchelor, 1953), can be made to relate the turbulent dissipation rate to the turbulent kinetic energy and the integral scale. Consider an energy cascade where, owing to conservation of energy, the rate at which energy enters the cascade at the large scales L is dissipated at small scales η via viscous dissipation ε; as before, we assume that $L \gg \eta$. This therefore implies that the rate at which energy is transferred across the scales (from the large to the small), must also equal the rate at which the energy is dissipated ε - in other words, there is an *equilibrium* in the cascade. From the spectrum, we also know that the turbulent kinetic energy at the large scales k_L is significantly larger than that at the small scales i.e., $k_L \gg k_\eta$,

and so the energy being transferred across the scales is simply $k_L - k_\eta \approx k_L$. From a scaling point of view, we argue that the energy transferred scales as $k_L \equiv k$, the total energy in the flow. The time taken to transfer the energy from the large scales to the small is therefore $\mathrm{d}t \sim L/k^{1/2}$. Hence the rate at which energy is transferred from the large scales to the small scales is $\mathrm{d}k/\mathrm{d}t \sim k/(L/k^{1/2}) = k^{3/2}/L$, and this in turn is proportional to the rate at which energy is dissipated ε. Therefore, from a scaling point of view, one finds that

$$\varepsilon \sim \frac{\mathrm{d}k}{\mathrm{d}t} \equiv \frac{k^{3/2}}{L} \implies \varepsilon = C_\varepsilon \frac{k^{3/2}}{L}\,, \tag{2.33}$$

where C_ε is a constant for high Reynolds number turbulent flows, referred to as the dissipation coefficient.

A recent body of work, however, has shown that the dissipation coefficient is not universally constant and depends on the internal structure of the turbulence being generated, (Goto and Vassilicos, 2009; Nedić and Tavoularis, 2016a; Vassilicos, 2015). Specifically, it is found to be non-constant in regions where the cascade is not in equilibrium, namely $\mathrm{d}k/\mathrm{d}t \neq \varepsilon$. The behavior of the dissipation coefficient, measured in the streamwise direction, can therefore be used as an indicator of when the flow is in equilibrium. Once C_ε reaches a stable value, the turbulent flow is considered fully developed. In the development region, located close to the source of the turbulence generation the dissipation coefficient has been found to be inversely proportional to the turbulence Reynolds number, (Vassilicos, 2015).

2.2 Methods of Generating Turbulence

The goal of many turbulence studies has been to generate turbulent flows with a large Taylor scale Reynolds number, in order to test whether Kolmogorov's hypothesis are valid in the limit when $Re_\lambda \to \infty$. Kolmogorov predicted that for high Reynolds number flows, we can expect to see universal properties of the smaller scales in turbulent flows, specifically the $-\frac{5}{3}$ power law in the inertial subrange. As a result, many scientists have tried to create flows with high Re_λ in a laboratory setting.

One popular method of producing this fundamental type of turbulence is by obstruct-

ing the flow with a rectangular grid. Grid turbulence has been widely studied since the mid 1930's, (Batchelor and Townsend, 1948; Simmons and Salter, 1934; Taylor, 1935), however, one of its main shortcomings is that it produces flow with a low Reynolds numbers (both turbulent and Taylor-microscale). Many of the theories physicists and engineers attempt to verify, however, assume very large Reynolds number. From the end of the 20^{th} century to the present, there has been a large leap in creating desirable high Reynolds number flows. In the 1990's, active grids were made popular in the turbulence community; these grids consist of spinning triangular pieces that block the flow. This type of grid is capable of producing stochastic turbulence with large Reynolds numbers not previously seen in mid-sized wind tunnels, (Makita, 1991; Mydlarski and Warhaft, 1996). These active grids were the foundation, or proof of concept, for the University of Miyazaki's multi-fan wind tunnel which uses active control turbulence generation, (Ozono and Ikeda, 2018). The University of Miyazaki in Japan has produced the vast body of research into MFWTs, (Nishi et al., 1997, 1999; Nishi and Miyagi, 1995; Nishi et al., 1993; Ozono and Ikeda, 2018; Ozono et al., 2006; Takamure and Ozono, 2019), which shall be explained later in this chapter .

2.2.1 Passive Grids

One method of generating homogeneous, isotropic turbulence in a laboratory is achieved by obstructing the flow with a grid consisting of evenly spaced horizontal and vertical rectangular bars or rods, where the distance between the centre of the bars is defined as the mesh size L_0. Although this type of turbulence is not as common in nature, we can begin to understand turbulent flows of increasing complexity by first investigating their simplest form. As such, grid turbulence has been studied extensively, (Batchelor, 1953; Comte-Bellot and Corrsin, 1966; Simmons and Salter, 1934; Taylor, 1935), because of the isotropic turbulence these grids produced when obstructing a flow. Traditionally the development region of grid turbulence, namely the region within roughly 20 mesh sizes, L_0, from the grid i.e., $x < 20/L_0$, was not studied, (Batchelor and Townsend, 1948). In this region, the production and dissipation terms in Equation (2.24) are non zero due to the presence of a mean sinusoidal velocity gradient behind the grid. By studying the near field, it has provided insight into how turbulence evolves, and how the development region influences

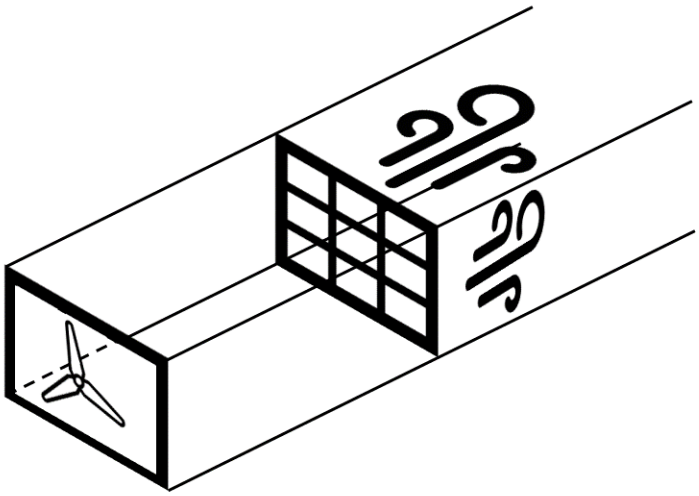

Figure 2.2: Illustration of a passive grid.

the fully developed region of the flow, (Bos, 2020).

As mentioned previously, close to the grid, for stationary, homogeneous, isotropic flow, the advection term is balanced by the production and dissipation terms, the TKE budget becomes,

$$\overline{u_k}\frac{\partial k}{\partial x_k} = P - \varepsilon \, . \tag{2.34}$$

Further from the fan wall, where there is expected to be a lack of velocity shear in the flow, the production is zero, resulting in a balance between the dissipation and advection terms of the TKE budget,

$$\overline{u_k}\frac{\partial k}{\partial x_k} = -\varepsilon \, . \tag{2.35}$$

For decaying grid turbulence, the TKE has been shown to decay as a power law, (Batchelor, 1953; Comte-Bellot and Corrsin, 1966; Taylor, 1935), namely

$$\frac{k}{U_\infty^2} = A\left(\frac{x - x_0}{L_0}\right)^n \, , \tag{2.36}$$

where U_∞ is the mean free stream velocity, x_0 is the virtual origin, L_0 is the mesh size of the grid and A is a scaling constant. Within the development region of decaying grid turbulence, namely the region where the dissipation coefficient is non-constant, it has been found, for both regular and fractal grids, that $-2.4 \leq n \leq -3.0$, (Hearst and Lavoie, 2014; Valente and Vassilicos, 2011, 2015). For the developed region, namely where the dissipation coefficient is constant, $-1.1 \leq n \leq -1.4$, again for both regular and fractal-type grids, (Comte-Bellot and Corrsin, 1966; Lavoie et al., 2007).

2.2.2 Active Grids

Although regular, and fractal grids, have proven invaluable in developing much of the turbulence theory that we have today, a main shortcoming of them is their limited capability of generating large Reynolds numbers, generally $Re_\lambda < 100$ for these passive grids. Active grids were made popular by Makita (1991), and then greatly expanded upon by Mydlarski and Warhaft (1996). Makita generated a turbulent flow with $Re_\lambda = 387$, whilst Mydlarski and Warhaft were able to achieve a $Re_\lambda = 473$. Larger Taylor-scale Reynolds numbers studies, using both active and passive grids, include Kang et al. (2003) with $Re_\lambda = 716$, and Larssen and Devenport (2011), who achieved $Re_\lambda = 1362$.

The wind tunnels used in these studies replaced a traditional grid comprised of rectangular bars or rods with an array of triangular agitator wings on bars attached to motors; the bars and agitator wings spin, which is the active part of the grid. The bars randomly change direction and rotation speed which creates the highest TKE and integral length scale, and as a result, a larger Re_λ (Mydlarski, 2017).

2.2.3 Random Jet Arrays

A stirred tank or grid stirred tank (GST) is an experimental device used to create zero mean turbulent flows, wherein the fluid, typically water, is agitated in a tank and the resulting motions are measured using particle image velocity. The resulting motion is turbulent with temporal velocity measurements fluctuating about zero. One method of agitating the flow is via *random jet arrays*, which utilize parallel planar arrays of jets that randomly fire jets of fluid towards each other. The resulting motion creates a region of 3D

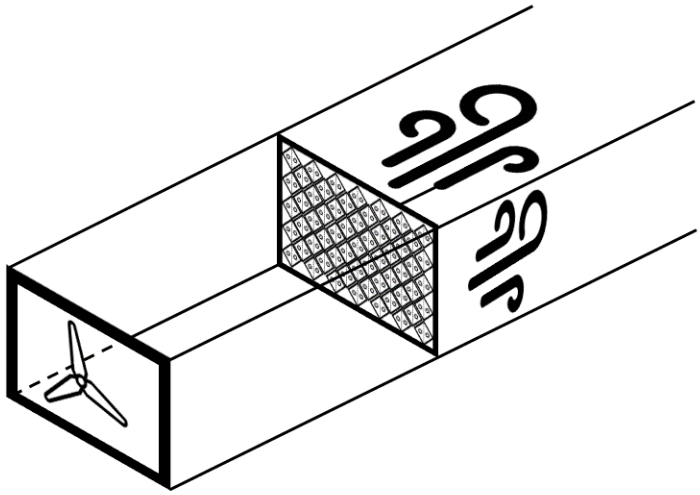

Figure 2.3: Illustration of an active grid with agitator clips.

homogeneous isotropic turbulent flow with large length scales Bellani and Variano (2014). Not only are length scales produced by random jet arrays larger than those typically made by passive and active grids, the homogeneity levels are notably improved as well. The Re_λ produced using a random jet array was reported as 314 by Variano and Cowen (2008) $Re_\lambda = 334$ by Bellani and Variano (2014) and a range of $Re_\lambda = 300 - 500$ was reported by Carter and Coletti (2017). These turbulent Reynolds number are typically the same order of magnitude as seen in active grids.

2.2.4 Multi-Fan Wind Tunnels

Multi-fan wind tunnel (MFWT) facilities are slowly growing in popularity. For example, the Canadian based WindEEE Research Institute at Western University, (Hangan et al., 2015), used an array of fans to mimic wind gusts for wind engineering application. A facility at Tianjin University in China uses multiple fans on multiple rotating walls to create tailored flows, (Wang et al., 2015). This facility uses six rectangular walls each with

a 2-by-4 grid of 140 mm fans. Each of the six walls can also rotate $\pm 90^{\circ}$. The results of this study show that this facility is capable of generating flows comparable to outdoor near-surface airflow. The vast majority of research, however, using a grid of fans has been conducted at the University of Miyazaki in Japan.

The goal of the work conducted by the Miyazaki research group has been to mimic the atmospheric boundary layer, which is achieved through control of turbulent scales and turbulence intensity. The tunnel used for this research is a simple design with small fans that have a fast input response. The operating range of the Miyazaki tunnel is $5\,\mathrm{m\,s^{-1}}$, (Nishi et al., 1997, 1999; Nishi and Miyagi, 1995; Nishi et al., 1993; Ozono and Ikeda, 2018; Ozono et al., 2006; Takamure and Ozono, 2019). The references listed above are for publications released by this research group in English, although additional works have been published in Japanese, (Ikeda and Ozono, 2013; Takamure and Ozono, 2016; Wakamatsu et al., 2019).

The focus of the research conducted at the University of Miyazaki is the testing of structures in atmospheric conditions for civil engineering applications. More precisely, their focus is on generating high intensity large scale turbulence to mimic the atmospheric boundary layer. Ozono and Ikeda (2018), showed that it is possible to generate large turbulence intensities and large scales of turbulence by modulating each fan in the MFWT individually, giving each fan the same signal shifted in time also appeared to eliminate the pulsatile components of the flow, a problem that was present with previous operating modes.

Power Spectrum Modification Method

Nishi et al. (1993) considered the flow downstream of a single column of 11 voltage controlled fans In order to determine the frequency response of the flow, a square wave signal was sent to the fans and the corresponding response of the velocity field was measured. A frequency response of 2 Hz was observed. The group also attempted to control the turbulence intensity of the resulting flow by modulating the fans in one of four ways:

1. All fans ON
2. The even number fans ON and odd fans OFF

3. All fans given the same 1 Hz periodic signal

4. Even numbered fans given a 1 Hz periodic signal with the odd numbers fans OFF

All fans ON produced a streamwise turbulence intensity of $\approx 2\%$, with the other cases producing $6\% - 8\%$, with Case 4 producing the largest intensity level. The streamwise integral length scale of Case 3 appears to be significantly larger than the three other cases, with $L_{11,1} = 0.75\,\text{m}$ compared to $0.1\,\text{m} - 0.2\,\text{m}$ for the other cases, however, Nishi et al. (1993) did not provide information on how the turbulent fluctuations are decomposed from the mean flow, if the flow is stochastic or how the integral length scale is calculated from their data.

Nishi and Miyagi (1995), again using a single column of 11 fans, attempted to control the resulting spectra measured in the flow. Building on the previous work, feedback was used to generate mean uniform flow, and boundary layer flows. The main objective of their study was to match a desired spectra, given by the von Kármán equation for isotropic turbulence

$$S_u(n) = \frac{4I_u^2 U L_u}{[1 + 70.8(nL_u/U)^2]^{5/6}}\,, \tag{2.37}$$

where I_u is the turbulence intensity, $S_u(n)$ is the power spectral density, L_u the turbulent length scale and n is the frequency of the turbulence. The working hypothesis was to convert the target spectrum to a time series using a Fourier transform, and give this time series as a signal to the fans. During testing, the resulting spectrum would be measured and compared against the target spectrum, and modifications would be made until the target and measured spectrum matched within a certain tolerance. The results were deemed satisfactory, but the resulting spectra only match the target spectrum at low frequencies,and was limited by the frequency response of the fans, which was 2 Hz.

Time-Lag Modification Method

Nishi et al. (1997, 1999) attempted to improve upon the spectra tracking. The *time-lag modification method* (Nishi et al., 1997) was developed to account for the known lag in the fans. The input signal was modified assuming first order lag of the velocity response of

the fan, which improved the spectra tracking at larger frequencies; for example, the spectra produced without the correction method would divert substantially from the target spectra for $f > 10^0$ Hz. The *time-lag modification method* improved the tracking significantly, the correlation between the target input signal and measured output was 96% compared to 88% without any modification. As a result of this, they were able to successfully create a flow with a specific integral scale and turbulence intensity using the method of tracking a time space converted spectrum.

Cao et al. (2002) extended the work to more than a single column of fans. The wind velocity history was reproduced in a wind tunnel comprised of 9 columns of 11 fans each. The velocity history of a target flow was reproduced in the 3D wind tunnel using the *time-lag modification method*, which was previously tested on 2D tunnels (Nishi et al., 1997). Large changes in velocity over very short time periods were also reproduced, an impulse-like change of $2.5\,\mathrm{m\,s^{-1}}$ was tracked with 89.8% correlation coefficient between the target and generated flows. This study also showed that by accurately reproducing the modelled velocity time history resulted in an accurate reproduction of the expected turbulent statistics from the model; the turbulence statistics in the case being the mean flow, turbulence intensity and integral scale. Intermittent turbulence seen in the atmospheric boundary layer was also tracked from a time history with 89.8% correlation between velocity history and reproduced velocity. The main objective of the majority of the work up to this point has been to mimic the atmospheric boundary layer. The papers discussed above prove that this is possible through the means of tracking a previously obtained velocity signal of the atmospheric boundary layer.

Quasi-Grid Mode

Later studies, however, were concerned with studying methods of generating large turbulence intensities and integral scales without velocity tracking. Ozono et al. (2006) attempted to compare a velocity history tracking method, and the turbulence generated by it, to another fan wall configuration called the *quasi-grid mode*. In the *uniformly-active mode*, the fan is being fed a time series of velocity with the goal of tracking a von Kármán spectrum - Equation (2.37) - similar to the spectra tracking seen previously (Cao et al., 2002; Nishi et al., 1997; Nishi and Miyagi, 1995; Nishi et al., 1993). In the *quasi-grid*

mode, each fan that is set to ON is completely surrounded by fans that are OFF, with the active fans given a constant signal. These experiments attempt to obtain a $-5/3$ slope on the measured power spectra. For the *uniformly-active mode*, the spectra are not smooth, and the inertial subrange of the spectra divert considerably from Kolmogorov's predicted $-5/3$ slope. The spectra generated from the *quasi-grid mode* has a better agreement to the $-5/3$ slope for approximately one decade, and appears to give a typical turbulent spectra, although no PDFs were provided. Moreover, at approximately 30 fan lengths downstream, the reported Taylor-scale Reynolds number was $Re_\lambda = 270$. The results form the *quasi-grid mode* also show better isotropy of 1.1, compared to approximately 3-8 for the *uniformly-active mode*, an isotropy of 3-4.5 for a turbulence intensity of 5% and isotropy of 5.5-8 for a turbulence intensity of 10%. It was noted that the uniformly active mode is dominated by pulsating components, whilst the *quasi-grid mode* appears to be a better analog for decaying turbulence that has been traditionally studied.

Random-Phase Mode

The *random-phase mode* was introduced by Ozono and Ikeda (2018). Here, each fan in the 9-by-11 grid is randomly assigned a unique integer value between 1 and 99. Next, one predetermined signal is constructed, using the following expression

$$u_e(t) = U_e + \sqrt{\frac{2C}{T_0}} \sum_{i=1}^{J} \sin(2\pi f_i t + \phi_i) \; . \tag{2.38}$$

This signal is comprised of J sinusoidal waves (in this case 40), each with a unique frequency f_i. The constant spectral density C and period T_0 are preset: C varies from $1\,\mathrm{m^2\,s^{-1}}$ to $20\,\mathrm{m^2\,s^{-1}}$ and the period is set to 40.94 s, hence the minimum frequency that can be used is $f_{min} = \frac{1}{T_0} = 0.024$ Hz, and the maximum frequency is set to $f_{max} = 0.96$ Hz, which is $40 f_{min}$ Note that the authors set f_{max} to be well below the physical limitation of the fans, which is 2 Hz. The values of f_i are 40 evenly spaced frequencies between f_{min} and f_{max}. Lastly each frequency f_i is assigned a corresponding phase ϕ_i which is randomly generated for each value of $i = 1$ to 40, with the condition $-\pi \leqslant \phi_i \leqslant \pi$. To reiterate, all of this is to create one velocity signal, comprised of 40 frequencies and phase shifts.

The second step of the *random-phase mode* utilizes the randomly assigned integers

discussed previously. Given that the signal generated using Equation (2.38) is periodic, with a period of T_0, each fan can produce a velocity signal according to Equation (2.38) with a unique temporal offset Δt_e, noting that $0 \leq \Delta t_e < T_0$. This temporal offset is determined using

$$\Delta t_e = T_0 \frac{n_e - 1}{N} , \tag{2.39}$$

where N is the total number of fans and n_e is a unique random integer number within $1 \leq n_e \leq N$. In the study by Ozono and Ikeda (2018), $N = 99$. Equation (2.38) can therefore be rewritten as

$$u_e(t + T_0(n_e - 1)/99) = U_e + \sqrt{\frac{2C}{T_0}} \sum_{i=1}^{J} \sin(2\pi f_i(t + T_0(n_e - 1)/99) + \phi_i) . \tag{2.40}$$

In the study by Ozono and Ikeda (2018), the final signal generated by the facility therefore contains 40 frequencies, and 99 random temporal shifts. A sample of the velocity signal generated using Equation (2.38), and the composite signal using Equation (2.40) for $J = 40$ and $N = 99$ is shown in Figure 2.4. The resulting flow field eliminated the pustule component of the flow, a problem that exists with the *uniformly-active mode*. The *random-phase mode* was successful at creating large turbulent scales $L_x = 0.65$ m, intensities $\frac{u'}{U} = 13.3\%$, and also produced $\mathrm{Re}_\lambda = 753$. In contrast the *quasi-grid mode* produced $L_x = 0.15$m, $\frac{u'}{U} = 5.54\%$, and $\mathrm{Re}_\lambda = 281$. The authors argued that the increased scales of the turbulence generated by the *random-phase mode* is due to the temporal offset introduced to each of the fans, which in turn create shear layers and thus generate turbulence. This increased mean shear, which manifests as a velocity gradient, results in an increase in the production term since the $\frac{\partial \overline{u}}{\partial y}$ is non zero and non constant.

One of the drawbacks of this method, however, was that the anisotropy of the *random-phase mode* was 1.20 at $x/M = 60.5$, whereas the *quasi-grid mode* had and anisotropy of 1.12 at the same location, in this case M is the equivalent duct size at the outlet of each fan. The decay exponent of the turbulent kinetic energy, for both the *random-phase mode* and *quasi-grid mode*, were found to be $n = 1.08$ and $n = 1.05$ respectively. These decay exponents were obtained over the spacial regions $44.2 \leq x/M \leq 60.5$ for the *random-phase mode* and $37.2 \leq x/M \leq 60.5$ for the *quasi-grid mode*. Lastly, inspection of the spectra for both the *quasi-grid mode* and *random-phase mode* indicate a good $-5/3$ fit for just over

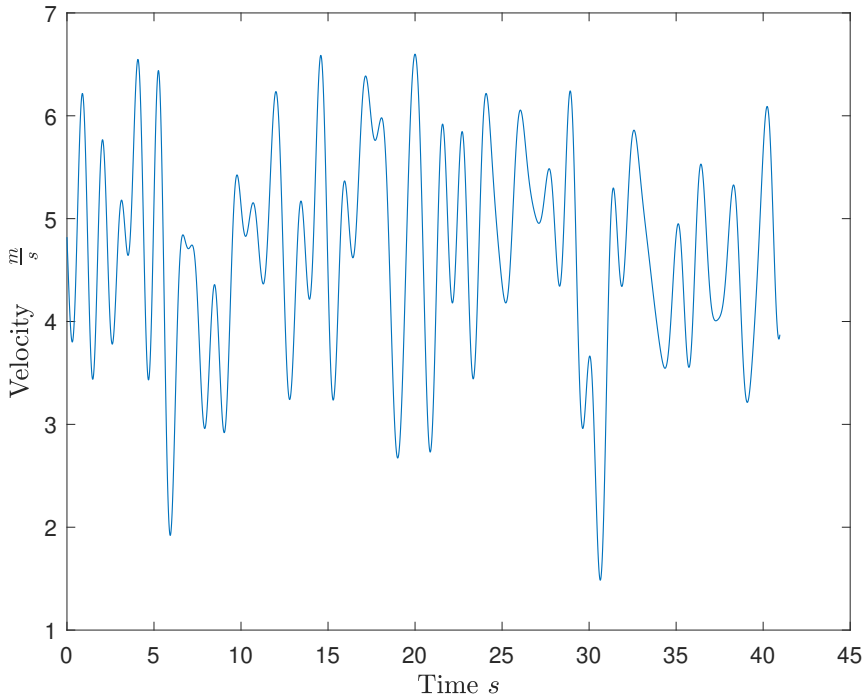

Figure 2.4: An example of the time Varying signals given to the MFWT at the University of Miyazaki. The *random-phase mode*, one instance of Equation (2.40).

one decade for the *quasi-grid mode* and just over two decades for the *random-phase mode*.

In a later study, Takamure and Ozono (2019) examined the *random-phase mode* using two frequencies (J=2), and investigated how changing N from 2, 5, to 99 affected the statistics of the flow. The results indicated that $N = 5$ overall temporal shifts are sufficient to create similar turbulence intensities and scales as compared to the $N = 99$ case. A drawback of constructing a periodic signal of only two frequencies, however, ($J = 2$) is that a pulsatile component was introduced to the flow. In order to examine the velocity fluctuations u', therefore, the authors utilised a triple decomposition

$$u(t) = \overline{u} + u' + \tilde{u}\,, \tag{2.41}$$

where $\tilde{u}$ was the pulsatile component of the signal.

2.3 Objectives Revisited

Of the many ways turbulent flow can be created, the reviewed literature and presented theory suggest that creating a velocity shear, thus resulting in a local velocity gradient, in the planar direction will produce high levels of turbulence. Although dynamic changes to the velocity field have shown to produce very large turbulence intensities and integral scales, this study will focus on the static case, with the aim of producing stochastic turbulence conditions in the MFWT. Much of the literature on MFWT has investigated the region far from the fan wall ($x \gtrapprox 30M$), but there are no studies investigating the near field, close to the fan wall. The aim of this study is to fill this gap in knowledge by focusing primarily on the near field region of the turbulence.

The summary of the revised objectives are as follows:

1. Evaluate the stream wise evolution of the bulk velocity, turbulence intensity, turbulent kinetic energy, integral scale and other turbulent parameters for different velocity gradients, or shear ratios S_r.

2. Fill the current gap in knowledge of what occurs in the near field region of flows produced in MFWTs by investigating how the turbulent kinetic energy decays, and by looking at the behavior of the dissipation coefficient.

3. Determine a scaling law for the turbulent parameters as a function of the velocity gradients. With the aim of predicting the magnitude of turbulent intensity for generating flows for UAV and drone testing.

Chapter 3

Experimental Equipment & Procedure

3.1 McGill Multi-Fan Wind Tunnel Facility

A new multi-fan wind tunnel facility was constructed for this thesis. It is composed of 81 computer fans (*Delta Electronics* QFR0812UHE) each with a diameter of 80 mm, arranged in a 9-by-9 grid. The grid of fans are secured by a structure made of 3 mm thick medium density fiberboard (MDF); this resulted in the square test section having a height and width of 750 mm-by-750 mm. The fan wall assembly is shown in Figure 3.1(a), and it is attached to a test section assembly which is 2.4 m in length, as shown in Figure 3.1(b). Test section modules can be added to the assembly to increase the overall length, currently two modules are used , each 1.2 m in length; note that the technical drawings and assembly instructions for the test section can be found in Appendix B. Great care was taken during the manufacturing of the test facility to ensure flatness and straightness. T-Slotted aluminum extrusions (*MiniTec* aluminium extrusions, purchased from *Central Industrial Solutions*, Cambridge, Ontario, Canada), so chosen for their ease of assembly and modularity, were used to hold the wooden test section.

Both the fan wall and test sections have adjustable ground clearance; this feature allows a multitude of apparatuses and stands to be positioned below the wind tunnel, an example of this is the *Quanser* 6-degrees of freedom motion platform shown below the wind tunnel in Figure 3.1(b). A 30 cm diameter hole was cut in the test section floor to

(a) Inlet of tunnel.

(b) Outlet of tunnel.

Figure 3.1: McGill's Multi-Fan Wind Tunnel.

allow for the installation and testing various wind tunnel models.

The facility is fitted with a 3D traversing mechanism along the top surface of the test section, as shown in Figure 3.2. The gantry cart located inside the test section allows the user to install various probes and sensors. The traverse is a modified version of linear rails produced by *OpenBuilds*, a company that specializes in modular, open source, CNC routers. Two 2 m long *OpenBuilds* C-Beams run the entire length of the outer face of the ceiling panels of the test section modules. Two C-Beam gantry carts are mounted with wheels on the C-Beams, and can travel along the streamwise (x) direction of the tunnel - see Figure 3.2 for co-ordinate system used. To allow for movement in the $y-z$ plane, two *OpenBuilds* V-Slot linear traverses are mounted to the C-Beam carriages, creating the

Figure 3.2: CAD of wind tunnel with traversing mechanism, side wall removed. Figure also shows coordinate system used. The origin (0,0,0) is located at the center of the face of the center fan, the yellow star in the figure

planar traverse, as shown in Figure 3.3. The C-Beam carriages running the length of the wind tunnel are manual, therefore the user has to move the carriage themselves to the desired streamwise location; a measuring scale has been fitted to the C-Beams to facilitate consistent and precise positioning in the streamwise direction. The planar traverse inside of the tunnel is powered electrically by stepper motors. Two "I" beams are attached to the carriages on the C-Beams, outside of the test section. The middle of the "I" beams pass passes between two sets of inter-locking bristles; the purpose of the bristles was to reduce pressure losses in the wind tunnel. Finally the bottom of the "I" beams are connected to the planar traverse.

The traversing system is controlled by a purpose built LabVIEW virtual instrument program. The code is set up to move the traverse and record measurements from probes mounted to the traverse, keeps track of the location of the probe, communicates with the A/D converter and DAQ, and allows the user to label and organize the raw data from the velocity measurements. The filename for the LabVIEW code is: "+++*FanWall Experiment*+++.*vi*", and a screenshot of the front and back panel are shown in Appendix A.

Each fan receives individual 12 V power signals via a power supply unit connected to the mains. The fans have the capability to be individually modulated using Pulse Width

Figure 3.3: Planar traversing Mechanism for the wind tunnel.

Modulation (PWM) signals, as well as the ability to measure the RPM of the fan using a counter. Currently the hardware used is only capable of sending four different PWM signals to the fans. A multitude of patterns can be achieved with different wiring patterns and signal splitters. For this work, however, we have decided to begin with sending two signals provided to the fans which are steady (do not change in time).

The fans, *Delta Electronics QFR0812UHE*, are variable amperage and require a constant 12 V DC signal to operate; at maximum rotational speed the current drawn by the fans is 1 A. The RPM is controlled by adjusting the duty cycle of a 25 kHz PWM input signal. Before the entire turbulent flow field generated by the fans could be investigated, it was necessary to determine the relationship between the PWM signal sent to the fan and the corresponding velocity it would produce. For these tests, the velocity was measured using a hot-wire anemometer, sampling at a rate of 75 kHz for 1 s. Measurements were taken at a distance of 550 mm from the fan wall with the entire fan wall set to the same PWM. The distance of 550 mm was chosen because fully developed mean flow was achieved along the entire length of the tunnel for the case where all fans were set to the same PWM. The lowest possible speed attained by the facility is $1.45\,\mathrm{m\,s^{-1}}$ and the highest speed is $7.85\,\mathrm{m\,s^{-1}}$, the dependency of PWM on the fan velocity is shown in Figure 3.4.

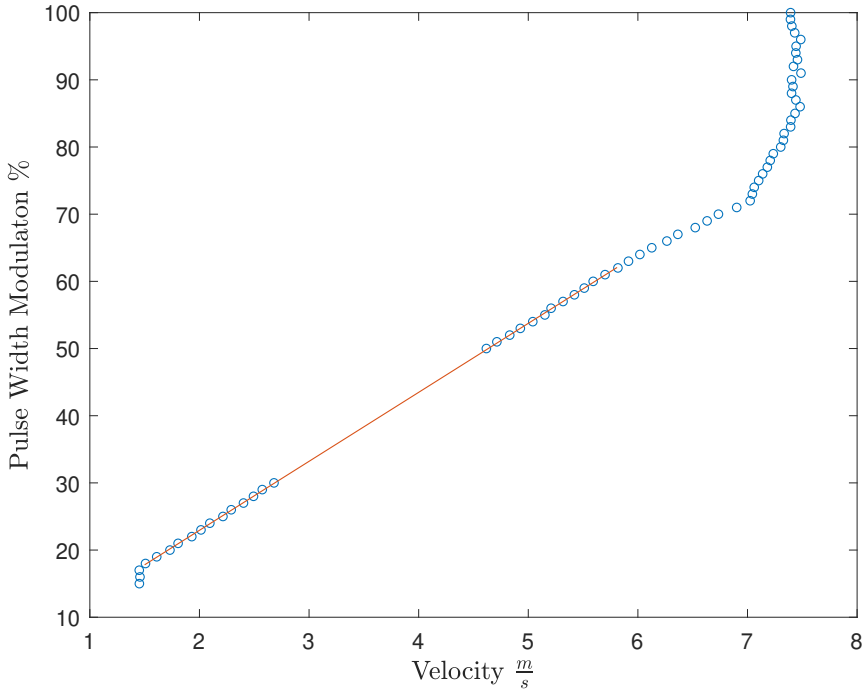

Figure 3.4: Relationship between the PWM signal sent to fan wall and resulting streamwise velocity at one point at $x = 550\,\text{mm}$.

Note that attempting to initiate the fans at any PWM lower than 30 % would not result in the fans to spin, but if the PWM was dialed down from a higher PWM, the fans would spin at PWMs as low as 15%. A linear fit between PWM and velocity can be fitted to a number of regions, the largest of which is shown in Figure 3.4. The various linear fits, and their ranges, are presented. All measurements were taken in the center of the plane (550, 0 0), aligned with the central fan of the fan wall. Within an error of 10%, the values of PWM can be calculated from the desired velocity using Equation (3.1).

$$\begin{aligned}
&\text{PWM} < 15\% && \overline{u} = 0 \\
&\text{PWM} = 15\% - 17\% && \overline{u} = 1.45\,\text{m}\,\text{s}^{-1} \\
&\text{PWM} = 10.27\overline{u} + 2.40 && 1.45\,\text{m}\,\text{s}^{-1} \leq \overline{u} \leq 5.8\,\text{m}\,\text{s}^{-1} \\
&\text{PWM} = 8.12\overline{u} + 15.12 && 5.8\,\text{m}\,\text{s}^{-1} \leq \overline{u} \leq 6.9\,\text{m}\,\text{s}^{-1} \\
&\text{PWM} = 30.90\overline{u} - 144.6 && 6.9\,\text{m}\,\text{s}^{-1} \leq \overline{u} \leq 7.23\,\text{m}\,\text{s}^{-1} \\
&\text{PWM} = 34.16\overline{u} - 168.2 && 7.23\,\text{m}\,\text{s}^{-1} \leq \overline{u} \leq 7.86\,\text{m}\,\text{s}^{-1}
\end{aligned} \tag{3.1}$$

3.1.1 Hot-Wire Anemometry

Hot-wire anemometry is a fast frequency response measurement technique used to measure a flow's velocity. The output of a carefully calibrated hot-wire experiment is a high resolution time series of velocity data. A feedback system is used to maintain a thin wire at a constant temperature. This thin wire, with a diameter d_w of the order of a few micro-meters, has a set length l_w and resistance R_w. When the wire is supplied with a current, I, the power consumption of the wire can be written as $P_w = R_w I^2$. As fluid passes over the wire, heat, q, will pass from the wire to the fluid by means of convective heat transfer. For a cylinder, the heat loss is given by $q = h_c A_s dT = h_c d l_w (T_w - T_{ref})$, where h_c is the heat transfer coefficient, $A_s = \pi d_w l_w$ is the cross sectional area of the wire exposed to the flow and $dT = T_w - T_{ref}$ is the difference between the temperature of the wire T_w and the temperature of the environment T_{ref}. The heat transfer coefficient is a function of the velocity of the fluid, $h_c = a + bU^n$. Heat transfer of the wire q is equal to the energy consumed by the wire, $P_w = R_w I^2$. Relating the two, one is able to obtain a relation for the heat transfer of the wire to fluid as

$$I^2 R_w = h_c d_w l_w (T_w - T_{ref}) = (a + bU^n) d_w l_w (T_w - T_{ref}) \; . \tag{3.2}$$

Ohms law relates the voltage E, to the current and resistance of an electrical system, $E = IR$. By squaring both sides, $E^2 = I^2 R^2$ and multiplying Equation (3.2) by R_w, one can relate the voltage lost due to heat transfer with the voltage supplied to the hot-wire.

$$E^2 = I^2 R_w^2 = (a + bU^n) R_w d_w l_w (T_w - T_{ref}) \tag{3.3}$$

As long as the reference temperature, T_{ref} and temperature of the wire, T_{wire} are kept constant, E^2 is only a function of U, since the resistance, length and diameter of the wire do not change. Defining new coefficients for Equation (3.3), $A = a R_w d_w l_w (T_w - T_{ref})$ and $B = b R_w d_w l_w (T_w - T_{ref})$, the previous equation can written as,

$$E^2 = (A + BU^n) \; . \tag{3.4}$$

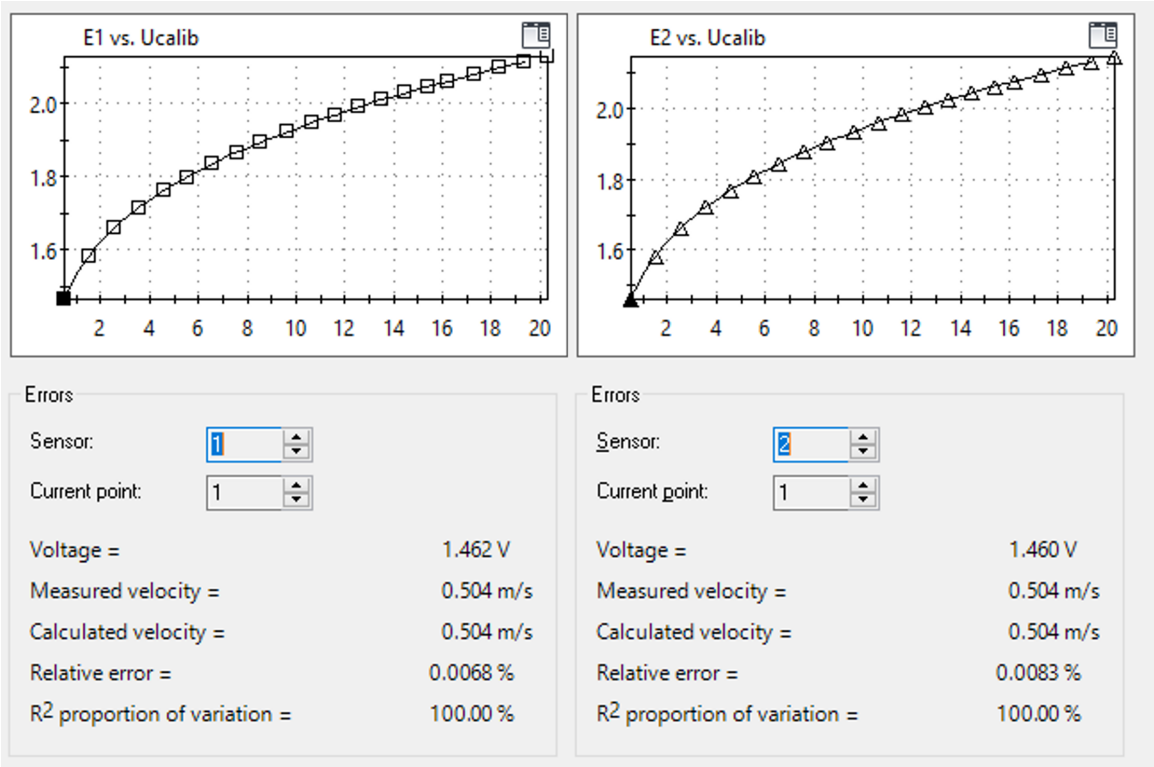

Figure 3.5: Example of a X-wire calibration.

Equation (3.4), known as the modified King's Law or power law, is used during the calibration of the hot-wire probe. The calibration consists of measuring the voltage of the wire in a small jet of known velocity. Another method of calibration fits a fourth order polynomial to the velocity-voltage curve. The method used for calibration of the hot-wire is the same as the one outlined in the *Dantec* practical guide for hot-wire measurement (Finn E. Jørgensen, 2002) where voltage and velocity are related by means of the modified King's law or a fourth order polynomial curve fit, of which the latter was used. The physical setup of the calibration can be seen in Figure 3.10.

Because a X-wire is used, a directional calibration must also be conducted to determine the yaw coefficients k_1^2 and k_2^2; these coefficients are used to calculate the velocity components in the coordinate system of the probe. The *Dantec* calibration module has an attachment which can move the probe to different angles with respect to the oncoming flow used for calibration. The probe was pitched from $-45°$ to $45°$ and the resulting graph is

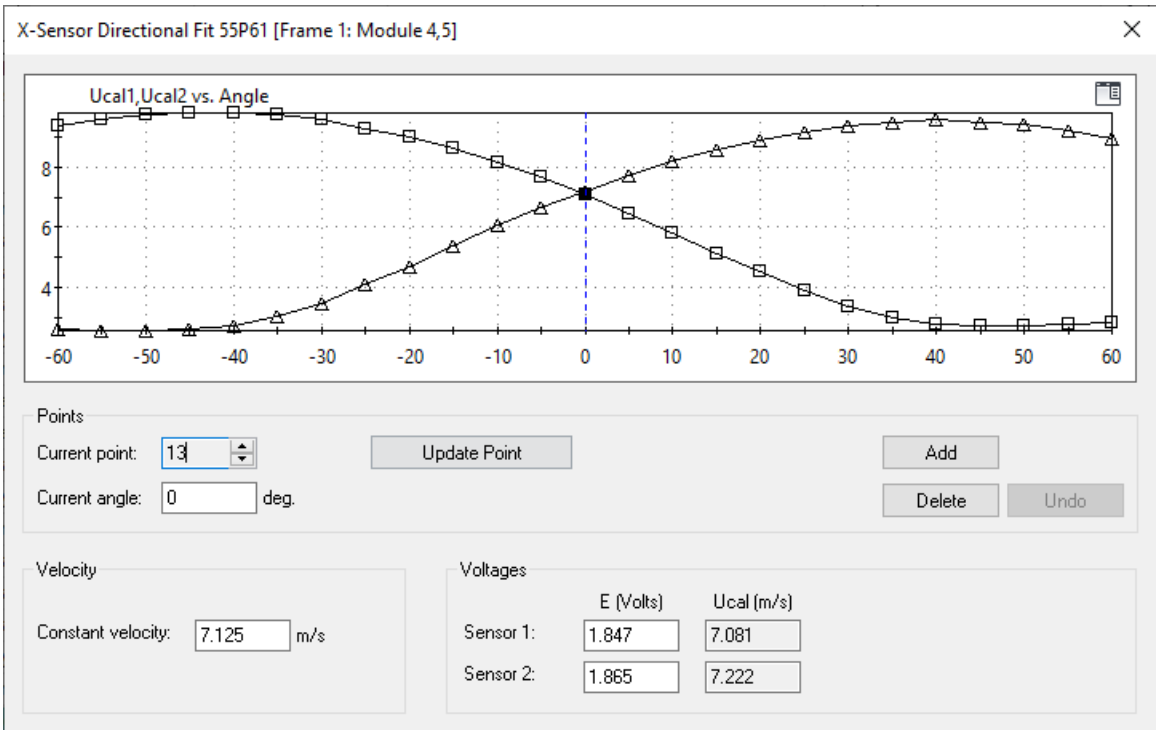

Figure 3.6: Pitching of probe to determine yaw coefficients.

shown in Figure 3.6. The obtained yaw coefficients were $k_1^2 = 0.0199$ and $k_2^2 = 0.0560$.

When measuring the velocity field with a X-wire there are two voltage time series being measured, E_1 and E_2. Using a 4 $^{\text{th}}$ order polynomial curve fit, E_1 and E_2 become U_{c1} and U_{c2}. To convert U_{c1} and U_{c2} into probe coordinates, U_1 and U_2, the yaw coefficients are used in Equation (3.5). In this study the author assumed $\alpha \approx 45°$, although there exist more accurate methods which do not rely on this assumption for α (Browne et al., 1988). To obtain U and V, the components of velocity in the coordinates of the wind tunnel, Equation (3.6) is used. Figure 3.8 illustrates the relationship between the two coordinate systems.

$$\begin{aligned} U_1 &= \frac{\sqrt{2}}{2}\sqrt{(1+k_2^2)U_{c2}^2 - k_2^2 U_{c1}} \\ U_2 &= \frac{\sqrt{2}}{2}\sqrt{(1+k_1^2)U_{c1}^2 - k_1^2 U_{c2}} \end{aligned} \tag{3.5}$$

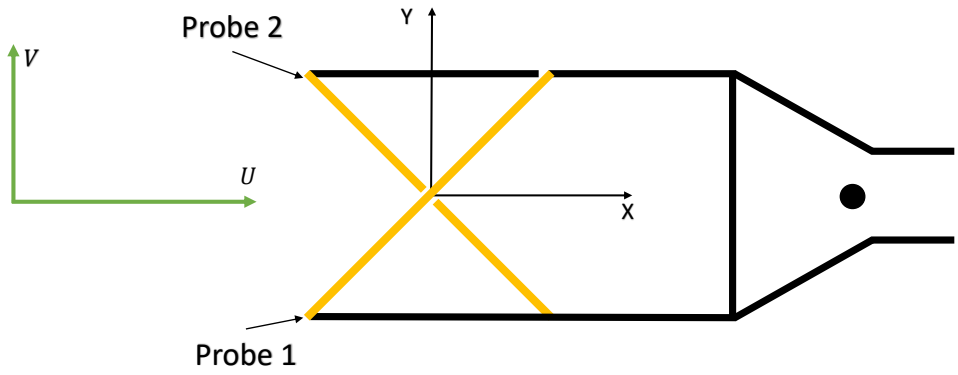

Figure 3.7: An example of a X-wire probe, based off an example provided by Finn E. Jørgensen (2002).

$$U = \frac{\sqrt{2}}{2}(U_1 + U_2)$$
$$V = \frac{\sqrt{2}}{2}(U_1 - U_2) \tag{3.6}$$

Before and after each test, or every 2 hours (which ever came first), a new calibration was preformed. The two calibrations, performed before and after each experiment, are used to obtain an average calibration data set. An example of two calibrations, performed within 1 hour 9 minutes of one another, is shown in Figure 3.9, which had a max percentage difference of 0.2015%. The converted velocity, U_c, is an average of the resulting velocities from the two calibrations taken before and after the experiment.

3.1.2 Hardware

The hot-wire probe used in this study was a *Dantec 55P61* miniature cross wire. The small size of the probe gives a high spatial resolution: the Platinum-plated tungsten wires have a diameter of 5 µm and are 1.25 mm long. The wire spacing is approximately 0.88 mm[1] and the wires are mounted on a 33 mm long ceramic tube with a diameter of 2.3 mm. The probe was mounted to a long *Dantec* probe holder *55H25*; two 4 m long BNC cables, also from *Dantec* (*A1863*), were connected to the probe holder. A

[1]This is estimated assuming an inclined wire length of 1.25 mm, that the wires are mounted at 45°, and that the distance between the two wires is the same as the parallel distance between the two prongs i.e., $1.25\sin(45)$

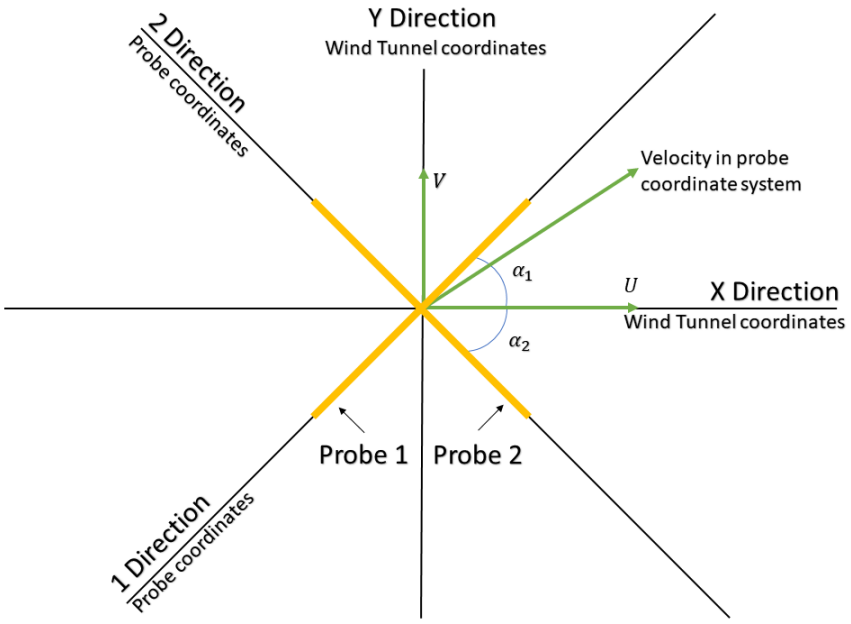

Figure 3.8: The probe coordinate system and the wind tunnel coordinate system.

Dantec Streamline 90H02 flow unit housed two CTA modules *91C10* and the Calibration module *90H01*. The A/D converter and data acquisition board used was a National Instruments *NI PCIe-6341* card connected to a *BNC-2110* Noise Rejecting, Shielded BNC Connector Block. The A/D converter is a 16-bit card with variable voltage input ranges, $\pm 0.2\,\mathrm{V}, \pm 1\,\mathrm{V}, \pm 5\,\mathrm{V}, \pm 10\,\mathrm{V}$, of which $\pm 10\,\mathrm{V}$ was used.. All of the hot-wire hardware was controlled by the *Dantec StreamWare* computer software. A gain of 1 and an offset of 0 V were used, this means the voltage measured accurately represents the power, or heat, lost from the probe to the fluid. With 16-bits the velocity resolution is 0.154% of full-scale at $5\,\mathrm{m\,s^{-1}}$, no more than $0.008\,\mathrm{m\,s^{-1}}$ of resolution error. For the cross wire, two channels were used for data acquisition. The card used has a maximum aggregate sampling rate of 500 kSamples/s for multiple channels; this results in 250 kSamples/s for each of the 2 channels used. For all tests, a sampling rate of 75 kHz was used for each sensor of the X-wire, well below the hardware's maximum capability, and data was sampled for 60 s at each measuring location.

The calibration procedure exposed the probe to velocities ranging from $0.5\,\mathrm{m\,s^{-1}}$ to $20\,\mathrm{m\,s^{-1}}$, which resulted in voltages of 1.4 V - 2.2 V, well within the operating range of the

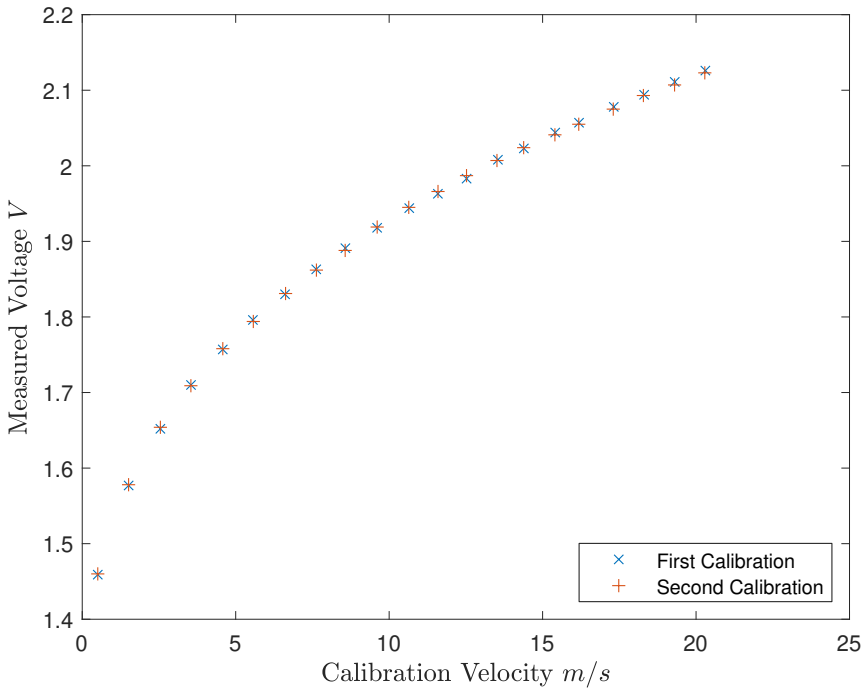

Figure 3.9: Comparison between two calibrations taken before and after an experiment. With 1 hour 9 minutes elapsed between calibrations.

A/D converter. The wind tunnel was only capable of producing velocities of $1.5\,\mathrm{m\,s^{-1}}$ up to $8\,\mathrm{m\,s^{-1}}$.

The hot-wires were operated at an overheat ratio of $a = 0.8$ with a sampling rate of 75 kHz and an analog low-pass filter set to 30 kHz; the sampling rate must be more than double the low-pass frequency to satisfy the Nyquist criterion. The Kolmogorov frequency, f_η, was assumed to lie below the 30 kHz low-pass frequency. An iterative method is used to find f_η in the post processing of data, with a fourth-order low-pass Butterworth filter applied to the data digitally at 1.3 times the Kolmogorov frequency. Additional data filtering was done following Burattini (2008) to account for the separation between the wires on the X-wire probe when estimating the mean of the directional velocity derivatives. These derivatives are used in the post processing to calculate some of the turbulence parameters described in Chapter 2. For the calculation of the integral length scale, an auto correlation was used to estimate the integral time scale and by extension, using Taylor's frozen flow hypothesis, to find the integral length scale. Error bars shown in the subsequent sec-

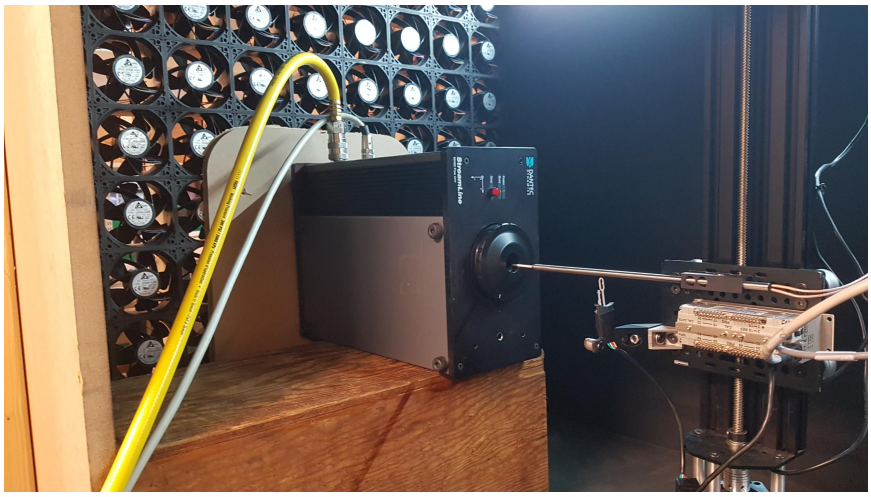

Figure 3.10: The physical calibration setup.

tions, where shown, represent the 95% confidence interval on the mean value based on the standard error, namely

$$\varepsilon_x = \frac{1.96\sigma_{\bar{x}}}{\sqrt{N}} \,, \tag{3.7}$$

where N is the number of samples, in this case $N = 60$, $\sigma_{\bar{x}}$ is the standard deviation of the means of each sample, and the 1.96 corresponds to the z-score for a normal distribution for a 95% confidence interval.

3.2 Fan Wall Configurations

For the present study, the fan wall's input system was wired to accept two different PWM signals. Each fan is fitted with a blue signal wire which, when sent a PWM, will modulate the RPM of the individual fan. Signal splitters were used to pass a PWM signal (PWM_1) to 41 fans, and a second PWM signal (PWM_2) to 40 fans. The convention used was that PWM_1 was always larger than PWM_2. The actual wiring was done in such a way to give adjacent fans different signals, similar to a checkerboard. In Figure 3.11, the dark fans are given signal one, the high signal, and the light fans are given signal two, the lower signal. Signal one always controlled the fans in each of the four corners and the center fan.

A series of data measurements were taken with the bulk flow kept constant at approx-

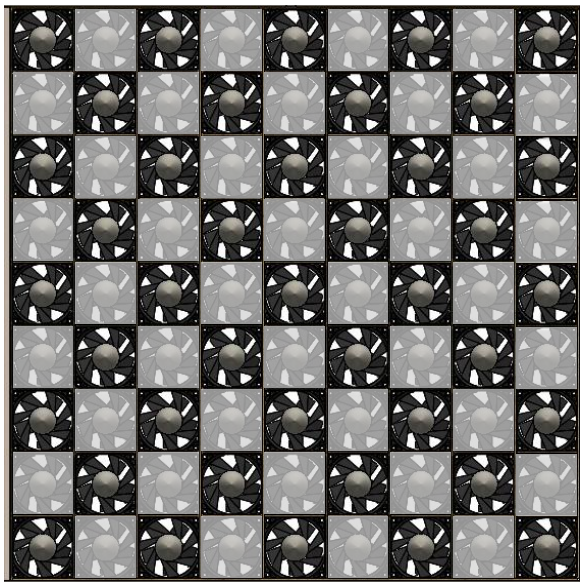

Figure 3.11: Wiring pattern of fan wall. Dark fans are given signal one, light fans are given signal two.

imately $5\,\mathrm{m\,s^{-1}}$, but with different shear ratios. We define the shear ratio

$$S_r = U_{\mathrm{high}}/U_{\mathrm{low}} \tag{3.8}$$

as the ratio between the highest U_{high} and lowest U_{low} velocity sent to the fan.The values of S_r tested were between 1.00 and 3.50, with a non linear spacing. The minimum value of S_r possible is unity and we can assume $S_r \to \infty$ for very low values of U_{low}. When the shear ratio is unity, all of the fans are spinning at the same speed. The physical interpretation for an infinite shear ratio would be a checkerboard pattern with only half of the fans on. The PWMs sent to the fans are shown in Table 3.1. These thirteen tests are the data sets presented in the following chapter.

Table 3.1: PWMs used to generate high and low velocities that average to $5\,\mathrm{m\,s^{-1}}$ and give the desired value of S_r.

S_r	U_{high} $\mathrm{m\,s^{-1}}$	PWM_1 %	U_{low} $\mathrm{m\,s^{-1}}$	PWM_2 %
1.00	5.00	53.5	5.00	53.5
1.05	5.13	55.0	4.87	52.5
1.10	5.24	56.5	4.76	51.5
1.25	5.56	59.5	4.44	48.0
1.50	6.00	64.0	4.00	43.0
1.75	6.36	67.0	3.64	40.0
2.00	6.67	69.0	3.33	37.0
2.25	6.92	71.0	3.08	34.0
2.50	7.14	76.0	2.86	32.0
2.75	7.37	83.0	2.66	30.0
3.00	7.50	91.0	2.50	28.0
3.25	7.65	95.0	2.35	26.5
3.50	7.78	98.0	2.22	25.0

Chapter 4

Results and Discussion

The streamwise evolution of turbulence statistics for 13 different shear ratios, while maintaining a constant bulk flow velocity at $5\,\mathrm{m\,s^{-1}}$, are presented. Preliminary measurements taken for streamwise locations $x \leq 500$ mm from the fan wall indicated that the turbulence intensity was greater than 20%. Since some of the post processing approximations required low turbulence intensities, the decision was made to set the starting streamwise location at $x = 550\,\mathrm{mm}$. See Chapter 2 for more information about these approximations. Streamwise measurements were therefore taken from 550mm $\leq x \leq$ 1750 mm, or $6.88 \leq x/M \leq 21.88$, where $M = 80$ mm, the diameter of the fans. The streamwise increments were 50 mm, or 0.62 M, which results in 25 streamwise measurement locations. For $S_r = 1.00, 2.00$ and 3.00, planar measurements were made in the vertical, y, and horizontal, z, directions for five downstream x locations: $x = 850\,\mathrm{mm}$, 1062 mm, 1275 mm, 1487 mm, and 1700 mm - or equivalently x/M = 10.62, 13.28, 15.94, 18.59, and 21.25.

The turbulent parameters of interest are the mean flow velocity, the turbulence intensity, the turbulent kinetic energy, the integral length scale of the flow, the Taylor-scale Reynolds number and the dissipation coefficient; all of these parameters were calculated using the methods described in Chapter 2.

4.1 Mean Flow Characteristics

The streamwise evolution of the normalized mean flow, $\overline{u}/U_\infty$, is shown in Figure 4.1 for $S_r = 1.00$ to 3.50, in increments of 0.50. Note that U_∞ is obtained by taking the mean of the last three streamwise locations. For $S_r > 1.00$, the mean flow moving downstream of the wind tunnel first increases then stabilize, whilst for the $S_r = 1$ case, the mean velocity develops differently, decreasing before appearing to stabilize. For all cases, the mean velocity data collapse to approximately unity for $x/M > 18$. Although the desired nominal bulk flow was $5\,\mathrm{m\,s^{-1}}$, it is observed that the mean flow velocity obtained was $U_\infty = 5.19 \pm 0.086$ for all 13 data sets, given to a 95% uncertainty interval. The convention $\overline{u_c}$ is used to denote the centerline velocity at each location i.e, at (x,0,0). The error of the mean velocity was analyzed, error bars are not included in the plots presented because the error is small for the mean velocity. Table 4.1 presents the maximum error for $\overline{u(t)}$ and $\overline{v(t)}$ across the entire streamwise direction of the wind tunnel, $6.88 \leq x/M \leq 21.88$.

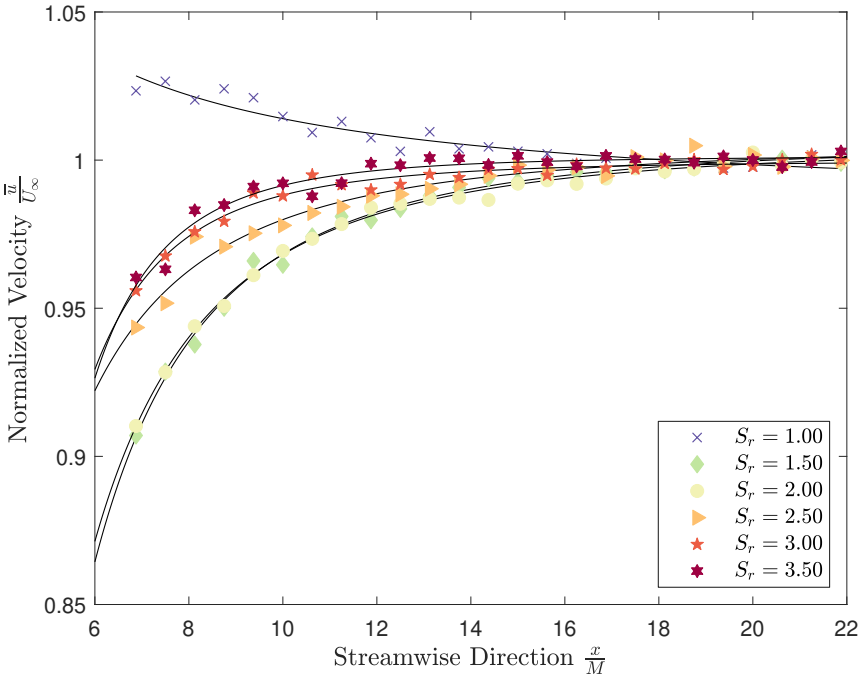

Figure 4.1: Profiles of streamwise mean flow development along the length of the wind tunnel.

Table 4.1: Maximum error bars for mean velocities across the entire streamwise direction of the wind tunnel, at 95 % uncertainty interval.

S_r	Max Error $\overline{u(t)}$ $\mathrm{m\,s^{-1}}$	Max Error $\overline{v(t)}$ $\mathrm{m\,s^{-1}}$
1.00	0.0398	0.0389
2.00	0.0231	0.0253
3.00	0.0280	0.0217

Uniformity of the Mean Flow

The variation of the planar normalized mean flow, $\overline{u}/\overline{u_c}$, in the vertical, y, direction is shown in Figure 4.2. A shear in the mean velocity is visible, with a faster mean flow

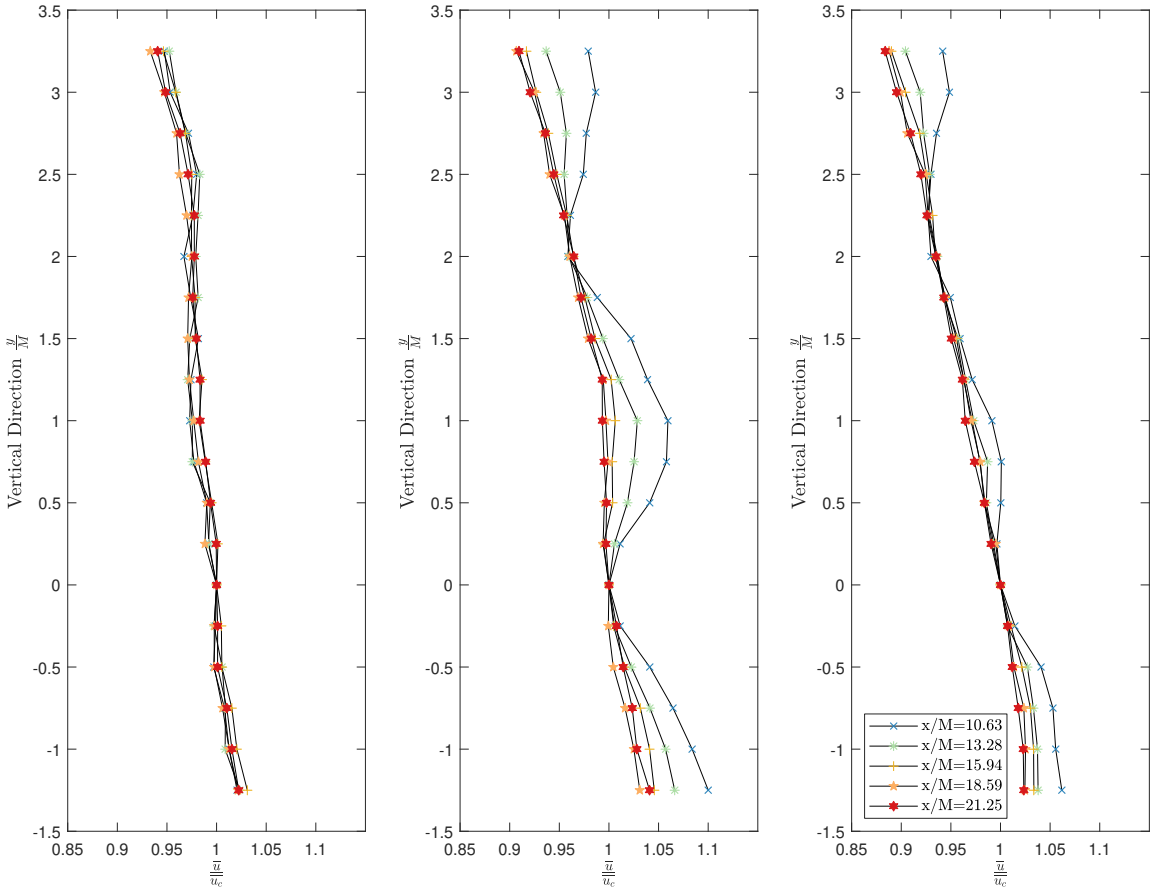

a) $S_r = 1.00$ b) $S_r = 2.00$ c) $S_r = 3.00$

Figure 4.2: Profiles of y direction mean flow normalized by $\overline{u}_c$ for positions along the length of the wind tunnel for various shear ratios.

observed for the lower half of the test section. During the preliminary construction phase of the facility, several attempts were made to correct/account for this mean shear. It was initially assumed that the traversing mechanism, which only covers the upper half of the wind tunnel may be a source of the shear, the mean flow would accelerate below the traverse. To investigate this, the the distance between the hot-wire probe and traverse was increased, however, no observable change in the mean shear was found. Secondly, there was a concern that the slot allowing the traverse to travel along the length of the test-section might be a source of the shear due to pressure losses; after covering the slot with tape, again no observable change was found. Lastly, the interface between the walls, ceiling and floor of the tunnel's test section were sealed. None of these methods, combined or individually tested, removed the element of shear cause by the change in velocity in the vertical y direction of the flow. One final possible source of the shear may be due to the power distribution system providing less power to the fans near the top of the fan wall; although the fans are connected in parallel, the electrical power is supplied from the bottom to the top fan i.e., the wire to the top fan is longer than the bottom fan, and hence the resistance might be slightly higher, thus causing a difference in electrical power. Estimates were made with regard to the resistance across the different lengths of wire, since the gauge of the wire was small, the difference in resistance was negligible. Verifying this possible cause is left as future work.

The variation of the mean flow in the z direction is shown in Figure 4.3, which indicates that the flow appears to be approximately uniform for $x > 13.28\,M$ for all shear ratios considered. Comparing to literature, Nedić and Tavoularis (2016b) found that uniformity was achieved between $8.5 \leq x/L_0 \leq 17.5$ for the various passive grids tested. It was expected that the sinusoidal variations present in the profiles of Figure 4.3 would have been larger for $S_r = 3.00$ but the results show the variations to be larger for $S_r = 2.00$, the reason for this is unknown.

In order to ascertain the importance of a mean velocity shear on the velocity field, we refer to the literature on uniformly sheared flow (USF). Although the present flow does not strictly indicate a uniform mean shear, being more sinusoidal in nature, one can still rely on the average velocity gradient of the flow to ascertain its relative importance. The measure

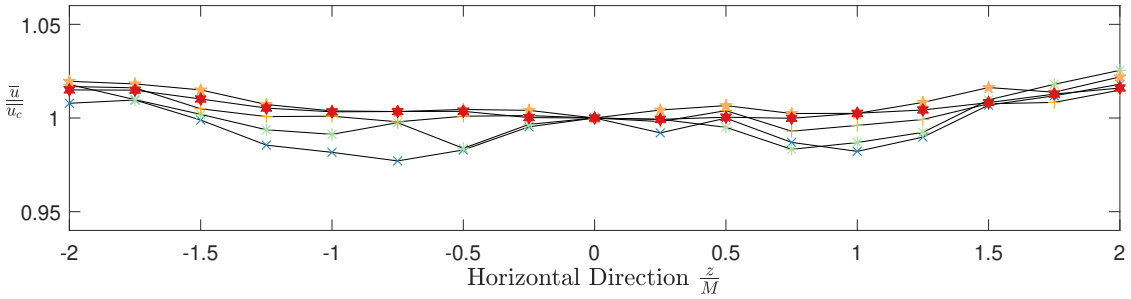

a) $S_r = 1.00$

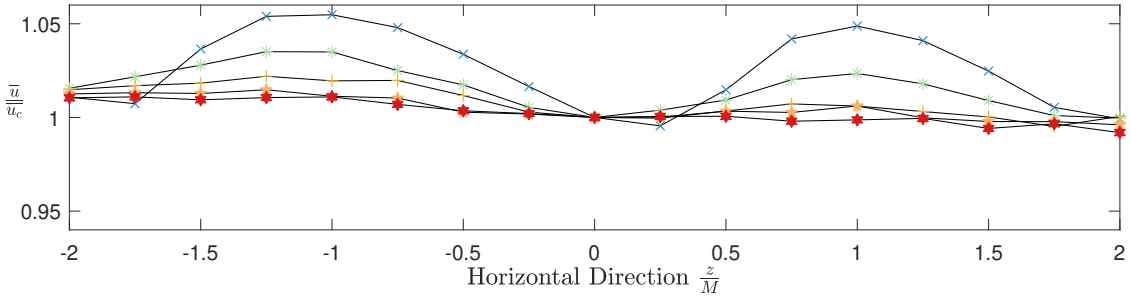

b) $S_r = 2.00$

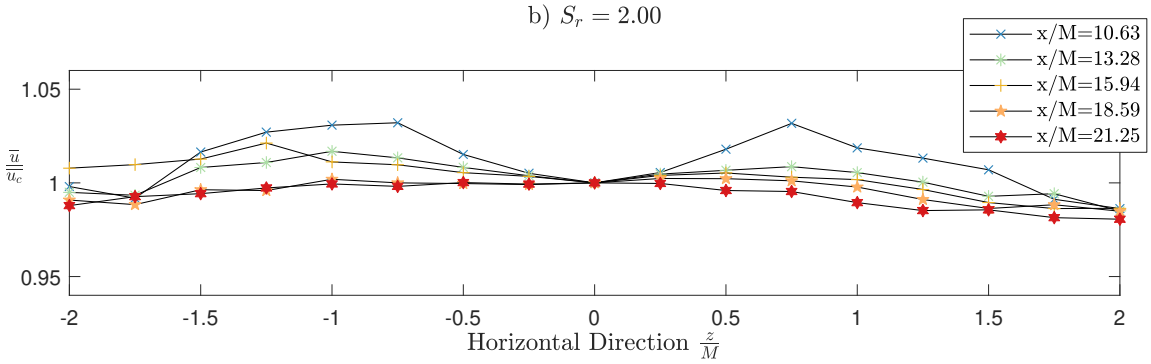

c) $S_r = 3.00$

Figure 4.3: Profiles of z direction mean flow normalized by $\overline{u}_c$ for positions along the length of the wind tunnel for various shear ratios.

of the strain imposed on the turbulence due to USF is denoted by τ,

$$\tau = k_s x = \frac{1}{\overline{u_c}} \frac{\mathrm{d}\overline{u}}{\mathrm{d}y} x \,. \tag{4.1}$$

where k_s is the flow generator constant and $\overline{u_c}$ is the center line velocity of the shear i.e., at (x,0,0). For values of $\tau < 4$, the shear is generally considered not to have an major

Table 4.2: Magnitude of τ, the influence of shear on the turbulent kinetic energy and turbulence.

S_r	$x/M = 10.63$	$x/M = 13.26$	$x/M = 15.94$	$x/M = 18.59$	$x/M = 21.25$
1.00	0.1779	0.2021	0.2390	0.2512	0.2306
2.00	0.2695	0.3500	0.3557	0.3468	0.3679
3.00	0.2860	0.3815	0.4104	0.3918	0.4024

influence on the turbulence being produced (Tavoularis and Karnik, 1989). A key difference between decaying grid-turbulence and USF is that for sufficient distances downstream of the generator, the turbulent kinetic energy grows for USF case, whereas it decays for grid-turbulence. Furthermore, even in the case where USF is distorted by a grid, the produced turbulence still exhibits grid like behaviour, as opposed USF-type behaviour (Nedić and Tavoularis, 2016a). The absolute values of τ were calculated for each of the cases tested, and are presented inTable 4.2; these values were obtained assuming a constant value of $\mathrm{d}\overline{u}/\mathrm{d}y$. Since the values of τ are less than 4, the shear seen in Figure 4.2 does not have a large impact on the turbulence being produced.

4.2 Evolution of Turbulent Properties

Turbulence Intensity

The streamwise evolution of the streamwise turbulence intensity, $I_1 = u_{rms}/U_\infty$, where $u_{rms} = \overline{u'^2}^{1/2}$, along the centerline of the tunnel, for all shear ratios, is shown in Figure 4.4. A clear monotonic decrease in turbulence intensity is observed for all shear ratios; there is also an apparent increase in turbulence intensity as the shear ratio increases. For example, an increase of 25.09 % was observed between $S_r = 1.00$ and $S_r = 3.50$ at $x/M = 6.875$, and an increase of 14.75 % was observed for the same change in shear ratios at the end of the tunnel where $x/M = 21.875$. The highest possible turbulence intensity level observed, within the spatial region considered here, was 17% for the $S_r = 3.50$ case, which decreased to roughly 5% at the farthest downstream position. Table 4.3 indicates the maximum relative error for both velocity components.

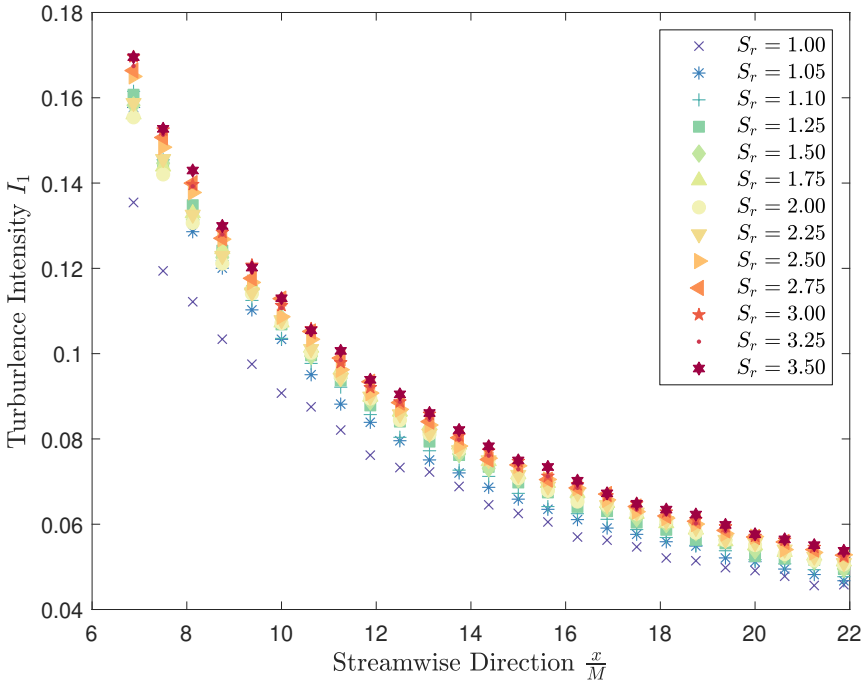

Figure 4.4: The development of Turbulence Intensity along the length of the wind tunnel, decaying Turbulence.

Large-scale isotropy

The large scale isotropy ratio u_{rms}/v_{rms}, along the centreline of the tunnel is shown in Figure 4.5. It is noted that it always lies between 0.95 and 1.08, which is similar to the values obtained by Comte-Bellot and Corrsin (1966) for grid generated turbulence with a straight duct, the same type of contraction-less tunnel used in the present study.

The reader is reminded that the presented results are immediately downstream of the fans, and that no filters, such as screens and honeycomb meshes, were used in the fan wall construction. The addition of these filtering devices would likely reduce the turbulence intensity at each downstream location in the tunnel, but the decision was taken to first investigate what turbulence levels the facility could produce without any flow conditioning.

Table 4.3: Maximum error bars for rms velocity across the entire streamwise direction of the wind tunnel, at 95 % uncertainty interval.

S_r	Max Error u'_{rms} %	Max Error v'_{rms} %
1.00	2.16	1.18
2.00	1.65	1.56
3.00	1.50	1.43

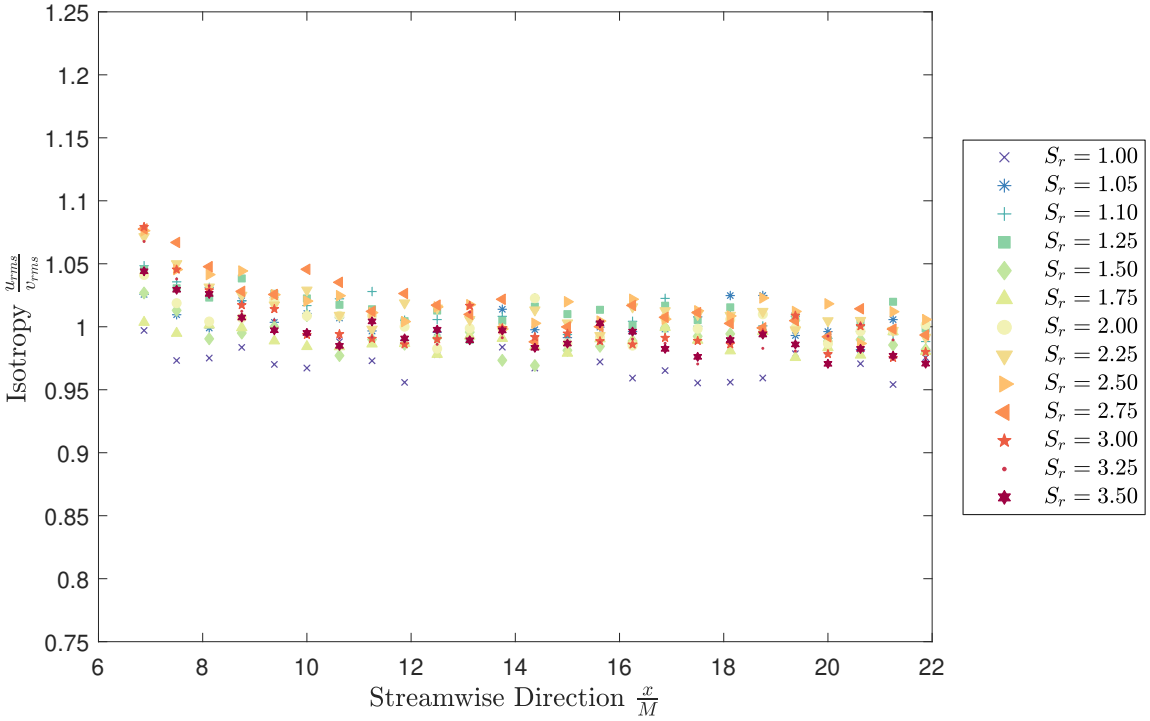

Figure 4.5: Isotropy along the length of the wind tunnel.

Homogeneity

The evolution of the normalized root mean square of velocity in the y and z direction is shown in Figure 4.6 and Figure 4.7. The flow is approximately homogeneous in the z direction (Figure 4.7) for all shear ratios and streamwise directions, with the highest levels of inhomogeneity observed at the closest location to the fans. In the y direction, Figure 4.6, the turbulence appears to be relatively homogeneous between $-1.25 \leq y/M \leq 2.5$ for all shear ratios and streamwise locations. A slightly sinusoidal variation is observed for the $S_r = 1.00$ case at the closest location of $x/M = 10.63$. For $y/M > 2.5$ there is a clear

increase in turbulence intensity, which progressively increases with streamwise distance and shear ratio. The source of this slight inhomogeneity is unknown at this point, but given that it increases with shear ratio suggests that it may be related to the operation of the fans the region $y/M > 2.5$. It is left as a future work to determine if this is indeed the case.

Turbulent Kinetic Energy

The turbulent kinetic energy $k = 0.5[\overline{u'^2} + 2\overline{v'^2}]$ (see Equation (2.6)), normalized by U_∞^2, is shown in Figure 4.9. When plotted in log-log scale, the linear decrease of the turbulent kinetic energy indicates a power law-type decay, which is similar to what is observed for decaying grid turbulence. The curves are divided into two regions, the near and far field,

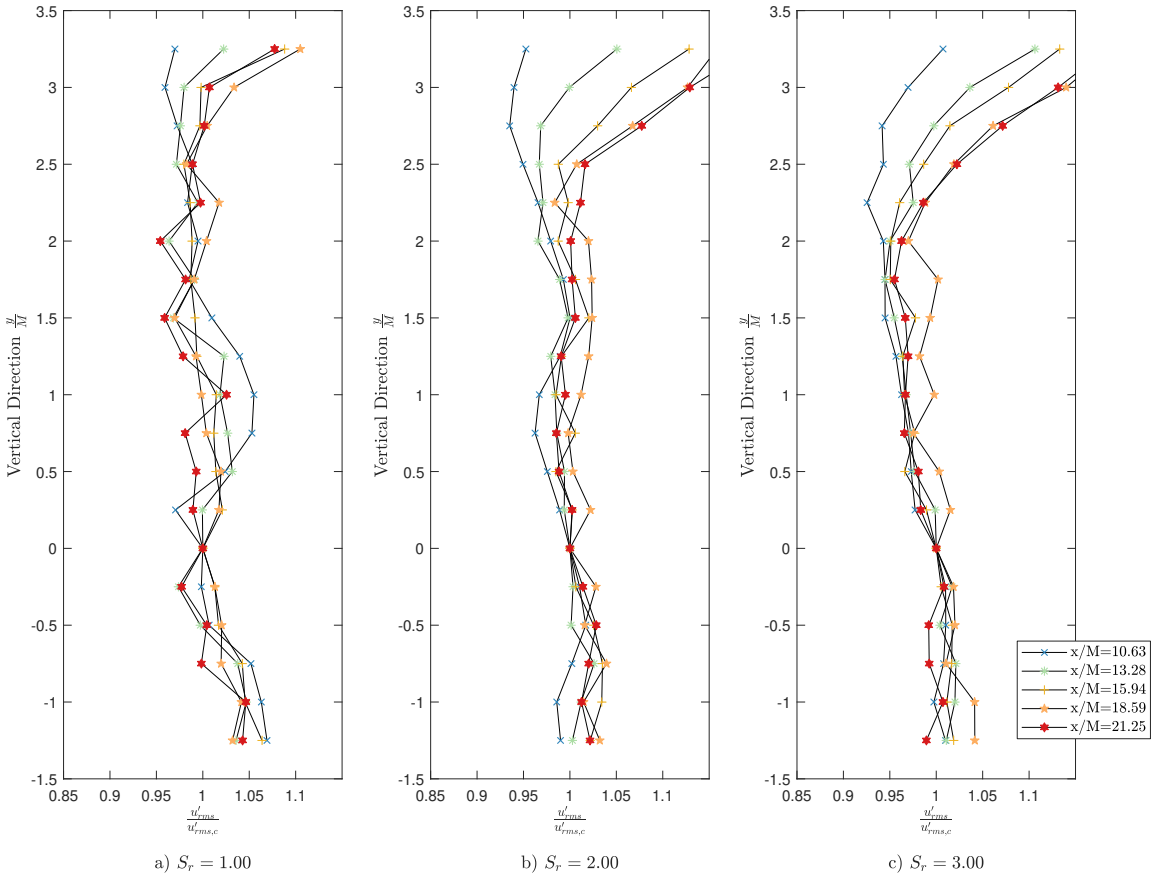

Figure 4.6: Profiles of y direction rms velocity normalized by the centerline rms velocity along the length of the wind tunnel for various shear ratios.

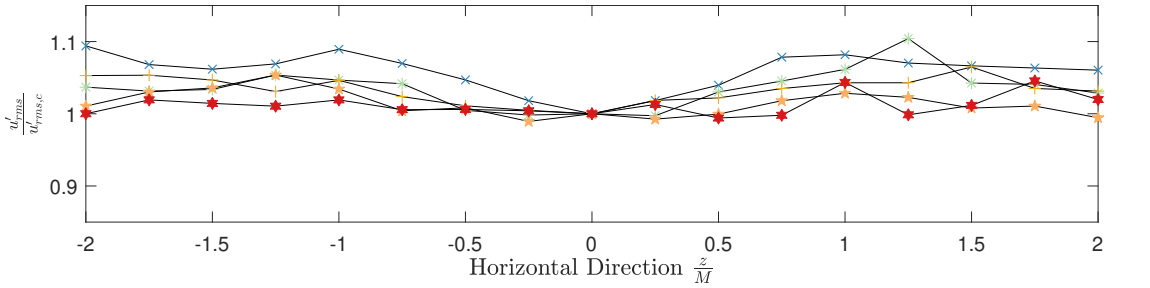

a) $S_r = 1.00$

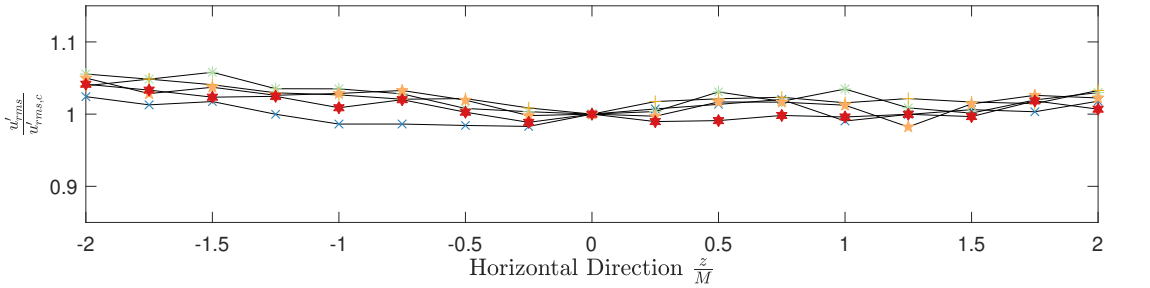

b) $S_r = 2.00$

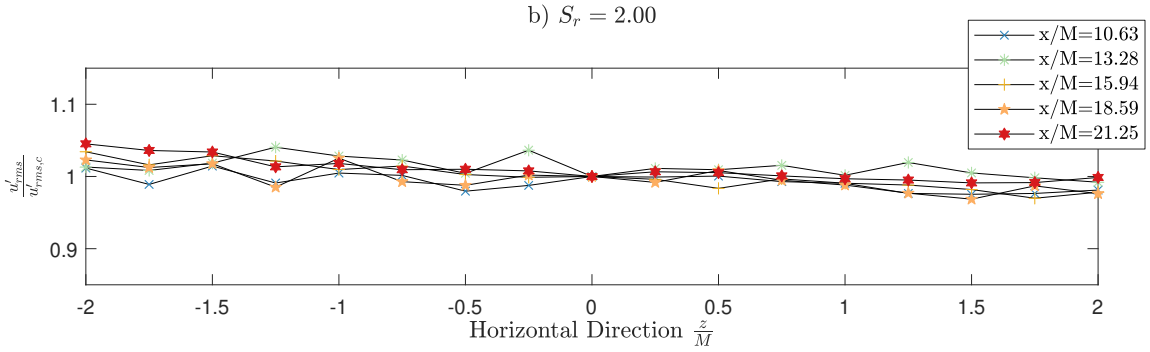

c) $S_r = 3.00$

Figure 4.7: Profiles of z direction rms velocity normalized by the centerline rms velocity along the length of the wind tunnel for various shear ratios.

the gap in the curves represents the approximate region where these regions are separated; the methodology used to find these regions is explained in the following paragraph.

Given the apparent power-law decay of the turbulent kinetic energy, and its similarities to decaying grid-turbulence, we fit the data using Equation (2.36), namely

$$\frac{k}{U_\infty^2} = A\left(\frac{x-x_o}{M}\right)^{-n}.$$

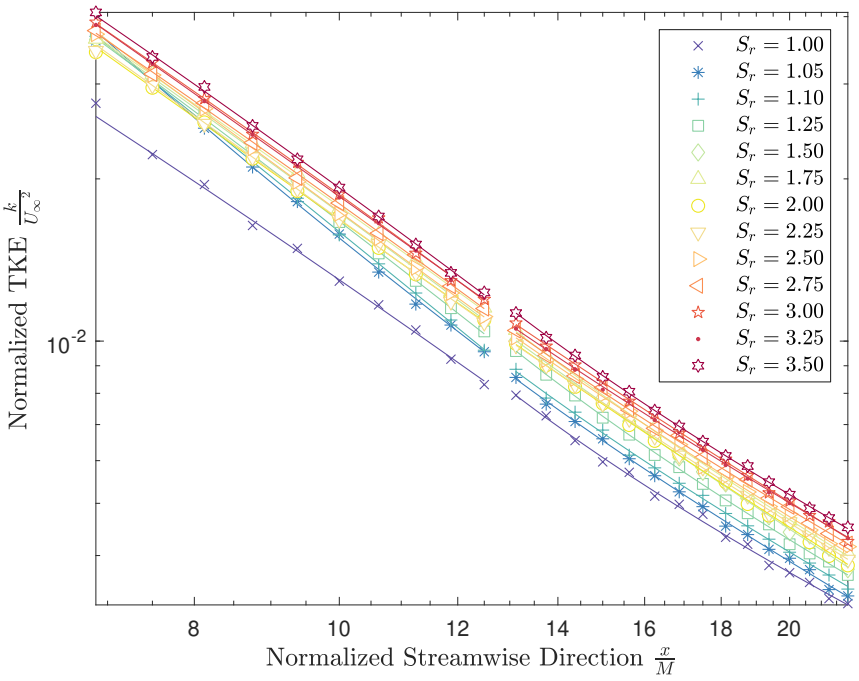

Figure 4.8: The normalized TKE Plotted in log-log.

It was decided to use the algorithm outlined in Valente and Vassilicos (2011), which itself draws from the method used by Lavoie et al. (2007). Briefly, the algorithm works as follows, a non-linear least squared algorithm is used to determine the virtual origin and decay exponent simultaneously. The reason for using this algorithm was to determine if multiple regions of the flow had different virtual origins and decay exponents. The the near field was determined by fitting Equation (2.36) from the first streamwise location to the second, and then adding one point at a time to observe when the error of the non-linear least squares fit increases for a given decay exponent and virtual origin. The separation between the regions was selected as $\frac{x}{M} = 12.5$, it is after this location where the error of the curve fit increases. Going backwards, performing a curve fit on the last two points and adding additional points going backwards yielded increasing error in the fit up until approximately the same region where $\frac{x}{M} = 12.5$. The results of all of the curve fits are presented in Figure 4.9 and the log-log plot of the same data is presented in Figure 4.8.

The virtual origin and decay exponent for each of the shear ratios, and for each of the two different regions, is shown in Table 4.4. In the near field, the decay exponent ranged

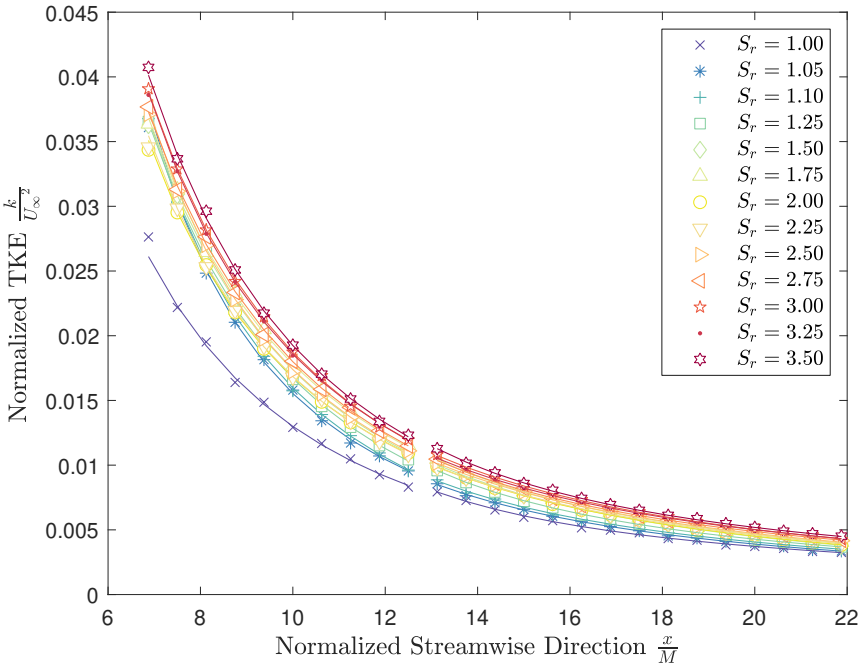

Figure 4.9: The normalized TKE with $\frac{k}{U_\infty^2} = A(\frac{x-x_o}{M})^{-n}$ fitted to the near field and far field regions of the flow.

Table 4.4: Calculated decay exponent and virtual origin for the development of the TKE in the near field and far field regions.

	Near Field		Far Field	
S_r	x_0/M	n	x_0/M	n
1.00	-1.44	2.002	6.49	1.064
1.05	1.99	1.860	4.81	1.292
1.10	-0.31	2.312	5.11	1.244
1.25	-1.13	2.375	5.92	1.202
1.50	-0.98	2.233	3.13	1.582
1.75	-1.04	2.186	4.92	1.321
2.00	0.27	1.901	2.71	1.541
2.25	0.12	1.959	2.25	1.549
2.50	0.49	1.929	3.19	1.453
2.75	-1.23	2.232	4.49	1.288
3.00	-1.48	2.297	2.47	1.524
3.25	-0.19	2.01	3.78	1.347
3.50	-1.58	2.337	5.80	1.172

Table 4.5: Calculated decay exponent using the average value of virtual origin obtained in Table 4.4; $x_0 = -0.50M$ in the near field and $x_o = 4.24M$ for the far field.

	Near Field	Far Field
S_r	n	n
1.00	1.988	1.323
1.05	2.371	1.353
1.10	2.362	1.356
1.25	2.214	1.403
1.50	2.127	1.407
1.75	2.068	1.403
2.00	2.062	1.380
2.25	2.079	1.327
2.50	2.138	1.337
2.75	2.082	1.314
3.00	2.084	1.329
3.25	2.071	1.301
3.50	2.097	1.335

between $1.78 \leq n \leq 2.37$, with an average value of $n = 2.13$, whilst the virtual origin ranged between $-1.58 \leq x_o/M \leq 1.99$, with an average value of $x_0 = -0.50M$. In the far field, the decay exponent ranged between $1.064 \leq n \leq 1.549$, with an average of $n = 1.349$, and the virtual origin ranged between $2.25 \leq x_0/M \leq 6.49$, with an average value of $x_o = 4.24M$. As discussed in Chapter 2, these results are in accordance with those values observed for grid turbulence(Comte-Bellot and Corrsin, 1966; Hearst and Lavoie, 2014; Lavoie et al., 2007; Valente and Vassilicos, 2011, 2015). In particular, it is noted that the virtual origin in the near field of grid generated turbulence is negative, and positive in the far field.

Table 4.5 presents the decay exponent for a fixed virtual origins of $x_0 = -0.50M$ in the near field and $x_o = 4.24M$ for the far field; both are the averages of the virtual origins shown in Table 4.4. The average value of the decay exponent in the near field is $n = 2.134$, the range of decay exponents for varying shear ratios is smaller than the previous case using a variable virtual origin, $1.988 \leq n \leq 2.372$. For the far field, the decay exponent was $n = 1.351$ and the range for changing shear ratio was also smaller compared to the case of varying the virtual origin, $1.301 \leq n \leq 1.407$.Given the clear dependence of the shear ratio on the magnitude of the turbulent kinetic energy, it seems reasonable to assume that the scaling factor would be a function of it i.e., $A = \text{fn}(S_r)$. The values of A, as a function

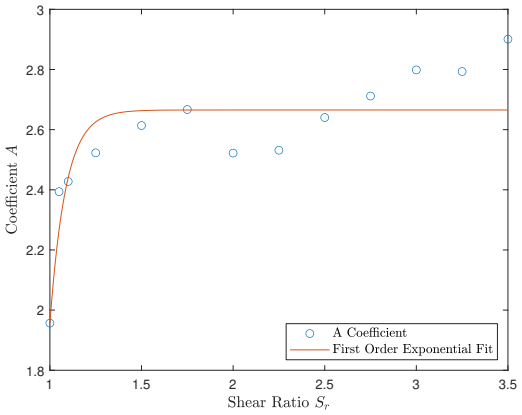

(a) Development of scaling factor A in the near field.

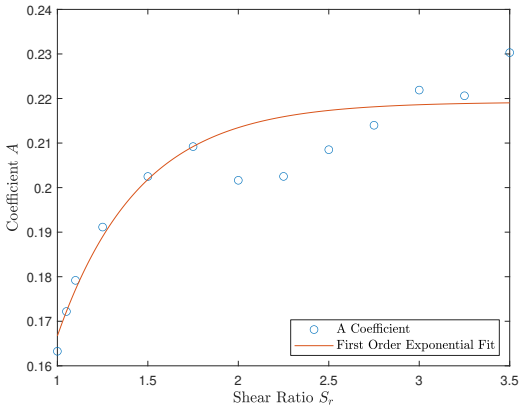

(b) Development of scaling factor A in the far field.

Figure 4.10: Development of scaling factor A.

of the shear ratio, are shown in Figure 4.10. Using the average value of x_o and the average value of n in each region, an estimate for A can be made. The equation,

$$A = a\exp\left(-bS_r\right) + c\ ,$$

was used. For the near field $a = -7.034 * 10^4, b = 11.51$, and $c = 2.665$. For the far field, $a = -0.478, b = 2.208$ and $c = 0.219$. The RMSE uncertainty of these curve fits 0.1265 and 0.0076 for the near and far field respectively.

From the results presented, it is apparent that the turbulence generated by the MFWT is similar to that observed in decaying grid turbulence. In particular, it has been shown that the turbulence is homogeneous and isotropic, exhibiting decay exponents of the turbulent kinetic energy that are comparable to those observed in grid turbulence, both in the near and far field.

4.3 Probability Density Functions

The probability density functions for all shear ratios are shown in Section 4.3 for two downstream locations: one in the near field at a streamwise distance of $x = 10M$, and in the far field at a streamwise distance of $x = 21.25M$. It is noted that the PDFs appear Gaussian,

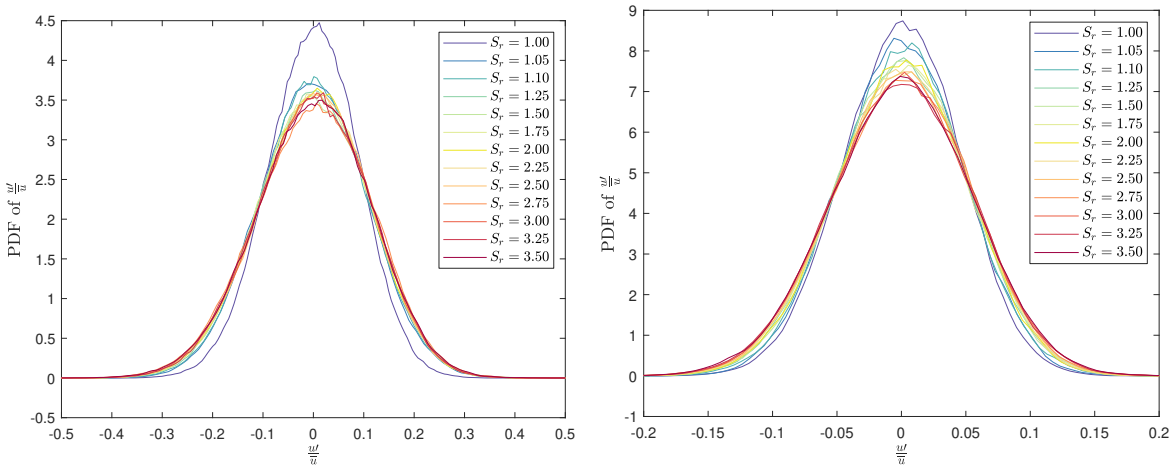

(a) The PDF at $x/M = 10$.

(b) The PDF at $x/M = 21.25$.

Figure 4.11: The probability density functions of u' normalized by the mean velocity, close and far from the fan wall.

however, there is a clear dependence of the shear ratio on the shape of the PDF. The peak of the PFDs appear to decrease as the shear ratio increases, this is particularly true for the case where the shear ratio was unity.

In order to test how close the PDFs were to Gaussian, the kurtosis and skewness were calculated. The kurtosis and skewness are very close to 3 and zero, respectively, for all 13 shear ratios, as shown in Figure 4.12.

The joint PDFs (J-PDFs), between the two velocity components, are shown in Figure 4.13 and Figure 4.14, again for both close and far from the fan wall, and for $S_r = 1.00, 2.00$ and 3.00. The case of $S_r = 3.00$ shows a slightly oval profile in the J-PDF, which is an indication that there is a slight correlation between u' and v', the fluctuating components of the velocity. Even with the presence of the slight oval shape, these results confirm that the velocity fluctuations in u and v are close to being uncorrelated, in other words the velocity fluctuations are random. A necessary condition of isotropy is having u' and v' be uncorrelated, although it is not a sufficient condition, as anisotropic flows can also have u' and v' be uncorrelated.

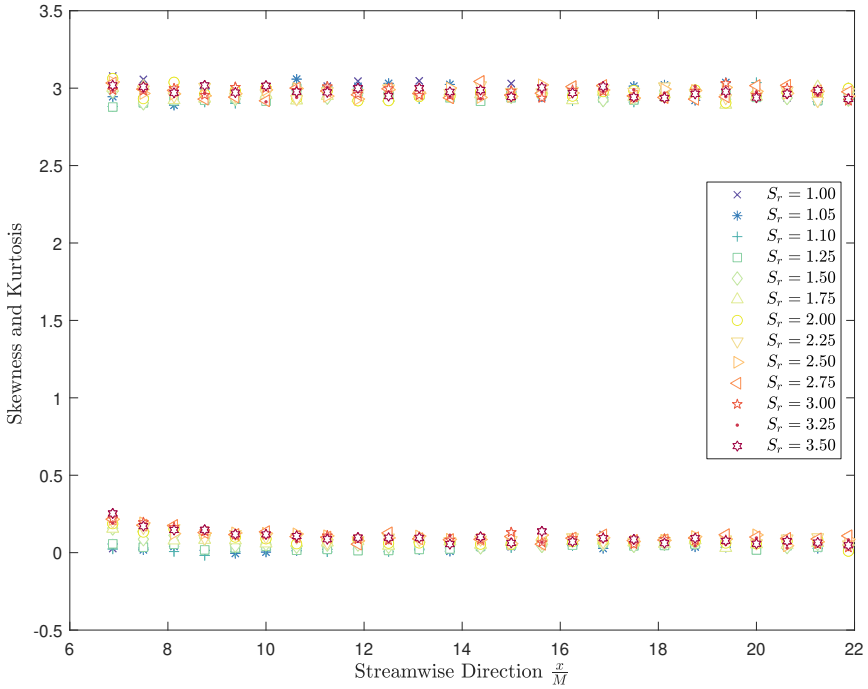

Figure 4.12: The Skewness and kurtosis at each downstream location for all S_r.

4.4 Estimated Turbulent Parameters

Taylor-Microscale

The streamwise development of the normalized Taylor-microscale is shown in Figure 4.15, where two distinct linear regions are observed, demarcated at $x/M \approx 12$. The development of the Taylor-microscale also appears to decrease somewhat as S_r increases. With the exception of $S_r = 1.00$, as the magnitude of the shear ratio increases, the approximate value of the Taylor-microscale appears to decrease. This is more noticeable for the measurements made closer to the fan wall.

Integral Length Scale

The integral length scale was calculated using the autocorrelation function, then fitting a 2^{nd} order exponential function to the discrete data using a least squares curve fit algorithm. The integral between $t = 0$ and $t = \infty$ of the 2^{nd} order exponential function

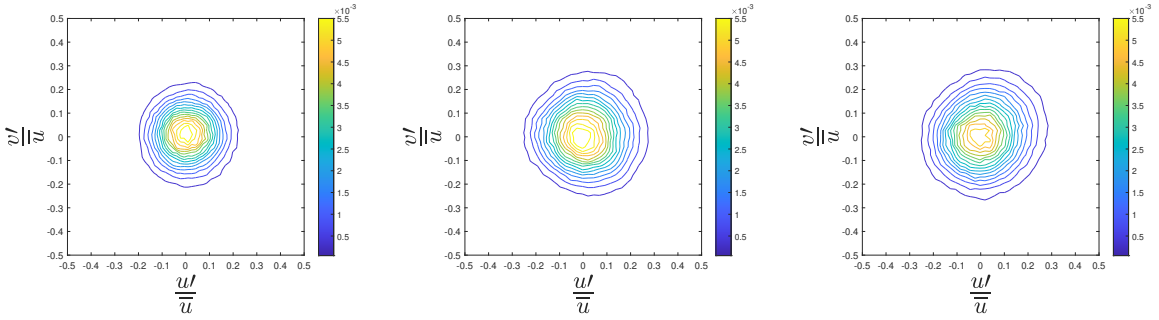

(a) J-PDF close to fan wall for $S_r = 1.00$

(b) J-PDF close to fan wall for $S_r = 2.00$

(c) J-PDF close to fan wall for $S_r = 3.00$

Figure 4.13: Joint PDFs for $S_r = 1.00, 2.00$ and 3.00 at $x/M = 10$.

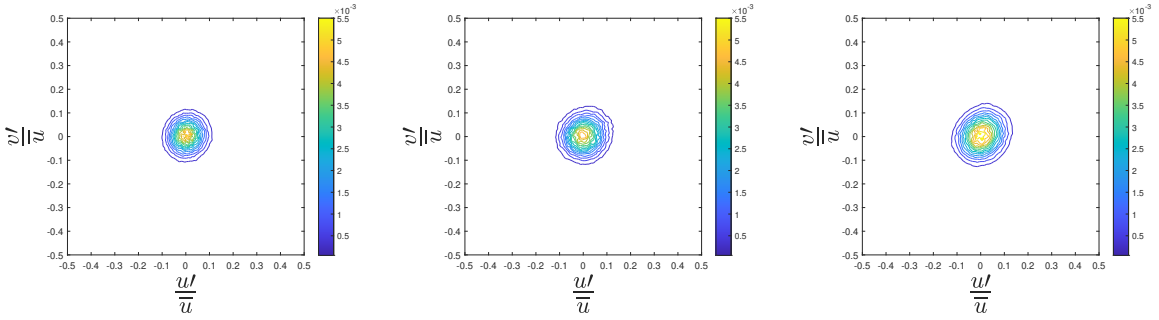

(a) J-PDF far fan wall for $S_r = 1.00$

(b) J-PDF far fan wall for $S_r = 2.00$

(c) J-PDF far fan wall for $S_r = 3.00$

Figure 4.14: Joint PDFs for $S_r = 1.00, 2.00$ and 3.00 at $x/M = 21.25$.

was then calculated using the estimated continuous function. Using Taylor's frozen flow hypothesis, the integral length scale was found. To minimize error, this process was performed on 60, one second data sets in order to obtain an average value for the integral length scale. The error bars in Figure 4.16 are calculated using the 60 calculated integral length scales for 95% uncertainty intervals.

The streamwise evolution of $L_{11,1}/M$ is shown in Figure 4.16, where it is observed to increase with streamwise distance, and that at the farthest streamwise location the integral scale is less than half the fan size $L_{11,1} < 0.5M$. Moreover, a clear trend is observed with regards to the effects of shear ratio: as the shear ratio increases, there integral scale increases. As an example, the variation of the integral scale with shear ratio, at $x = 10.625M$ (near field) and $x = 20.25M$ (far field) is shown in Figure 4.17. It can be seen that the integral

scale increases by 25.3% in the near field and 15.3% in the far field region for an increase of $S_r = 1.00$ to $S_r = 3.50$. Even when taking the error bars into account, shear ratios larger than $S_r = 1.00$ will greatly increase the magnitude of $L_{11,1}/M$ in both the near and far field regions

Taylor-Scale Reynolds Number

The estimation of Re_λ is determined using the r.m.s. velocity, the Taylor-microscale and the viscosity. The Taylor-microscale, λ, was estimated using the relation, $\lambda/u_{rms} = \sqrt{15\nu/\varepsilon}$, which is an isotropic relation. The dissipation rate, ε, was calculated using the velocity derivatives of both velocity components,

$$\varepsilon = 3\nu \left[\overline{\left(\frac{\partial u}{\partial x}\right)_c^2} + 2\overline{\left(\frac{\partial v}{\partial x}\right)_c^2} \right] . \tag{4.2}$$

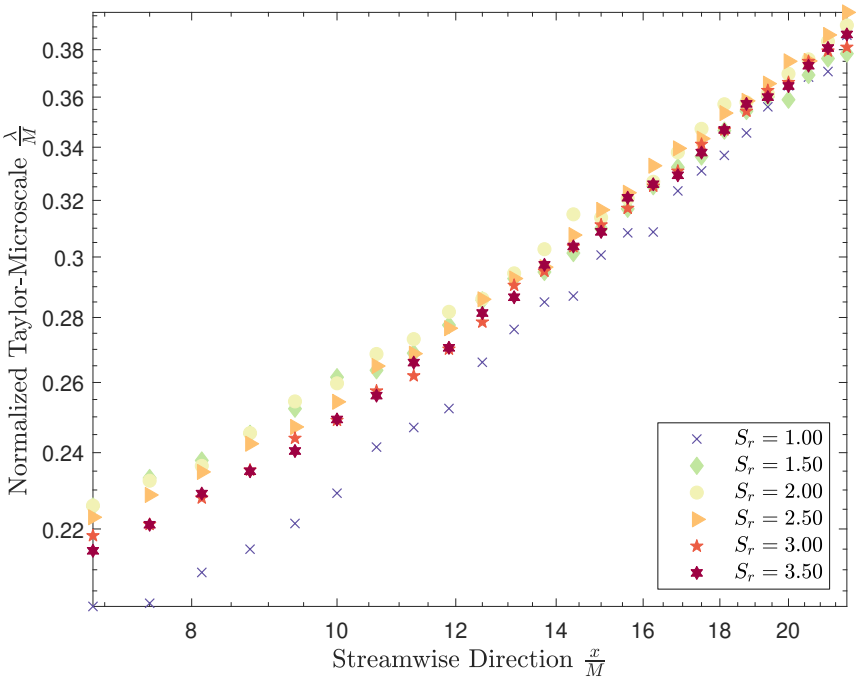

Figure 4.15: Development of the Taylor-Microscale, λ.

Note that the subscript c denotes the corrected velocity derivatives proposed by Burattini (2008). The results indicate that the Taylor-scale Reynolds number increases with shear ratio, as shown in Figure 4.19 for two downstream locations. The maximum magnitude of $\mathrm{Re}_\lambda \approx 180$ (see Figure 4.19) is lower than what can be achieved using active grids, or large passive grids, it is, however, comparable to previous grid turbulence studies (Comte-Bellot and Corrsin, 1966; Lavoie et al., 2007; Nedić and Tavoularis, 2016b). Having a moderate Taylor-scale Reynolds number also indicates a narrow inertial sub-range compared to a spectra obtained using an active grid, the inertial sub-range can be seen in Figure 4.20.

4.5 Spectra

The one-dimensional energy spectra $E_{11}(\kappa_1)$, or power spectral density, can be determined from the stationary and ergodic time series of the measured velocity. The spectra for multiple shear ratios, both for a near field location $x/M = 10$ and a far field location $x/M = 21.25$, are shown in Figure 4.20. On each plot the theoretical Kolmogorov $-\frac{5}{3}$

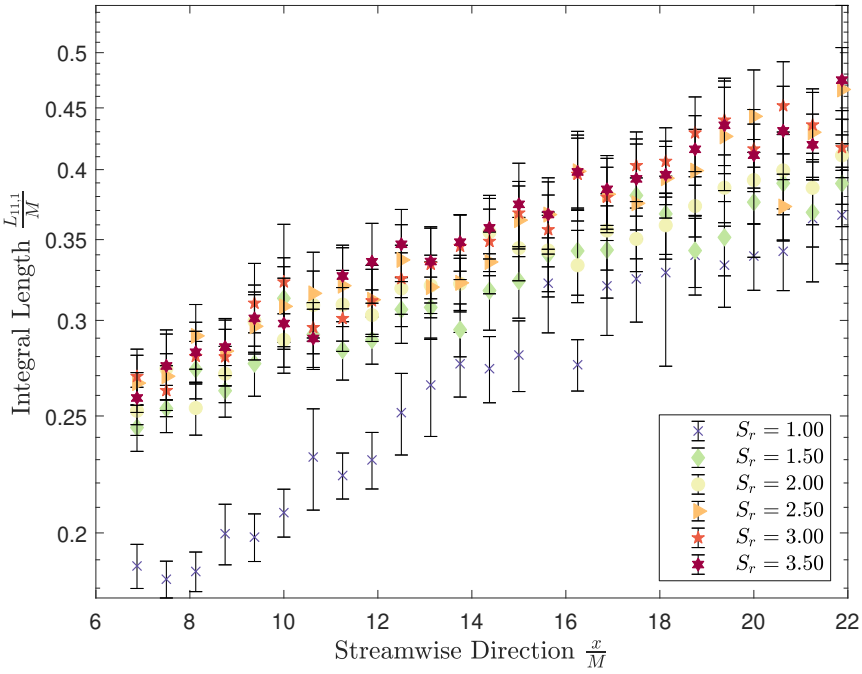

Figure 4.16: Development of the integral length scale, $L_{11,1}$.

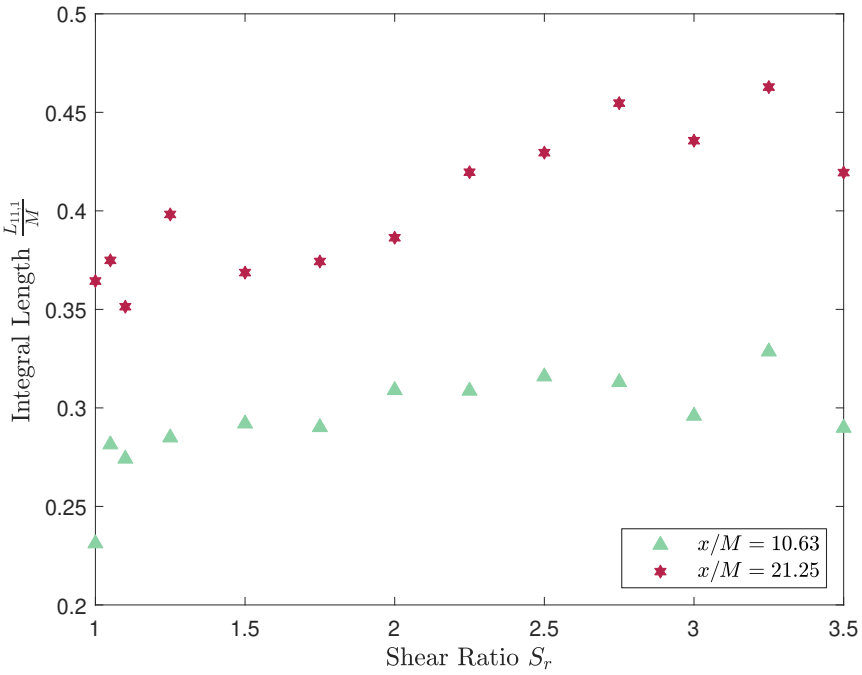

Figure 4.17: Evolution of $L_{11,1}/M$ for changing S_r at locations $x/M = 10.63$ and $x/M = 21.25$.

slope is shown as a dashed straight line above the inertial sub-range. For these plots, the wave number κ_1 was determined from the frequency using Taylor's frozen flow hypothesis: $\kappa_1 = \frac{2\pi}{\bar{u}} f$.

The spectra have an inertial sub-range comparable to lower Taylor-scale Reynolds numbers, with larger values of Re_λ the width of the inertial sub-range would be larger. At low wave numbers, roughly $\kappa_q \eta < 0.003$, the $S_r = 1$ case has lower energy content as compared to the higher shear ratio cases; this is true for both locations. The magnitude of the spectra at low wave numbers represent the magnitude of the integral scale obtained at the point in the flow being measured. The integral scale results agree with the spectra data, $S_r = 1.00$ produces a smaller integral scale compared to $S_r > 1.00$. The inertial sub-range for the cases where $S_r > 1.00$ is approximately one decade, and increasing the shear ratio above the threshold of $S_r = 1.00$ does not appear to have a difference on the width of the inertial sub-range of the resulting spectra.

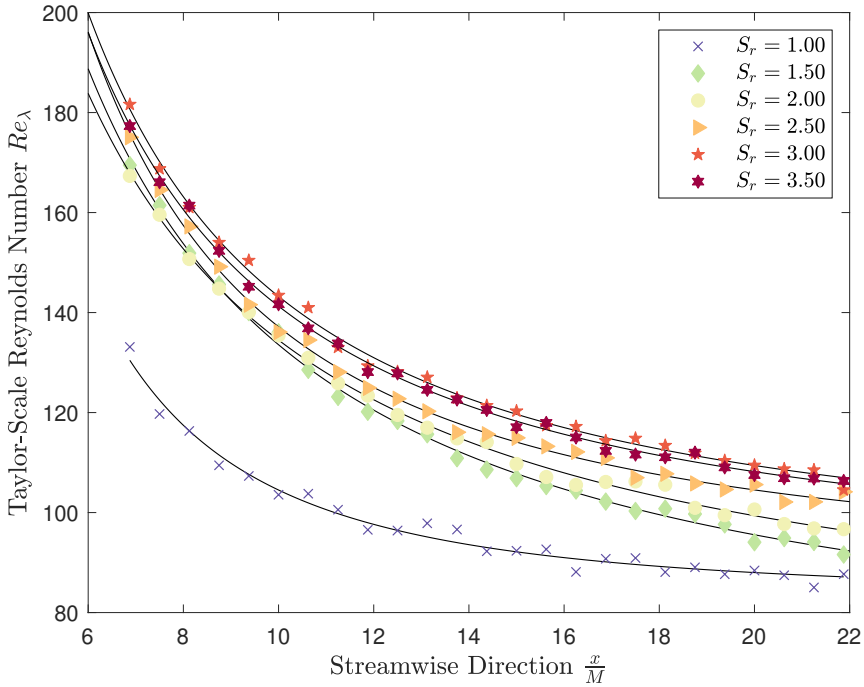

Figure 4.18: Estimation of Taylor-scale Reynolds number, Re_λ.

4.6 Dissipation Coefficient

Using the integral length scale, dissipation rate and turbulent kinetic energy, the dissipation coefficient can be estimated as $C_\varepsilon = \frac{\varepsilon L_{11,1}}{(2k/3)^{3/2}}$. The error bars from Figure 4.16 would obviously affect the estimate of C_ε in Figure 4.21, but the error bars were not included here to make the figure easier to read. From the region of $x/M = 6.875$ to $x/M \approx 14$ the dissipation C_ε is observed to increase, indicating a non-equilibrium region of the turbulence $\mathrm{d}k/\mathrm{d}t \neq \varepsilon$. Further downstream, it is less clear how C_ε is developing, however, from visual inspection C_ε appears to approximately constant. Previous studies (Hearst and Lavoie, 2014; Vassilicos, 2015) suggest a transition zone where C_ε transitions to a constant value in the far field, known as the equilibrium region. Singling out the highest shear ratio, $S_r = 3.50$, there appears to be a strong suggestion that the development, transition and steady regions of C_ε are present, as shown in Figure 4.22. Note that these observations hold regardless of the uncertainty in the integral scale.

This non-equilibrium region has also been observed in grid turbulence, jets, wakes,

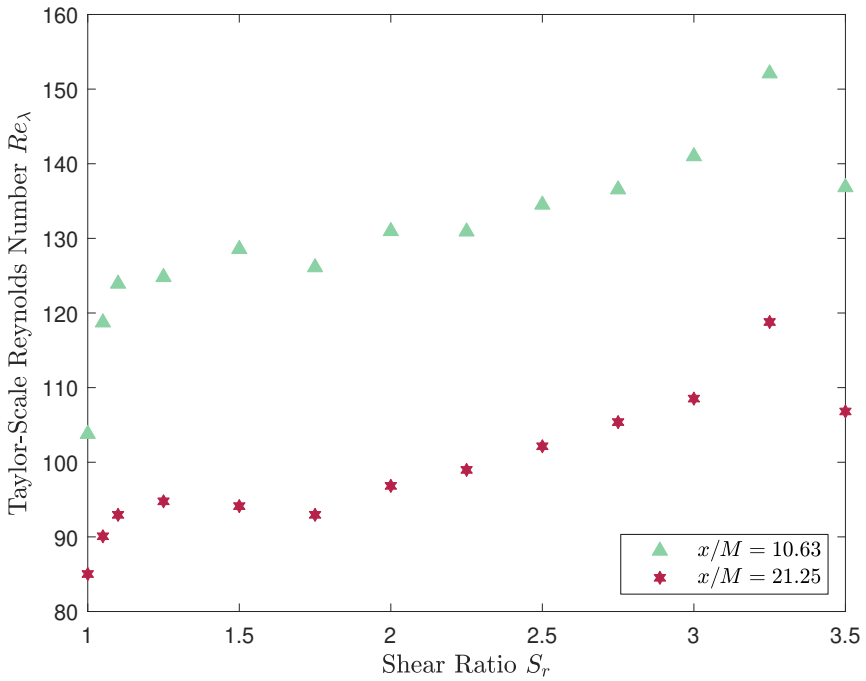

Figure 4.19: Evolution of Taylor-scale Reynolds number for changing S_r at locations $x/M = 10.63$ and $x/M = 21.25$.

uniformly sheared flow and boundary layer flow. In the majority of the previously mentioned turbulent shear flows, it has been observed that $C_\varepsilon \sim Re_\lambda^{-1}$(Vassilicos, 2015), except for the uniformly shear flow case, where $C_\varepsilon \sim Re_\lambda^{-0.6}$(Nedić and Tavoularis, 2016a). The variation of C_ε with Re_λ, for several shear ratios, is shown in Figure 4.23 in log-log scale. The linear variation of these two parameters indicates that there is a power law relation between the two, and the gradient of -1, shown as a dashed line, indicates that they are inversely proportional to each other. Therefore, turbulence generated in a MFWT does exhibit non-equilibrium turbulence, which is similar to non-equilibrium turbulence generated in decaying grid turbulence.

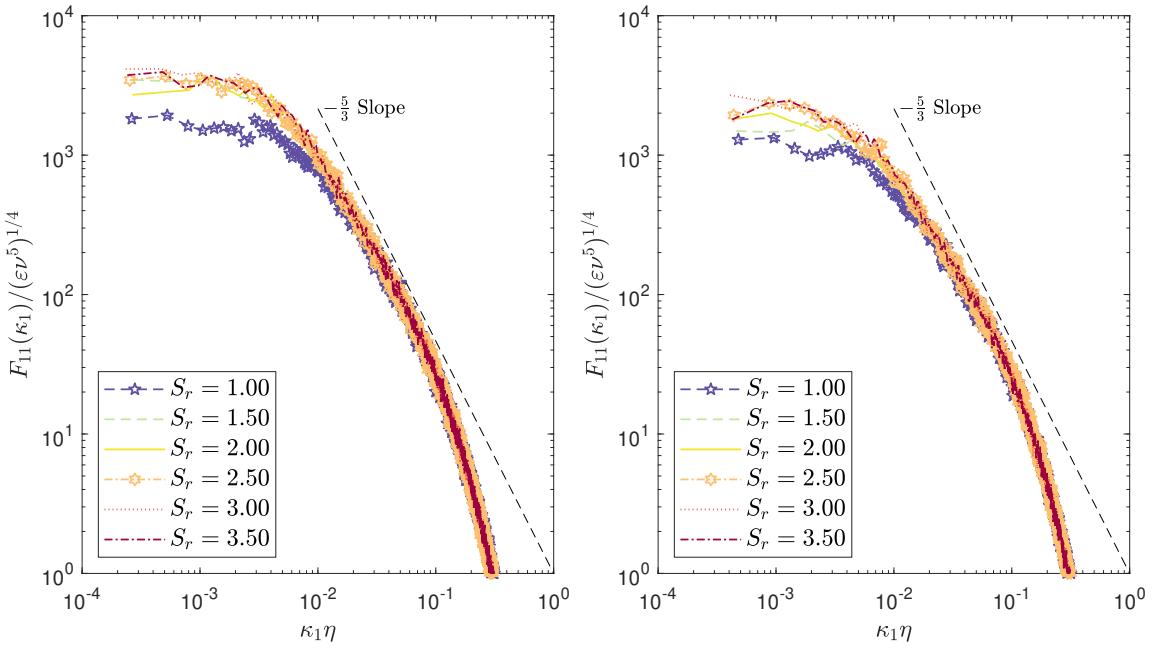

(a) The spectra close from the fan wall.

(b) The spectra far from the fan wall.

Figure 4.20: Spectra for $S_r = 1.00, 2.00$ and 3.00 at locations $x/M = 10$ and $x/M = 21.25$.

4.7 Centreline Turbulent Kinetic Energy Budget Term Estimation

The turbulent kinetic energy budget for decaying grid turbulence, can be simplified to,

$$A = -\varepsilon \ ,$$

as discussed in Chapter 2. However, it is important to stress that this balance is only expected to hold in the equilibrium region of decaying grid turbulence, far from the grid. In the near-field of grid turbulence, where a non-equilibrium scaling has been observed, it was shown that both production and the advective turbulent transport terms are non-negligible (Valente and Vassilicos, 2011, 2014).

The viscous diffusion term in the turbulent kinetic energy budget, Equation (2.24), is assumed to be zero since the Reynolds number is large, indicating a small impact from the viscosity of the air. We further assume the flow to be steady, hence the local derivative is also assumed to be zero. The pressure transport term is not considered in this analysis

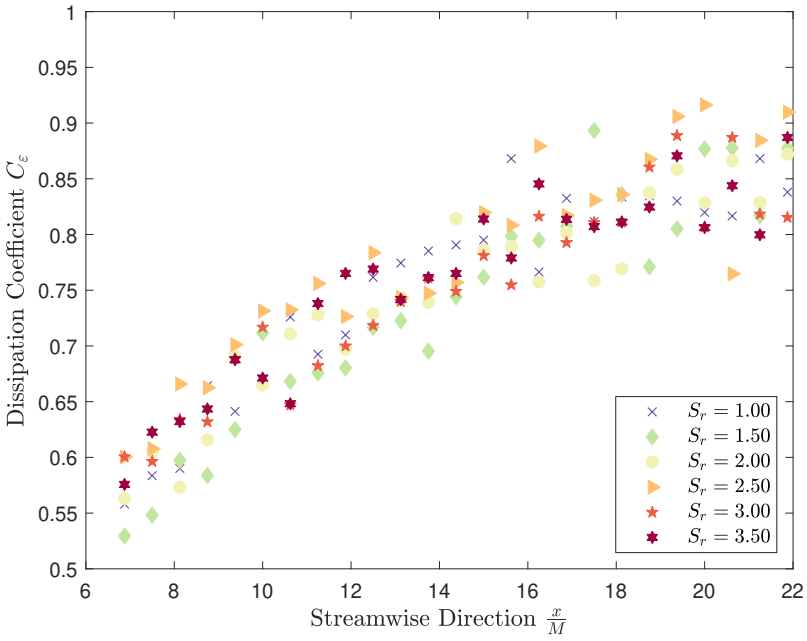

Figure 4.21: Development of the dissipation coefficient.

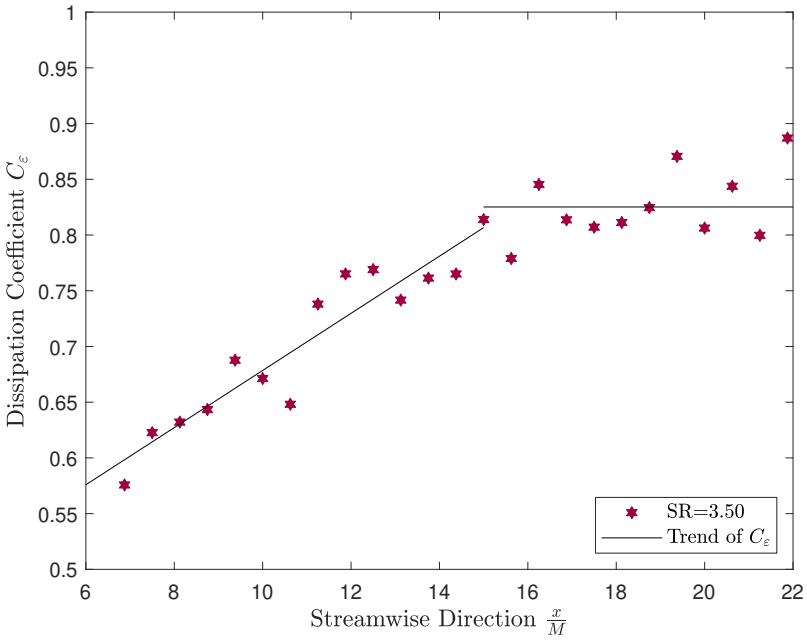

Figure 4.22: Profile of dissipation coefficient development.

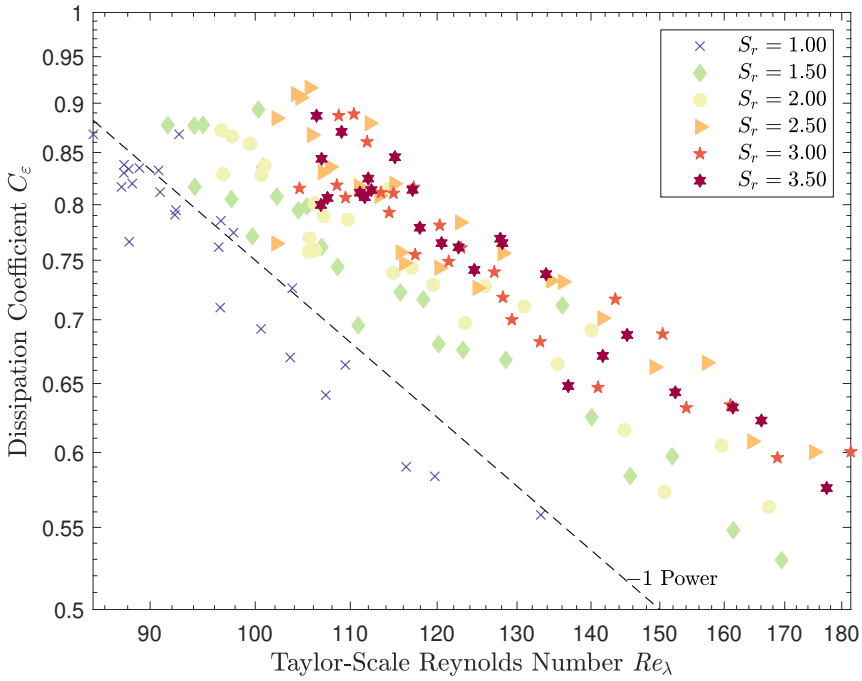

Figure 4.23: Comparison of Reynolds number to the dissipation coefficient.

given that no pressure measurements were taken with the hot-wire measurements. Hence the turbulent kinetic energy budget is

$$A = T + P - \varepsilon \,, \tag{4.3}$$

where the terms are estimated from the data as follows. The advection A is calculated as,

$$A = \overline{u}\frac{\partial k}{\partial x} \,,$$

because there is only a component of mean velocity in the x direction. The advective turbulent transport, T, was calculated as,

$$T = -\frac{\partial}{\partial x}\left(\frac{\overline{u'(u'^2 + 2v'^2)}}{2}\right) \,, \tag{4.4}$$

since measurements are taken at the centerline. Finally, the production term P is estimated

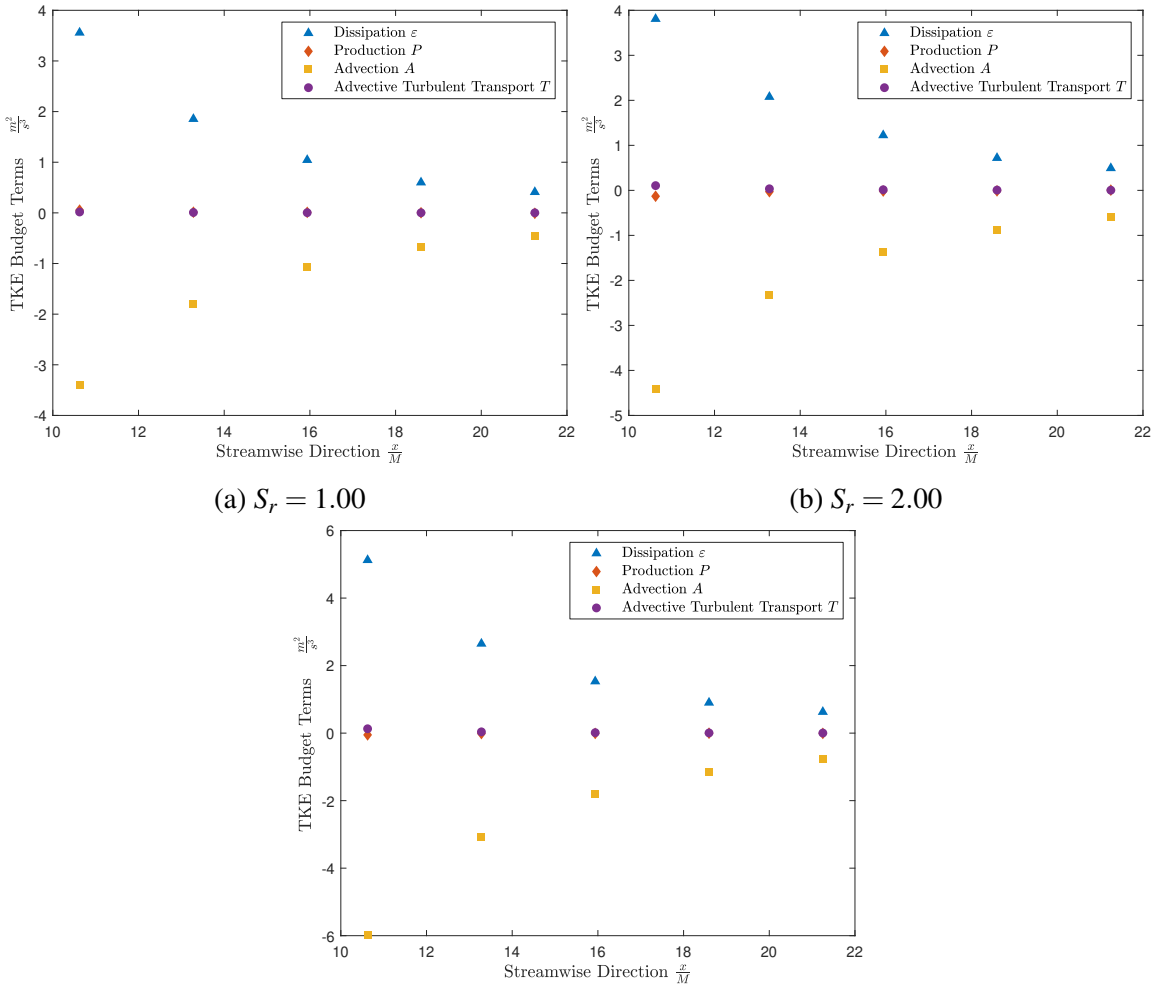

(a) $S_r = 1.00$

(b) $S_r = 2.00$

(c) $S_r = 3.00$

Figure 4.24: TKE budget terms for $S_r = 1.00, 2.00$ and 3.00.

as,

$$P = -\overline{u'^2}\frac{\partial \overline{u}}{\partial x} - \overline{u'v'}\frac{\partial \overline{u}}{\partial y}\,, \tag{4.5}$$

where the first term is due to the mean velocity gradient in the x direction. Note that close to the fan wall, the streamwise profile of the mean flow is increasing for $S_r > 1.00$ and decreasing for the case of $S_r = 1.00$ only; hence we can expect a possible change in sign for this term between the $S_r = 1$ case and the other cases. Lastly the dissipation, ε is calculated using a X-wire approximation, Equation (4.2).

The advection term, the advective turbulent transport term and the first element of the production term were estimated using the x direction derivative of the streamwise development of the TKE, k and mean velocity $\overline{u}$. The planar data was used to estimate the y derivative for the second component of the production term. Lastly, ε was calculated using the spatial derivatives of u and v. Since planar measurements were only taken at five streamwise locations, the turbulent kinetic energy terms can only be estimated at those locations, and are shown in Figure 4.24. Both the transport and production terms are an order of magnitude smaller than the advection and dissipation terms. The small production term indicates that the contribution of shear is negligible to the overall behavior of the observed turbulence, confirming the shear analysis conducted previously. Therefore, the two dominant terms in the balance are the dissipation rate and the advection term.

In order to determine if the pressure transport term, the one term that we were unable to measure, has any significant contribution to the budget, we compute the residual, namely $\Delta = A - T - P + \varepsilon$. If $\Delta \approx 0$, then all the terms in the budget are accounted for. As shown in Figure 4.25, the non-dimensional residuals for all shear ratios converge to a value of approximately -0.2 as we move further downstream from the fans. Increasing the shear ratio increases the magnitude of the residual for all downstream locations. Although the magnitude of the residuals may appear small, they are, at the closest position, roughly 5-14% of the advection term, the larger value corresponding to the $S_r = 3.00$ case. Therefore, there is a possibility that the pressure transport term may indeed have an influence on the turbulence. It may also be possible, however, that the uncertainties in estimating these variables, in particular the errors of $\sim 2-3\%$ in the turbulence intensity, may also contribute to the residual seen here; it is evident that these aspects would have to be investigated in a future study to verify. Regardless, it is evident that the advection and dissipation terms are the dominant ones, which is similar to what one observes in decaying grid turbulence.

4.8 Comparison to Previous Studies

Having the ability to operate with an envelope of turbulence intensities and integral scales to produce turbulent flows would be useful for UAV testing, one of the motivations of the present study. In Figure 4.26, the boundaries of the combinations of turbulent inten-

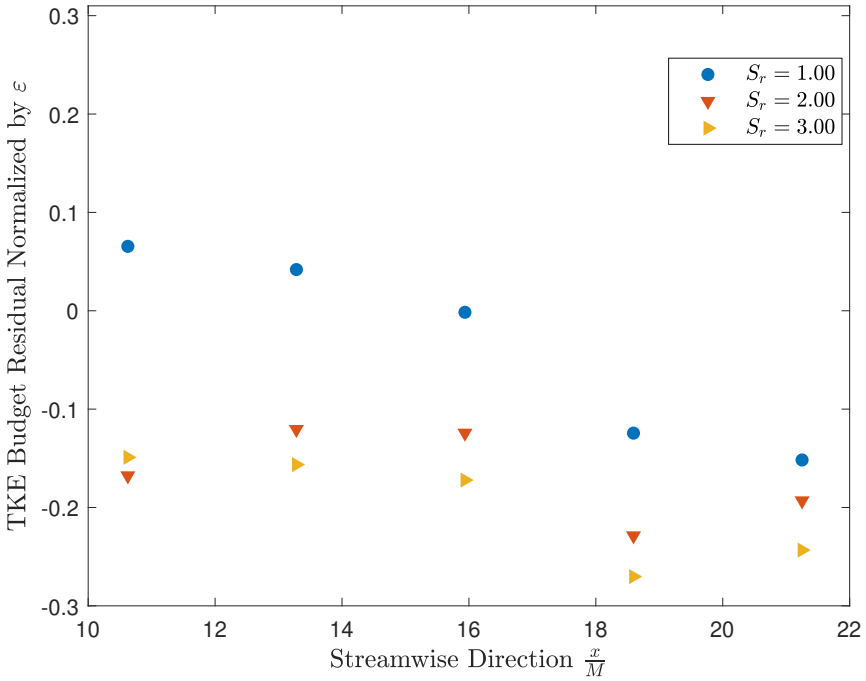

Figure 4.25: Non-dimensional residual of the TKE budget, $\frac{T-A-P+\varepsilon}{\varepsilon}$.

sities and integral length scales are presented, indicating that a wide range of turbulence intensities and turbulent scales can be realized through interpolation between shear ratios at various locations within the tunnel.

In Figure 4.27, a comparison is made between the data shown in Figure 4.26 to previous studies on turbulence generated by active grids (Mydlarski and Warhaft, 1996) and in MFWT used by Ozono and Ikeda (2018). It is clear that the McGill MFWT is capable of achieving high turbulence intensity but low integral length scales as compared to those found in the literature. The reason for the lower normalized scale is due to the static nature of McGill's facility compared to the dynamic nature of the tunnels used to produce the flows with larger integral scales. The *quasi-grid mode* (QG mode) presented by Ozono and Ikeda (2018) is another example of a static fan configuration. The realized integral scale of the *quasi-grid mode* mode is of the same order as the scales achieved in this study. The fans used in the *quasi-grid mode* are larger and more numerous than the fans used in the McGill tunnel, which would explain the difference between the two results, since larger wind tunnel geometries generate larger integral scales, even when the scales are normalized.

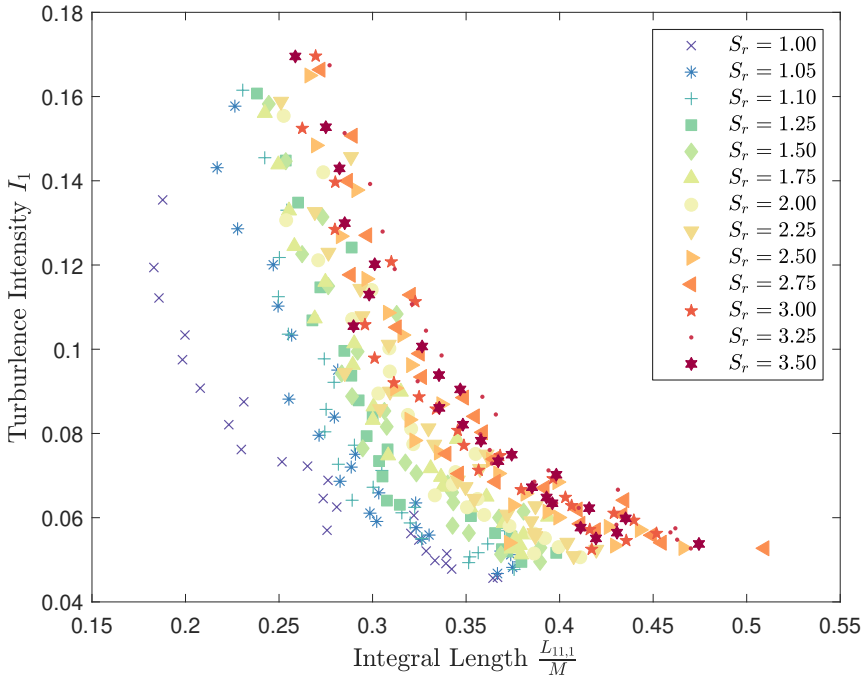

Figure 4.26: The integral scale and turbulence intensity number design envelope.

4.9 Suggested Turbulence Intensity Scaling

For the purpose of creating a tailored flow for UAV testing it would be desirable to estimate which shear ratio is needed to produce a given turbulence intensity for a given streamwise location. A turbulence intensity scaling is proposed which would achieve this goal. The turbulence intensity at a given shear ratio is normalized by the turbulence intensity for $S_r = 1.00$. The downstream development of the turbulence intensity for a shear ratio of unity must be known for the proposed scaling to work. The equation,

$$\frac{I}{I_{1,S_r=1.00}} = \frac{a}{a-1+S_r^b}\,, \tag{4.6}$$

has unique coefficients a and b for each downstream location as shown in Figure 4.28. Each curve represents one downstream location's growth of normalized turbulence intensity with increasing shear ratio. The growth of these coefficients are shown in Figure 4.29 for each downstream location tested. A least squares curve fitting method was used to determine a and b. Both coefficients appear to stabilize to a constant value after $x/M = 13.75$, be-

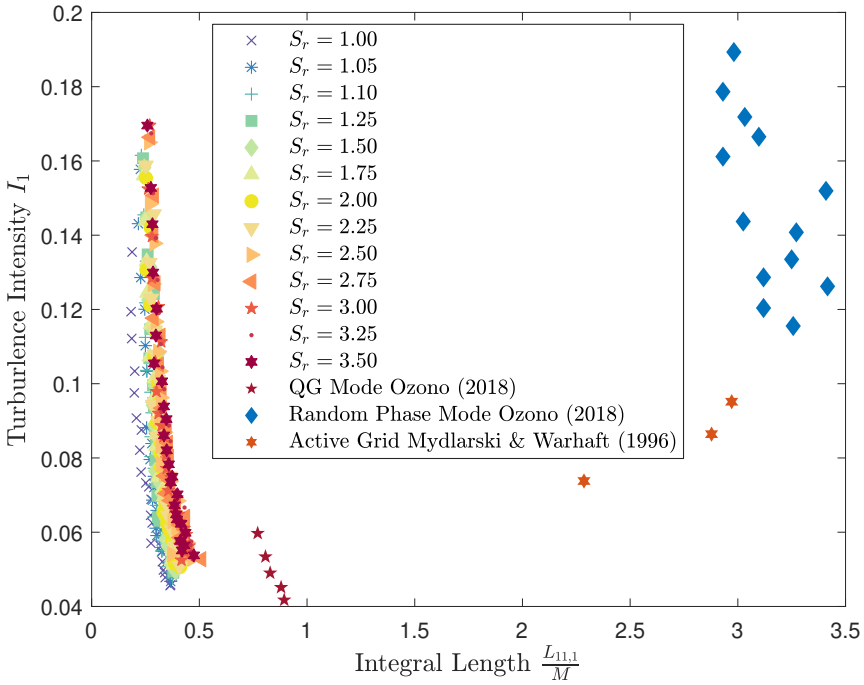

Figure 4.27: Comparison of turbulence intensity and integral scale to other research.

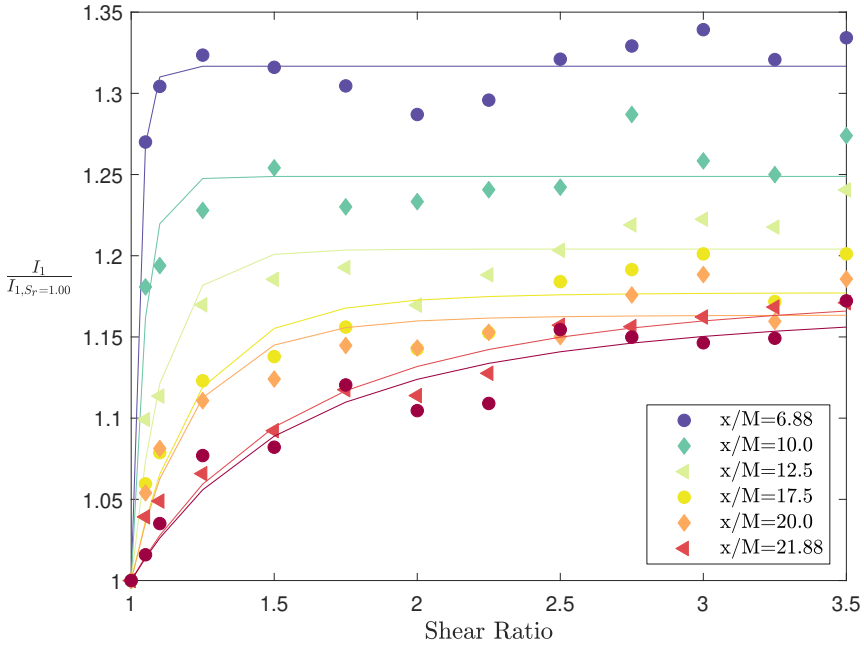

Figure 4.28: Scaling for turbulence intensity normalized by the $S_r = 1.00$ case.

fore this downstream location both coefficients seemingly grow linearly. The downstream location of $x/M = 13.75$ is close to the transition point between the non-equilibrium and equilibrium regions, as shown in the kinetic scaling, Section 4.2, and the dissipation coefficient analysis, Section 4.6.

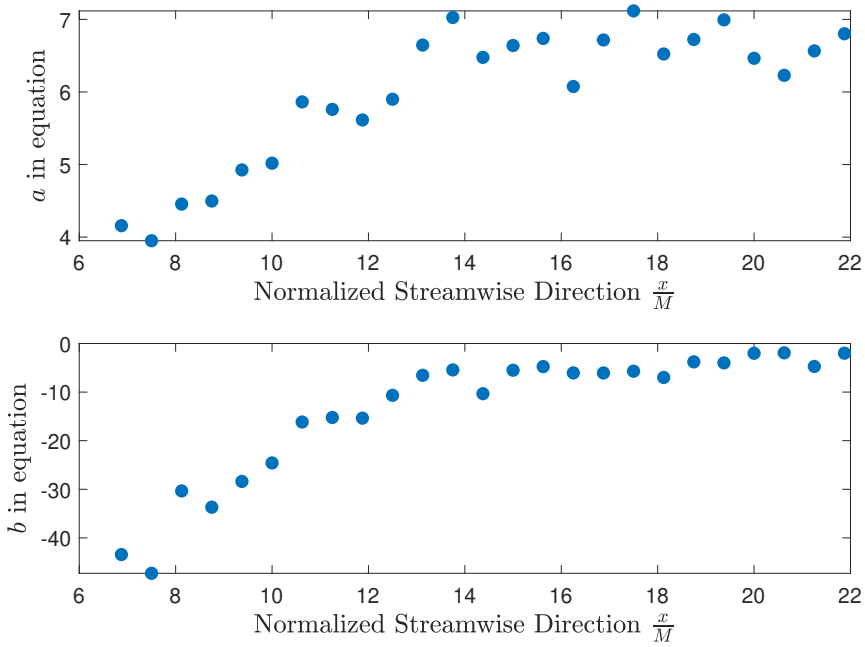

Figure 4.29: Coefficients of $\frac{a}{a-1+S_r^b}$.

The results presented in this section are a characterization of McGill's MFWT facility. The ultimate goal of this facility is to test aircraft and generate flows with known turbulent parameters in the near field of the flow. This study has shown that a change in shear ratio will indeed influence the nature of the turbulence being produced by a MFWT. There is also strong evidence that the flow generated by a MFWT is similar to grid turbulence. At the present time, the turbulent intensities produced by this tunnel are large and the integral length is small, it would be desirable to investigate dynamic modulation of the wind tunnels fans. Research from Ozono and Ikeda (2018), suggests that there are methods of dynamically modulation that will generate large integral scales without pulsatile components of the flow. The present data is meant to be used as baseline in the characterization of the MFWT. With the proper controller, a MFWT can be configured in innumerable ways, the work presented in this chapter represents only a small number of the tests conducted

with the MFWT in search of meaningful results. The next chapter will, very briefly, present other wind tunnel configurations that were tested.

4.10 Grid Spacing Equivalent for MFWT

Finally, to conclude this chapter, we briefly discuss the definition of the length scale that should be used for multi-fan wind tunnels and grid turbulence, in order to facilitate a comparison. In this study a length scale was needed for the normalization of various turbulent parameters, as well as the normalization of spatial movement within the wind tunnel. The chosen parameter was the dimension (diameter) of the fan, namely $M = 80$ mm. In contrast, the normalization used in grid turbulence is the spacing between the bars of the grid, L_0. To make an equivalent comparison between grid turbulence and the turbulence generated inside of a MFWT, it is argued that $L_0 = 2M$ should be the equivalent normalization. Bos (2020) emphasised how the bars of a grid creates a sinusoidal planar mean velocity profile, where the separation between the peaks of the sinusoidal profile is approximately L_0, and that the spatial evolution of such a profile leads to the turbulence scalings that have been observed previously. Looking at Figure 4.2 and Figure 4.3, the separation between the peaks of the mean velocity profile for $x = 850\,\text{mm}$ is indeed $2M$. If the scaling were to change, the plots with the normalized streamwise direction on the x axis would have their curves shifted to the left, and the range of measurement would change from $6.875 \leq x/M \leq 21.875$ to $3.4375 \leq x/M \leq 10.9375$. It is important, however, to note that the decay exponent calculated in Section 4.2 would remain the same even if a different length scaling was used. To verify if this is indeed the correct scaling, further measurements would have to be taken in the MFWT where the velocity map was changed so as to mimic the effects of a larger fan, as shall be discussed in the next chapter.

Chapter 5

Future Work

The objective of the present study was to provide a baseline set of measurements to be used to further develop the capabilities of McGill's multi-fan wind tunnel facility. Building from this baseline, a large array of additional tests could be conducted given the flexibility, and customizable nature, of multi-fan wind tunnels. A selection of suggested future studies is provided below. In particular, it would of interest to incorporate a dynamic mode that would allow for a large magnitude of additional tests and comparisons to be performed using McGill's facility. In order to conduct dynamic tests, a controller is needed to modulate the input signals to the fans. More static fan configurations, in addition to the chessboard pattern tested in this study, could also be used to help identify the proper length scale to be used with MFWTs.

5.1 Time Varying PWM Intensity

Some preliminary measurements were performed to determine if a sinusoidal function can indeed be sent to the fans. Figure 5.1 shows the resulting mean velocity profile obtained from sending all of the fans the function,

$$\text{PWM} = 0.0575 \sin(2\pi 0.1t + \phi) + 0.5375 \, .$$

For a phase shift of zero, the PWM signal was fluctuated between $48\% \leq \text{PWM} \leq 59.5\%$ at a frequency of $f = 0.1$ Hz. The mean velocity was calculated using a sliding window that uses one-tenth of the amount of samples taken in 1 s, in this case the sliding window used 7500 data points. The resulting velocity amplitude was measured as 1.9 m/s, with a mean velocity of 5 m/s. The estimated velocity profile, determined using the inverse of Equation (3.1), is also shown in Figure 5.1. Evidently, the measured velocity has a higher amplitude than the estimated one, indicating that the dynamic modulation of the fans produces higher velocities than the static case. The linear correlation between the estimated velocity profile and measured velocity is 94.2%.

This small tests proves that the McGill MFWT is capable of producing dynamic velocity signals. More work must be conducted to determine the fastest period the fan wall can replicate i.e., the frequency response of the facility, as well as the turbulence field generated downstream.

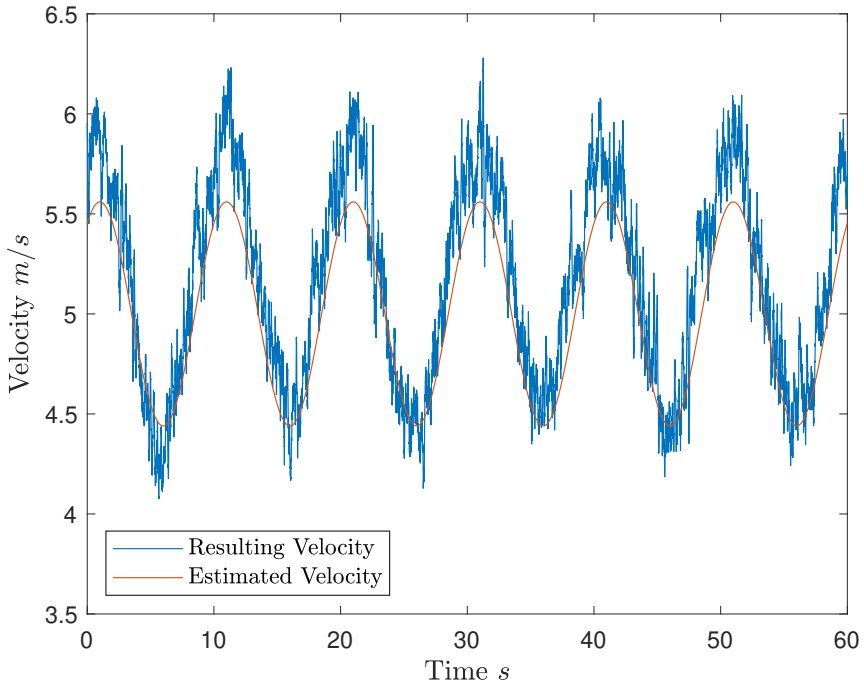

Figure 5.1: Mean flow following a 0.1 Hz sine wave oscillating between $48\% \leq \text{PWM} \leq 59.5\%$. The data was taken at $(6.88M, 0, 0)$.

5.2 Hardware

It would be useful to develop a device capable of generating a unique time varying PWM signal for each fan on the fan wall. This would allow for a comparison between McGill's facility and the facility at the University of Miyazaki. A great deal of time was spent at the beginning of this project attempting to use Arduino's to control the fan wall, however, the micro controllers simply did not have the capabilities to send the required signals to the fan wall - the main limitation being the need for a 25 kHz carrier wave for the PWM. The suggestion of the author is that a custom controller should be purpose built for the wind tunnel, and the controller should be able to produce 81 time varying PWM signals, one signal per fan. Software could also be created to store a repository of fan configurations to be used to create well defined flows for UAV testing.

In addition, it would also be of interest to discover the source of the slight vertical shear that is currently observed in the facility, as well as investigate if there are any pressure gradients present that might account for the imbalance in the turbulent kinetic energy budget.

5.3 Additional Static Fan Configurations

One last suggestion for future work would be to test what effect fan groupings would have on the streamwise development of the turbulent parameters. In the present study, the fans were arranged in a checkerboard pattern shown in Figure 3.11. The suggestion is to wire the fan wall to create another checkerboard pattern with groupings of four fans shown in Figure 5.2, which would effectively increase the fan spacing, and hence allow one to determine the correct normalising length parameter.

There are, of course, a plethora of other possible fan wiring configurations that one can consider, such as intentionally creating uniformly sheared flows, wakes without the solid object, co-flow jets, and atmospheric-type boundary layers, to name a few. It is necessary to have a specific goal in mind before selecting which configurations to test.

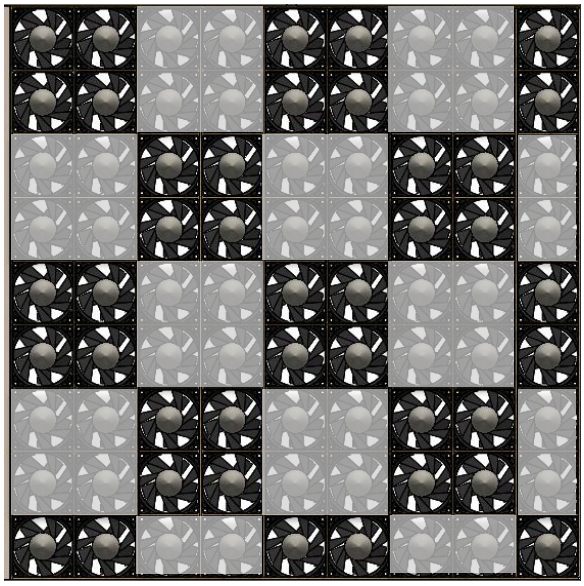

Figure 5.2: Suggested wiring pattern of fan wall. Dark fans receive signal one, light fans receive signal two.

Chapter 6

Conclusion

Multi-fan wind tunnels allow for greater flow customization compared to traditional wind tunnels which use a single large fan. This customization means that MFWTs have the potential to become widespread for use in a wide range of engineering applications, for example the testing of UAVs in unsteady wind conditions. Before this can happen, the resulting flow from specific fan wall configurations must be studied, hence performing a baseline study into one of these configurations was the primary motivation of this thesis. Based on previous studies in the literature, it was apparent that the nature of the turbulence near the fans, where one might expect the highest levels of turbulence intensity, was not explored. In particular, it was decided to focus on a static arrangement of fan velocities which would introduce a velocity shear in the flow, where the shear ratio S_r is defined as the ratio between the highest and lowest velocities. To address this gap, hot-wire anemometry was used to measure the u and v components of velocity at various locations downstream of the fan wall, closer than what has previously been investigated in literature.

The fan wall was arranged in a checkerboard pattern, a constant bulk velocity of $U_\infty = 5\,\mathrm{m\,s^{-1}}$ was maintained for the 13 shear ratios, ranging from $1 \leq S_r \leq 3.5$. The evolution of turbulent parameters was measured using velocity time series obtained by moving a hot-wire both downstream of the fan wall, as well as in the planar direction. The planar data was obtained by moving the probe in the horizontal z direction and vertical y direction. The uniformity of the flow was obtained from these planar measurements, for all shear ratios tested, was found to occur at 13.28 fan diameters away from the fan wall. The

homogeneity of the flow occurs slightly earlier at approximately 10.6 fan diameters from the fan wall, the planar measurement of the root mean square of the velocity was used as an indicator of homogeneity. Lastly, the isotropy, $\frac{u_{rms}}{v_{rms}}$, was found to lie between 0.95 and 1.10 for all measurements.

The results indicate that the multi-fan wind tunnel is capable of generating turbulence similar to that of decaying grid turbulence, without any structures blocking the flow field. This is confirmed by the streamwise evolution of the turbulence parameters, most notably in the decay of the turbulent kinetic energy, whose scaling yielded similar values as would be seen in decaying grid turbulence: $n = 2.13$ in the non-equilibrium range (near field) and $n = 1.349$ in the equilibrium range (far field).

Energy spectra were obtained from positions in the near and far field. An inertial sub-range is visible in the spectra data, the width of which was approximately one decade for all of the cases measured with $S_r > 1$. The case of $S_r = 1$ has less energy content in the spectra and a narrower inertial sub-range. The maximum Taylor-scale Reynolds number obtained was $Re_\lambda \approx 180$; comparable to what would be obtained by passive grids.

The dissipation coefficient, $C_\varepsilon = \frac{\varepsilon L_{11,1}}{(2k/3)^{3/2}}$, measured in the near-field, suggests that non-equilibrium turbulence is produced by this type of tunnel, where the dissipation coefficient is non constant while the flow is developing. Furthermore, it was found that the scaling between the Taylor-based Reynolds number and the dissipation coefficient was of the form $C_\varepsilon \sim Re_\lambda^{-1}$, which is similar to decaying grid turbulence, as well as several other types of shear flows (Vassilicos, 2015).

A very clear influence of the shear ratio on turbulence parameters, including the turbulence intensity, turbulent kinetic energy, energy spectra, integral length scale, and Taylor-scale Reynolds number, were observed. In particular, it was shown that all of these parameters increased with an increasing shear ratio. This observation indicates that this increase as a function of shear ratio can be modelled. For the case of turbulence intensity, a scaling is proposed to estimate the percentage increase of the intensity compared to the case of no shear, $S_r = 1.00$. The scaling indicates an asymptotic increase of the intensity with increasing S_r; for example, it was shown that the turbulence intensity can increase by 25.09% while only changing the shear ratio from $S_r = 1.00$ to $S_r = 3.50$ at the closest measured point to the fan wall. The increase was 14.75% at the farthest point from the fan wall for

the same increase in S_r. Similarly to the case of turbulence intensity, the integral length scale $L_{11,1}$ was found to increase by 25.3% in the near field and 15.3% in the far field for an increase of shear ratio from $S_r = 1.00$ to $S_r = 3.50$.

Motivated by creating a facility to test UAVs, this study aimed to generate bespoke turbulent flows inside of an nontraditional type of wind tunnel. The ability to easily control turbulent parameters of a flow field would be of interest for engineers who wish to test UAVs in conditions more akin to atmospheric boundary layer (ABL) conditions, where the turbulence intensity and integral length scales are large. This study tested and characterized the flows produced by a MFWT facility with the goal of one day being able to mimic the conditions seen in the ABL. This study revealed that a change in the shear ratio parameter will change the resulting turbulent parameters of the flow. For increasing shear ratio, an increase was observed for the turbulence intensity, spectra, Taylor-scale Reynolds number, integral length scale and turbulent kinetic energy. These turbulent parameter are all useful in creating tailored turbulence for UAV testing. The static tests conducted in this study aim to be a baseline for more studies in the future using this multi fan wind tunnel facility.

Appendix A

LABView Software

A.1 Wind Tunnel Control Software

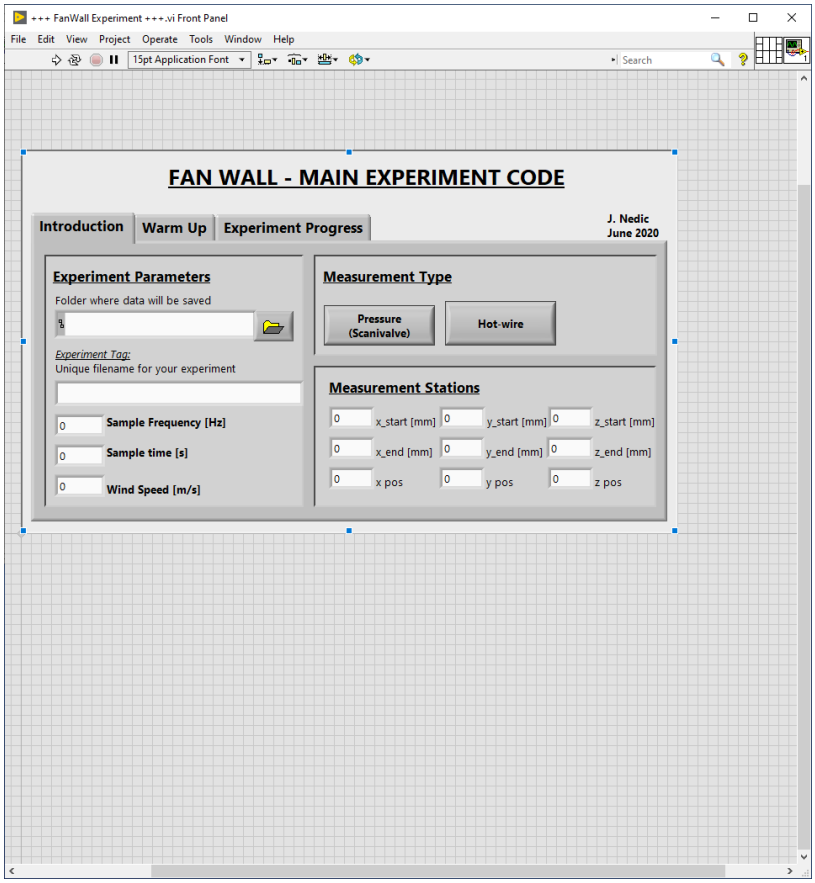

Figure A.1: Front Parnell of LabVIEW code "+++FanWall Experiment+++.vi"

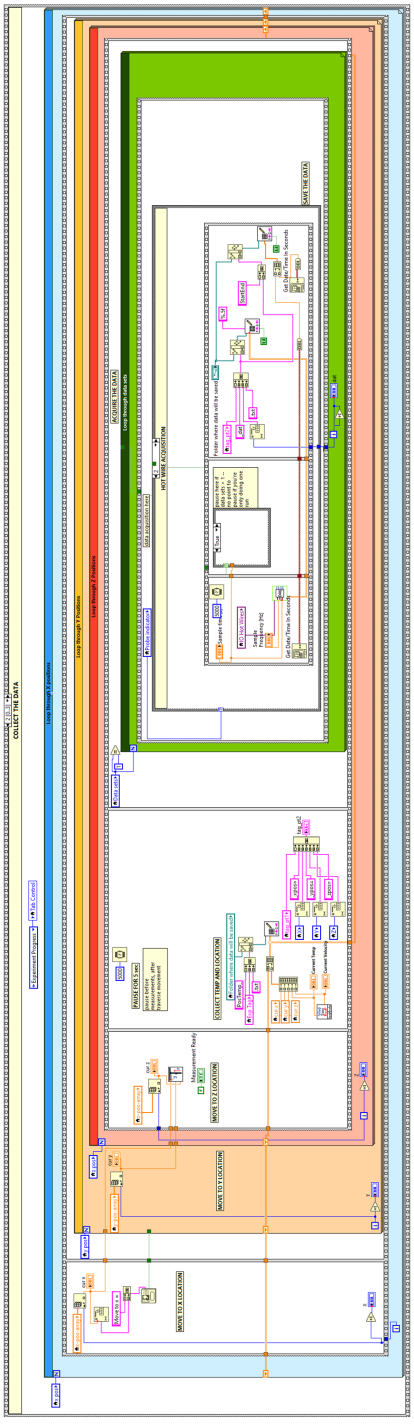

Figure A.2: Block diagram of LabVIEW code “+++FanWall Experiment+++.vi”

Appendix B

Wind Tunnel Test Section Drawings

B.1 Frame Subassembly

Table B.1: Parts required to build three frames, see Frame_SubAssembly_01

Quantity	Item Number	Description	Part Name
6	01	PROFILE 45 X 90 F-2000mm	LongBeam2000MM
9	02	PROFILE 45 X 90 F-2000mm	MediumBeam930MM
6	03	PROFILE 45 x 45 F-750mm	ShortBeam750MM
12	04	Modified two-by-four	MTBF
18	MT21.0978	Wide Angle Bracket	Angle 90
12	MT21.1397	Narrow Angle Bracket	ANGLE 45X90 GD-Z
4	MT21.1349	Small Angle Bracket	ANGLE 45 GD-Z
48	MT21.0818	Hidden Locking Screw	POWER LOCK SF
36	MT21.1210	M8x40 SHCS and nuts	M8x40 SHCS

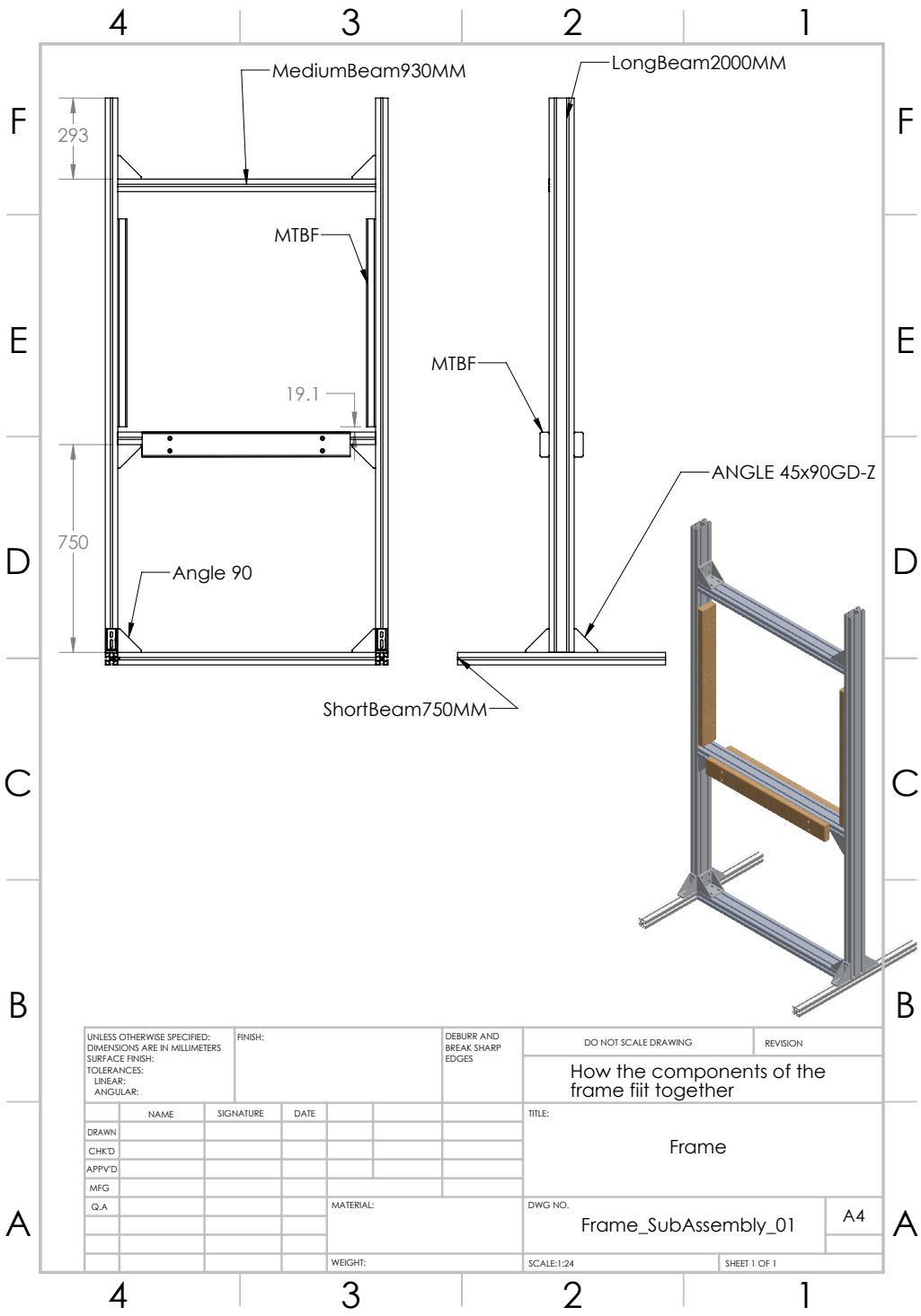

Figure B.1: Frame Subassembly

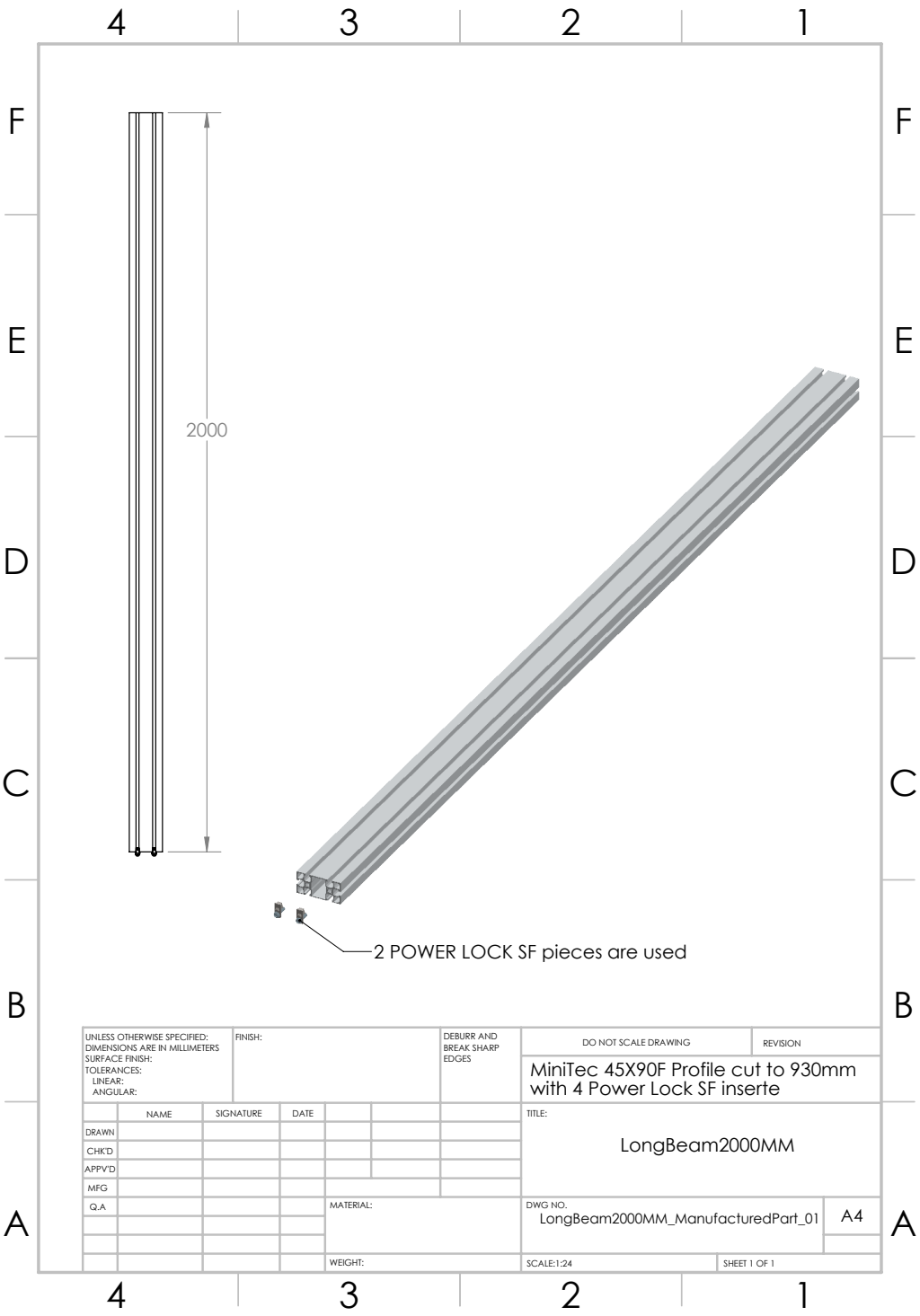

Figure B.2: LongBeam2000MM

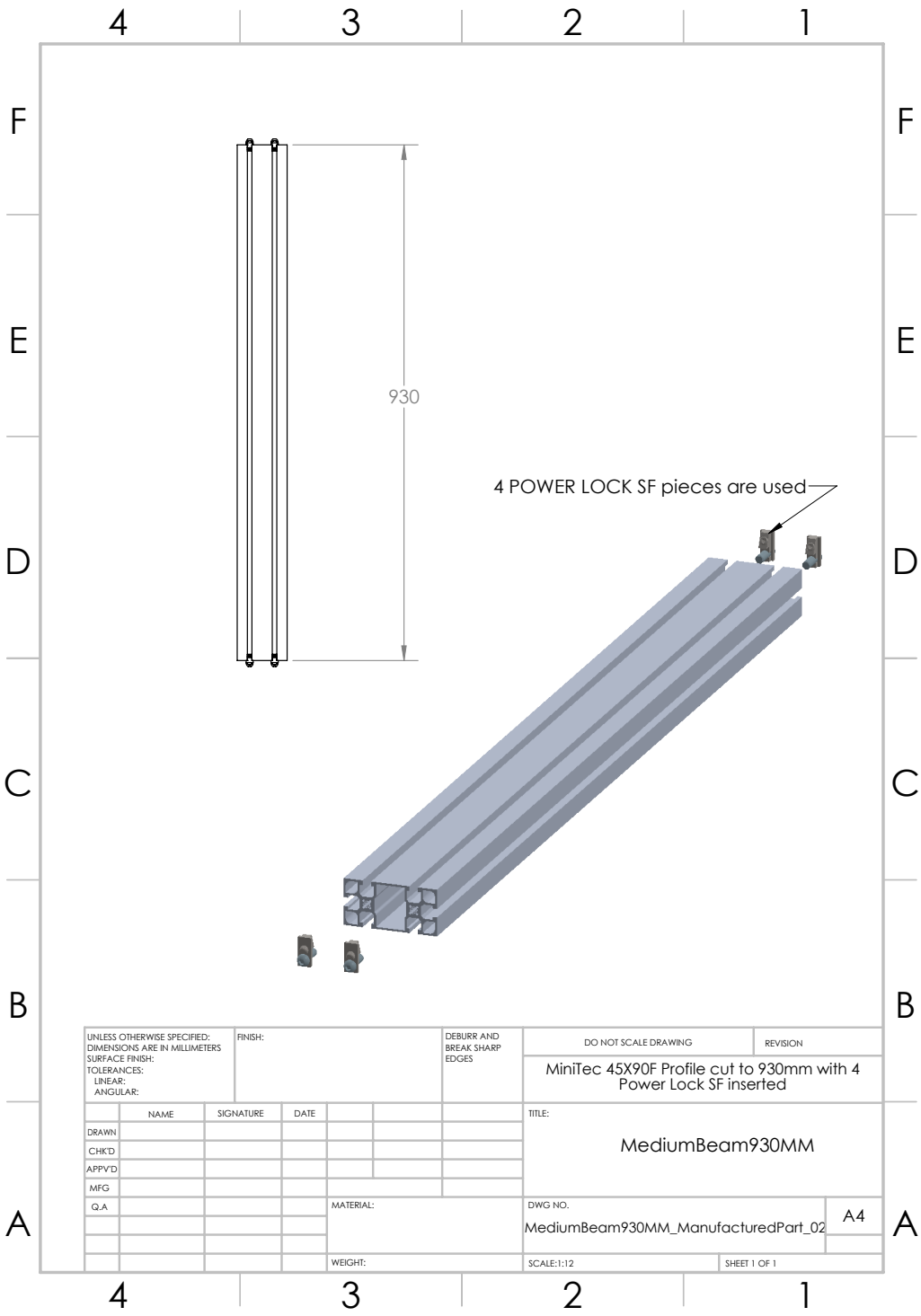

Figure B.3: MediumBeam930MM

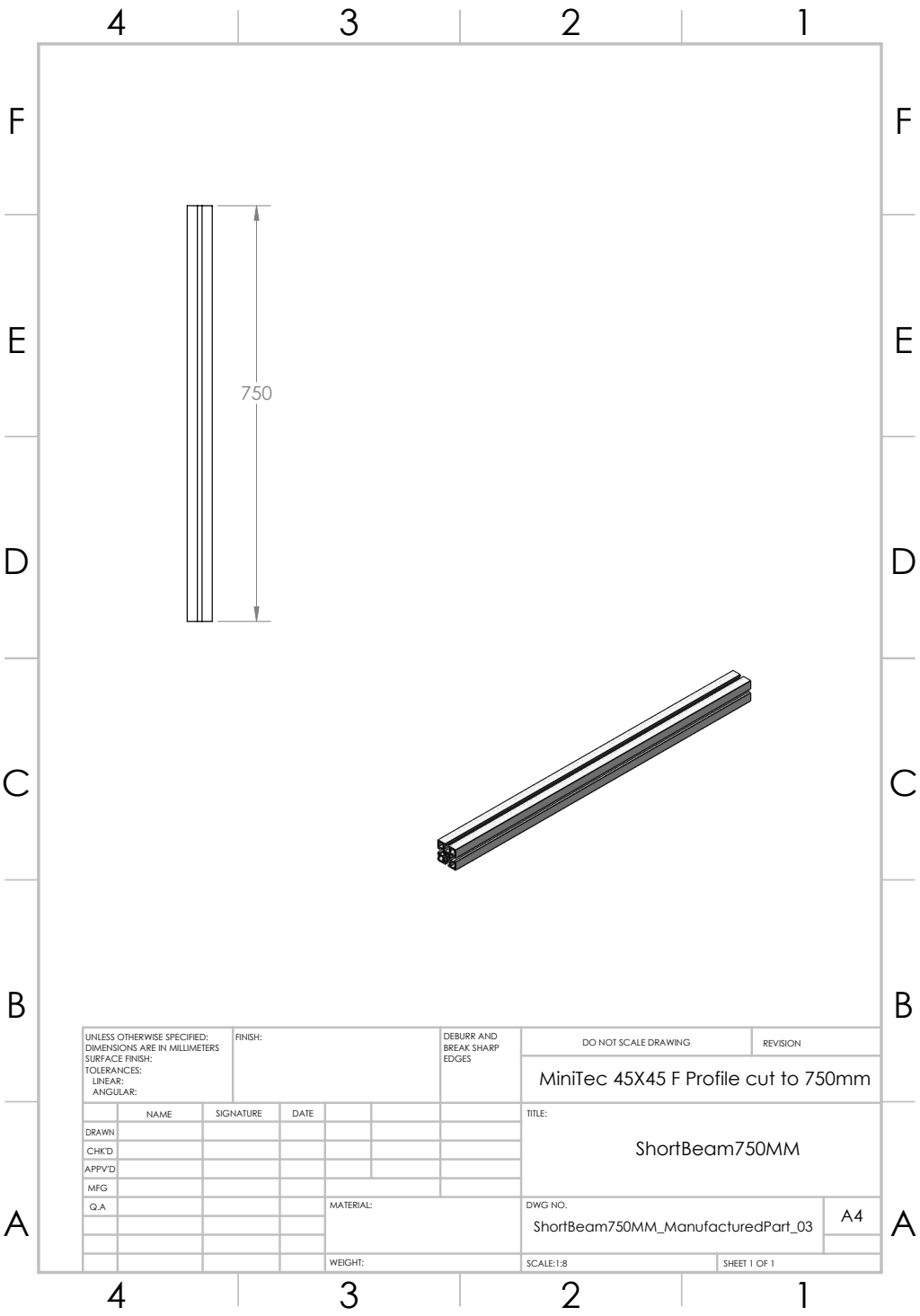

Figure B.4: ShortBeam750MM

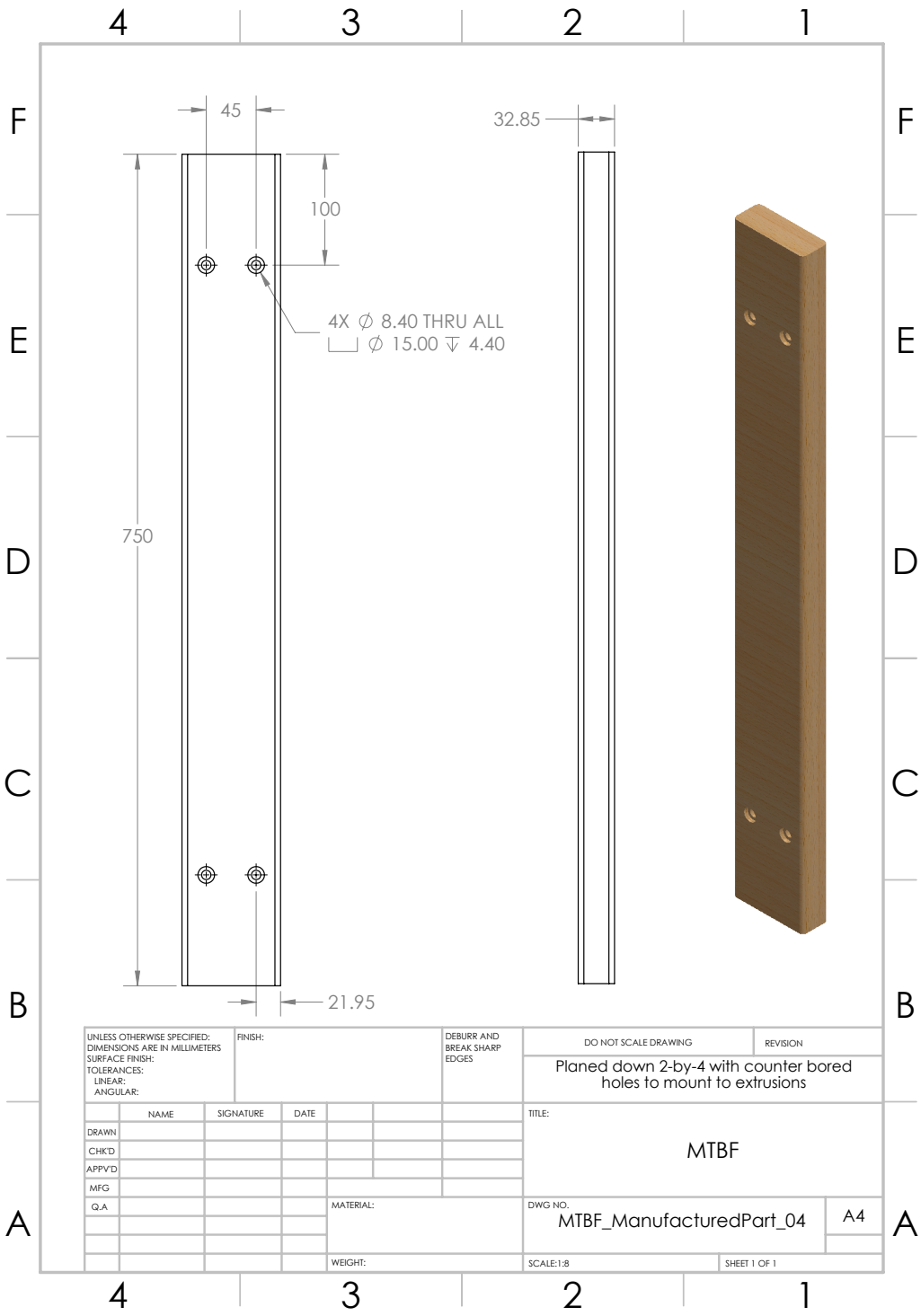

Figure B.5: MTBF

B.2 Box and Window Subassembly

Table B.2: Parts required to build two boxes, see Box_SubAssembly_02 and Window_SubAssembly_03.

Quantity	Item Number	Description	Part Name
8	5	Regular Two-by-Four	RTBF
2	6	Back Wall of Wind Tunnel-no window	Wall*
2	7	Front Wall of Wind Tunnel-with window	Wall
1	8	Floor-no hole	Floor*
1	9	Floor-with hole	Floor
2	10	Ceiling with Slots	Ceiling
8	11	C-Beam Mounting Brackets	CBeamMount
2	OBCustom	C-Beam Linear Rail-2000mm	C_Beam
2	MMC_1131A41	Anodized Aluminum Brush Seals-8ft	BrushSeals
2	12	Window Portion Inside Tunnel	WindowSeal
2	13	Window Portion Outside	WindowOuter
2	14	Window Acrylic	WindowAcrylic
4	MMC13435A63	Adjustable-Grip Draw Latch	Latch
1	MMC93085K42	EPDM Foam Rubber Seal-20ft	Seal
98	SCREW	1 in long wood screw	WS

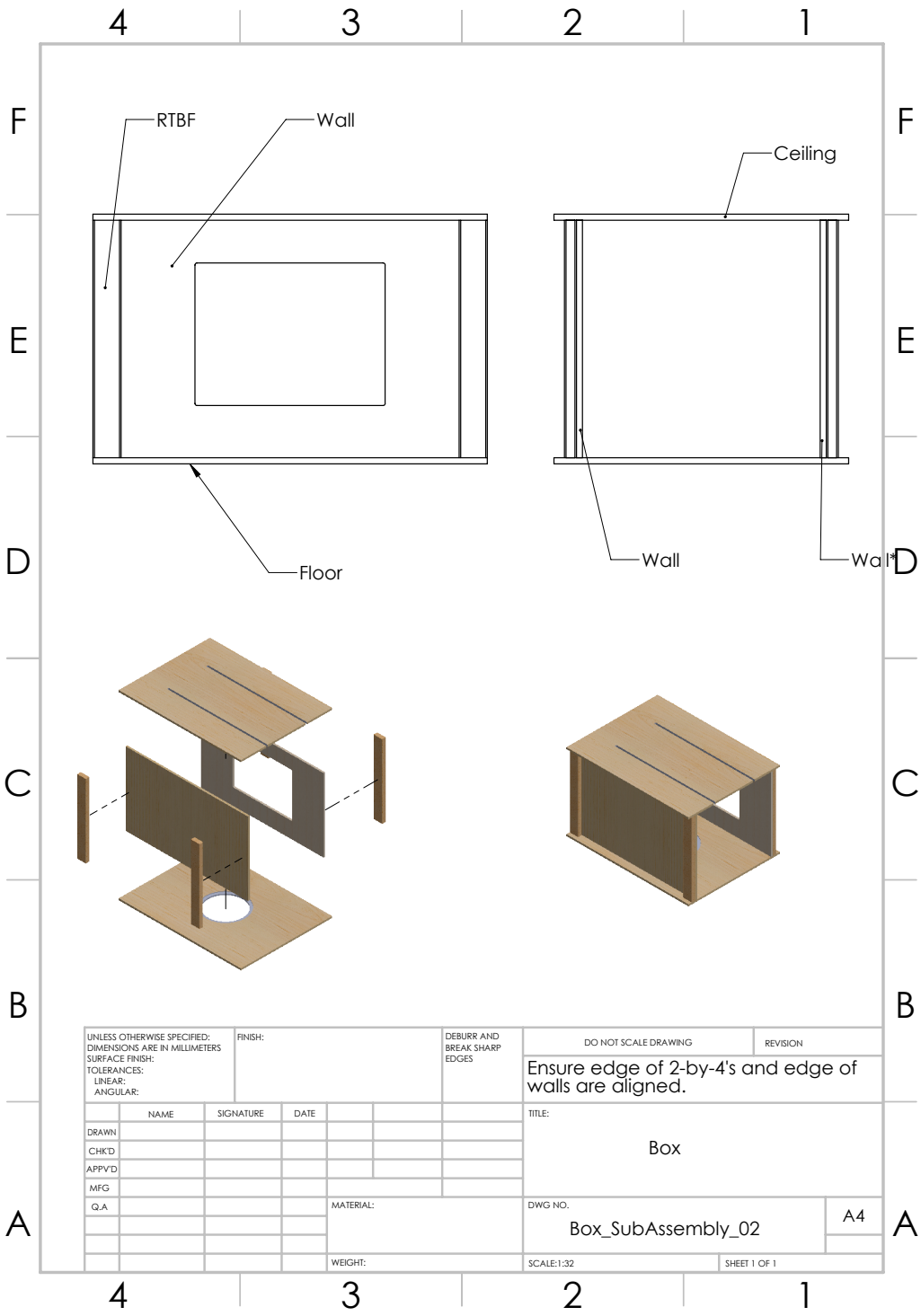

Figure B.6: Frame Sub-Assembly

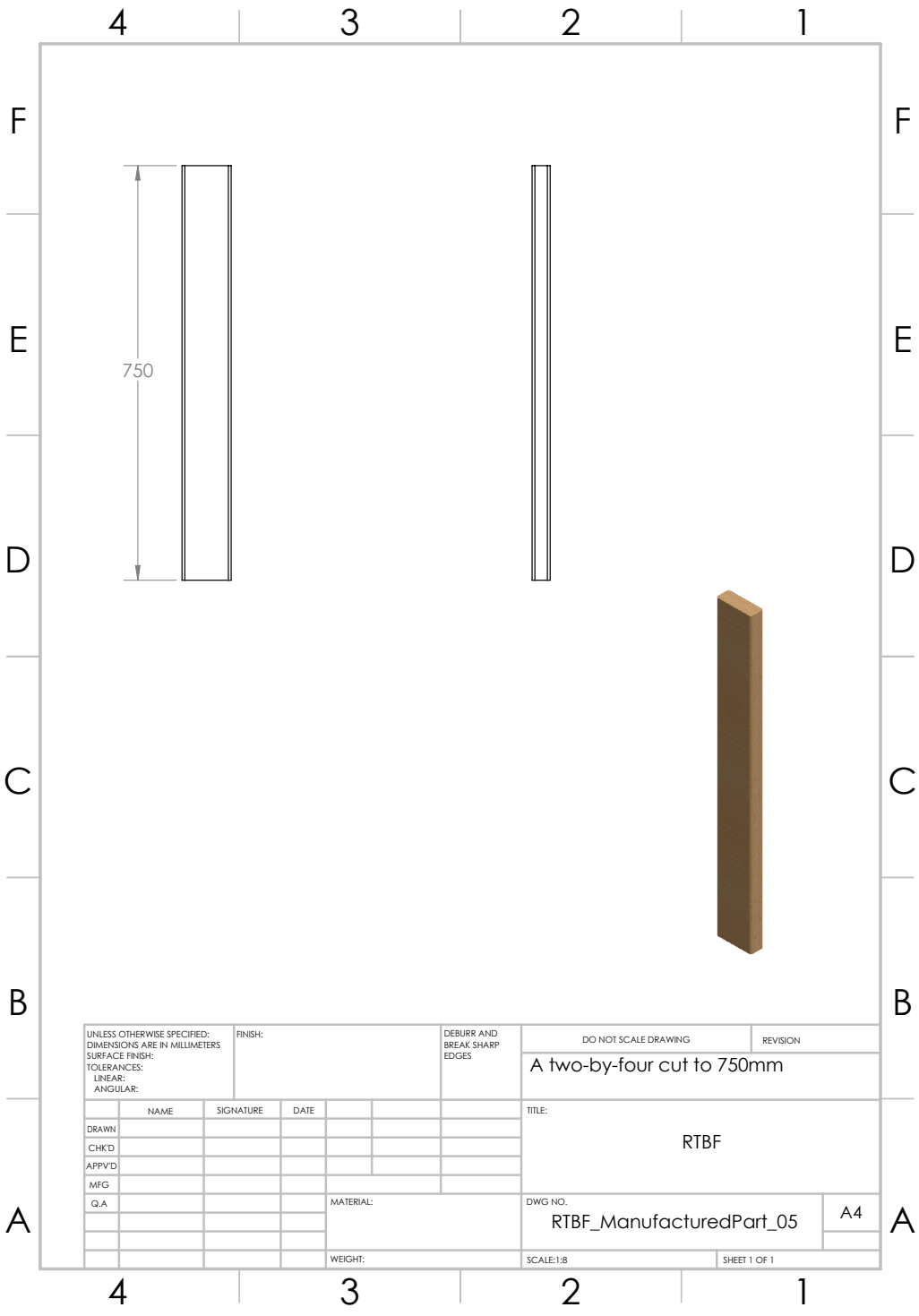

Figure B.7: Regular two-by-four.

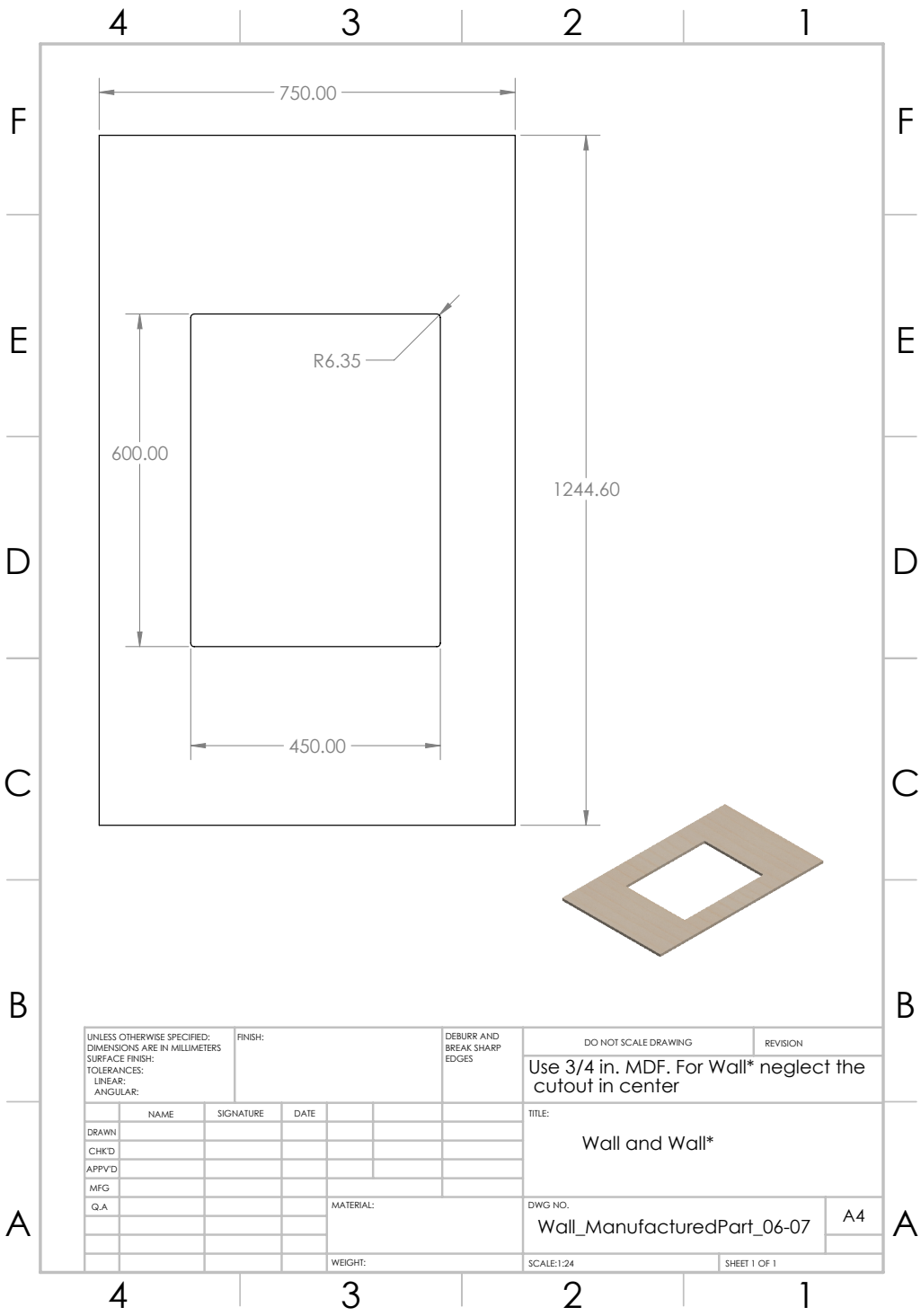

Figure B.8: Wall* and Wall

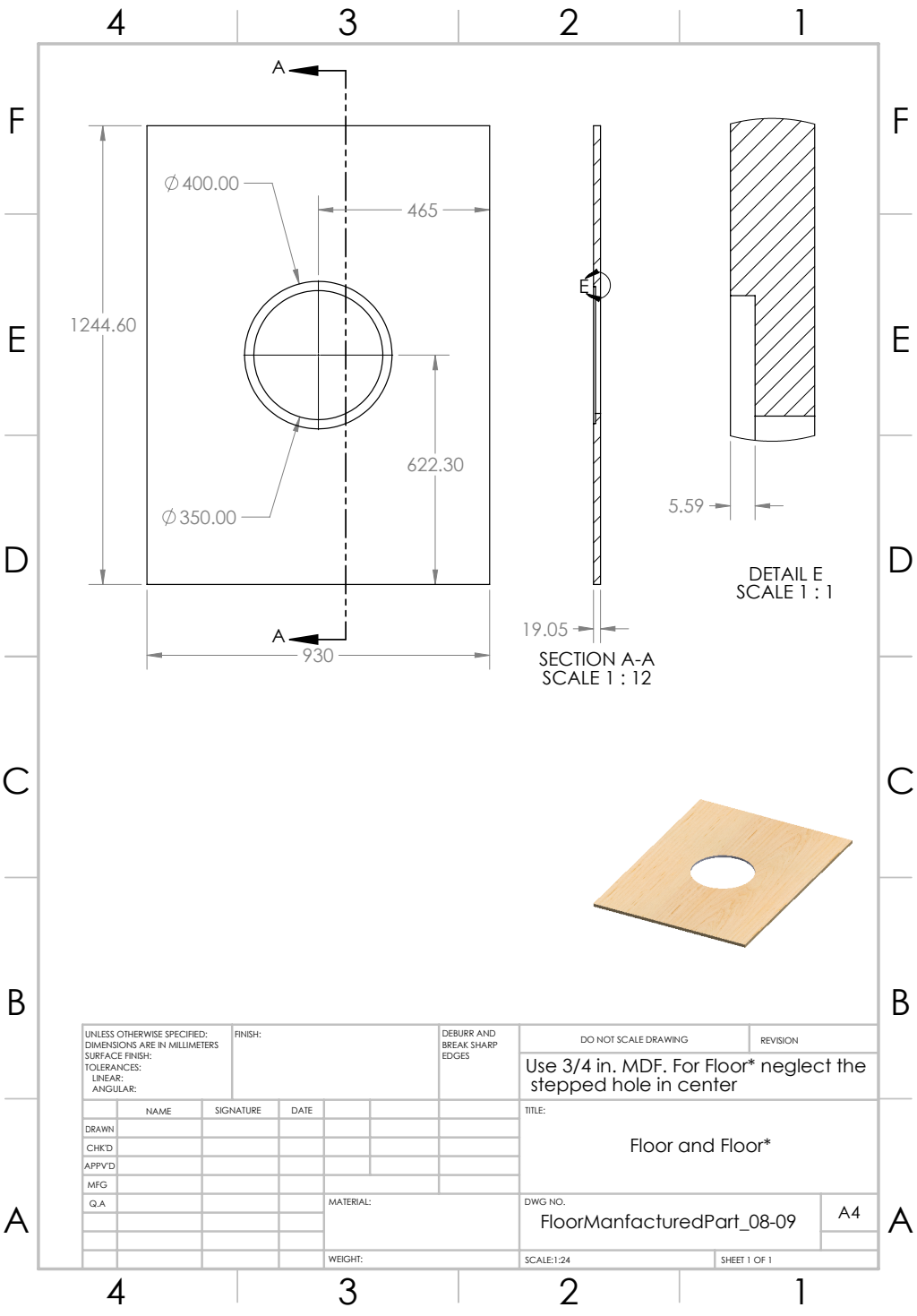

Figure B.9: Floor* and Floor

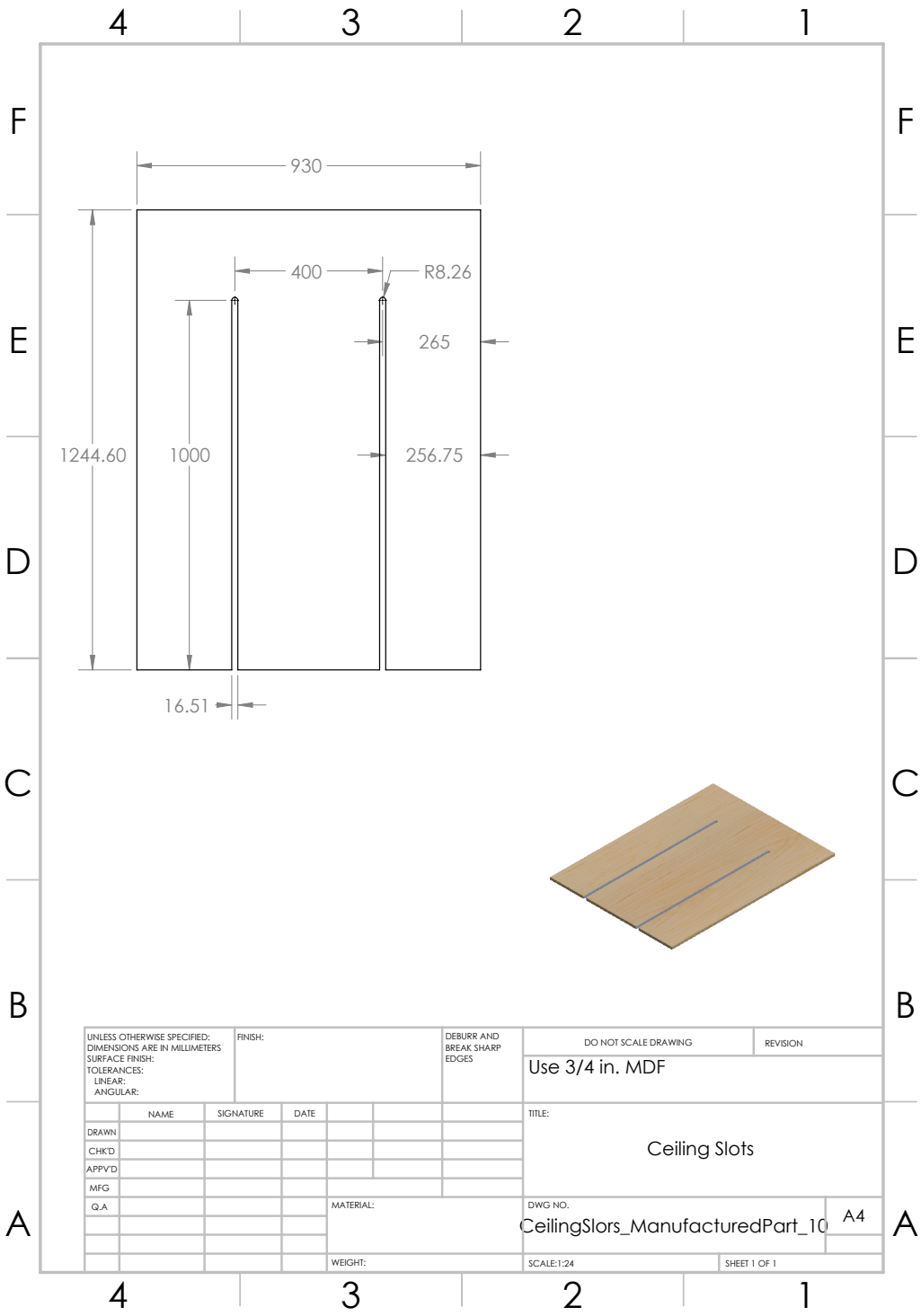

Figure B.10: Ceiling with slots.

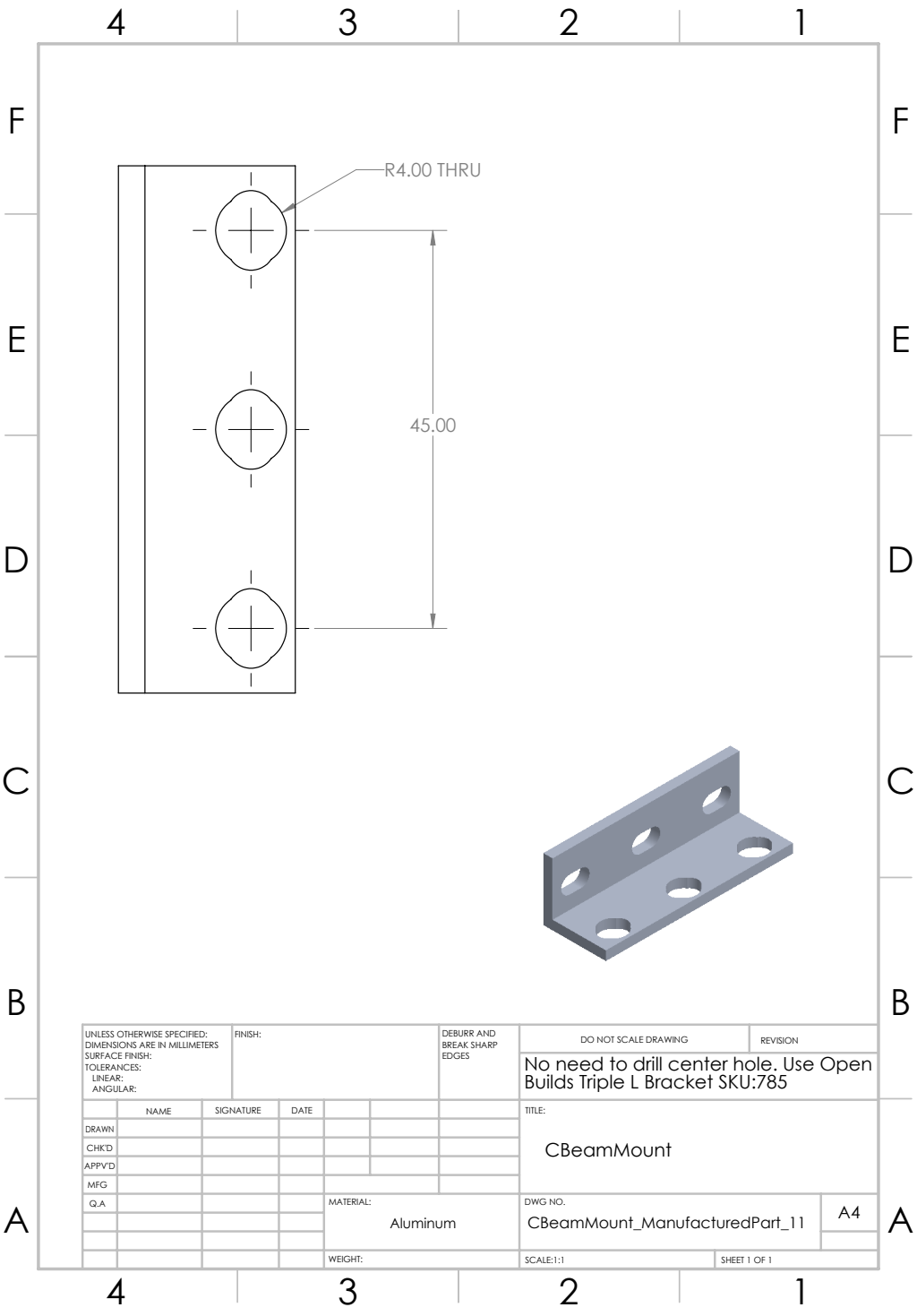

Figure B.11: Traverse C-Beam mounting bracket.

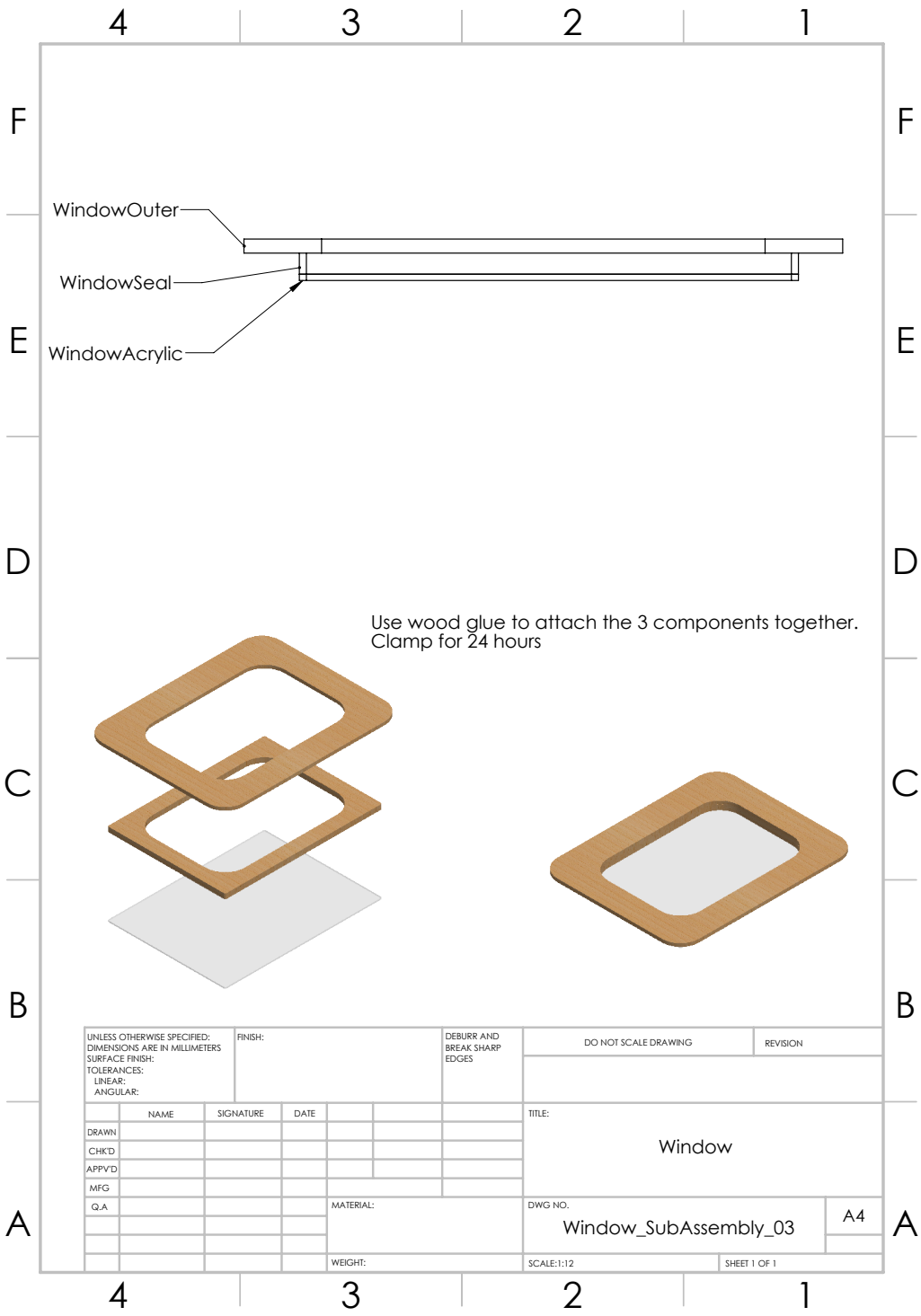

Figure B.12: Window Subassembly

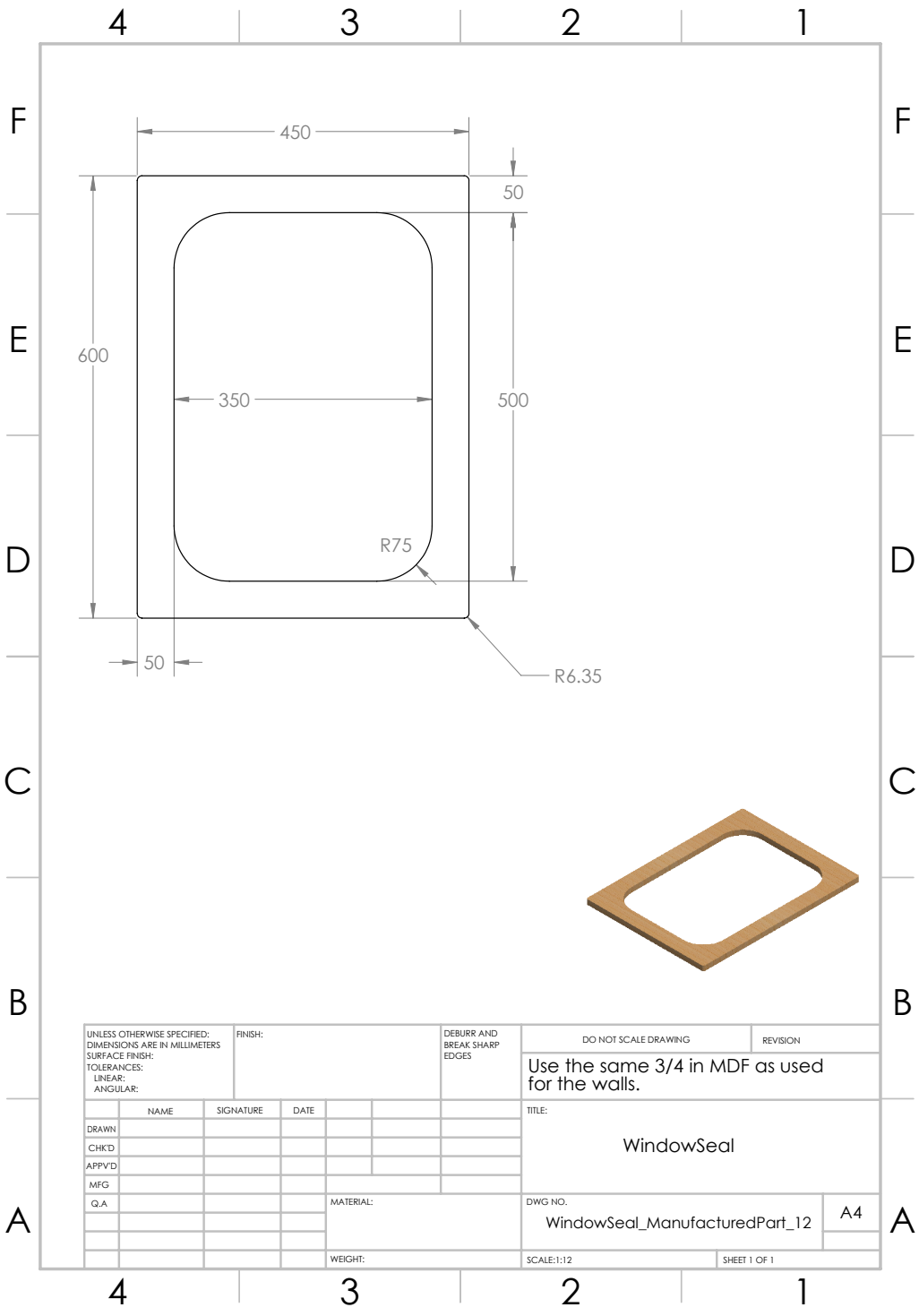

Figure B.13: Window Inner Portion

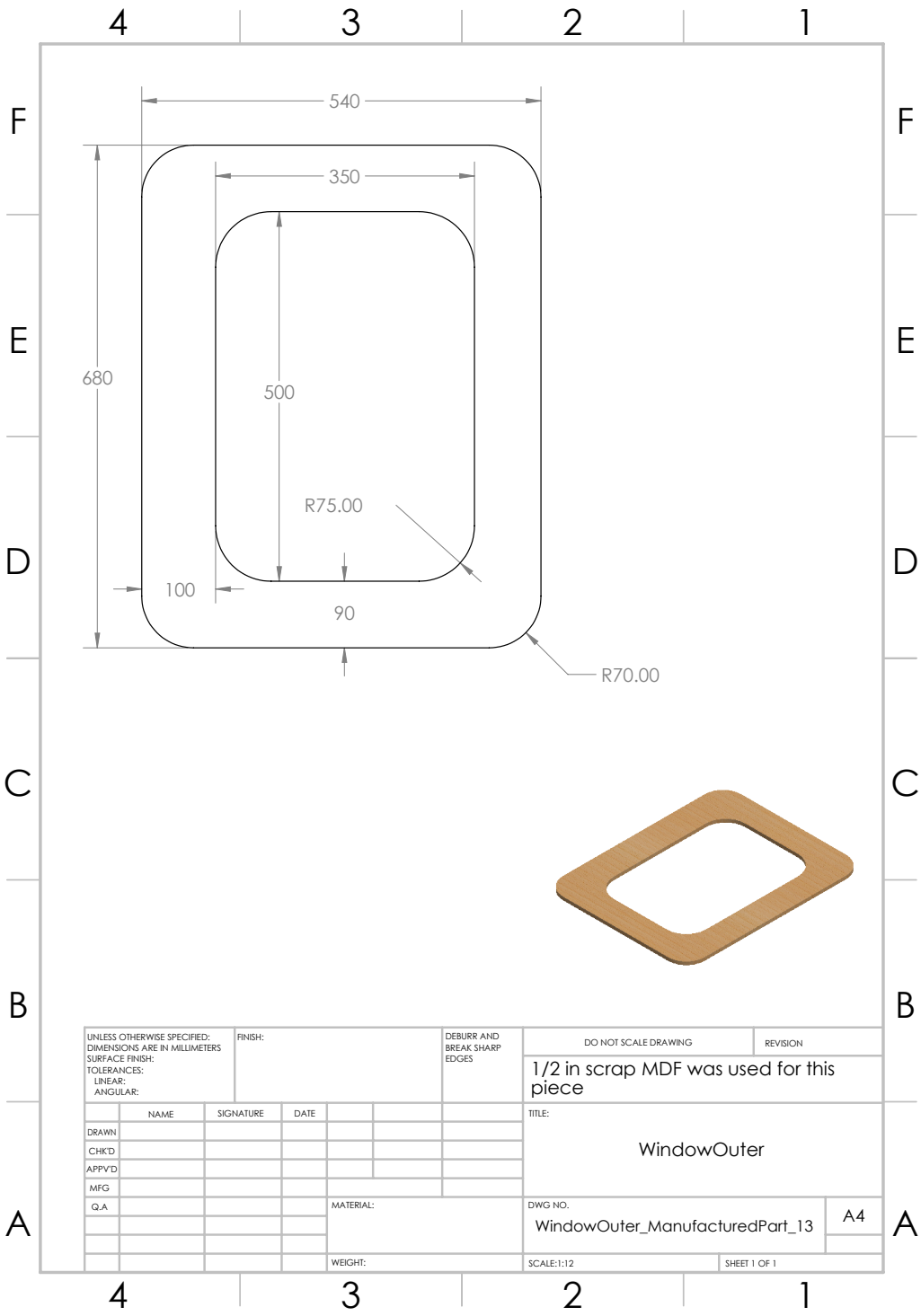

Figure B.14: Window Outer Portion

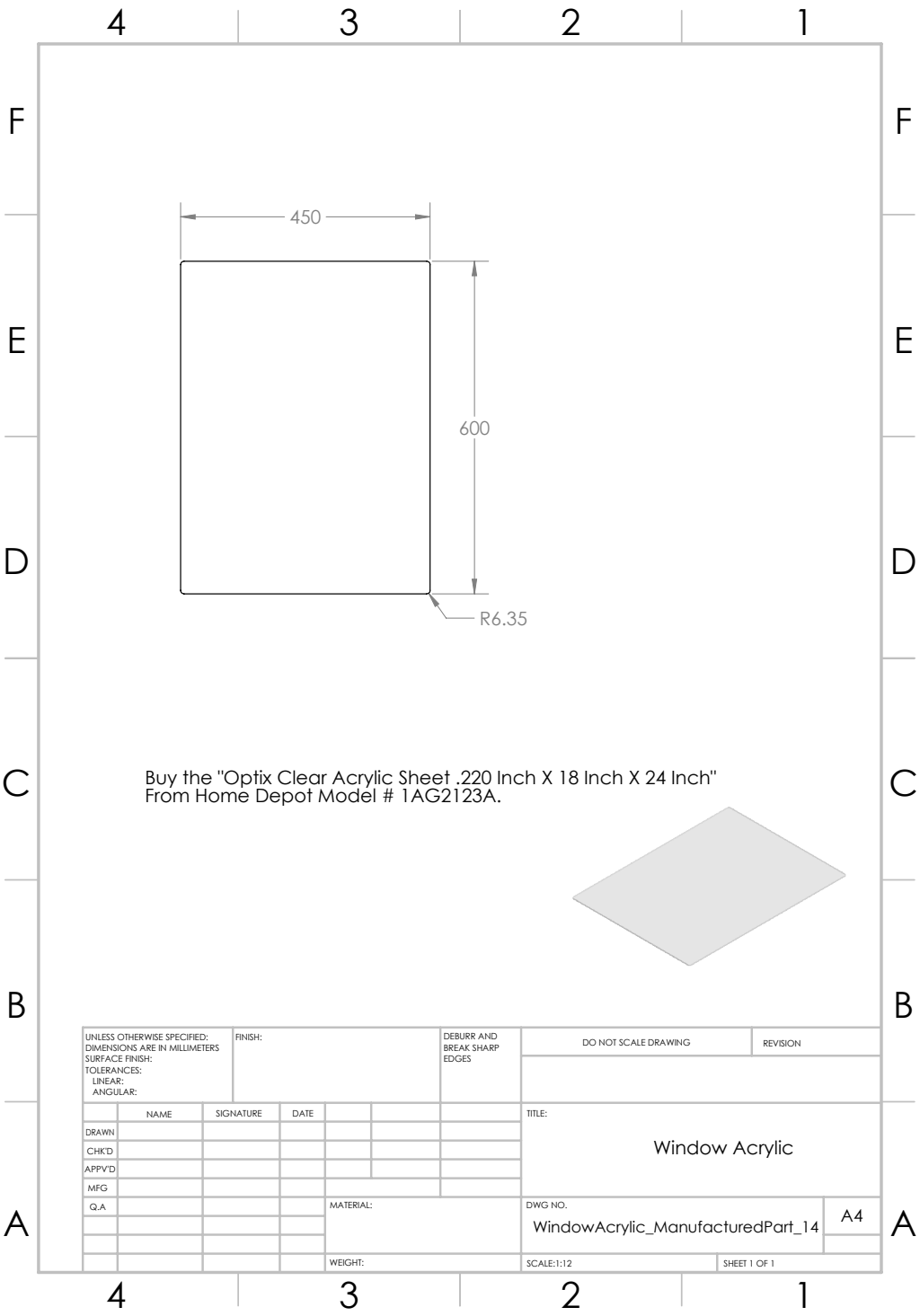

Figure B.15: Window Acrylic

B.3 Traverse Subassembly

Table B.3: Parts required to build the traverse, see Traverse_SubAssembly_04.

Quantity	Item Number	Description	Name
2	15	T inner/outer Connection Traverse	TConnectionTraverse
2	OB1170-Bundle	Nema 23 Linear Actuator Bundle-500mm	V_Slot
4	OB785	Triple L Bracket	Triple_Bracket
2	OB2671-Set	XLarge C-Beam Gantry Kit	GantryPlateXL
16	OB750-Pack	M5X20 Low Profile Screws	M5X20
6	OB20-pack	M5X25 Low Profile Screws	M5X25
1	16	Support for ceiling pieces	Shim
2	MT21.1225	M8x80 SHCS and nuts	M8x80 SHCS

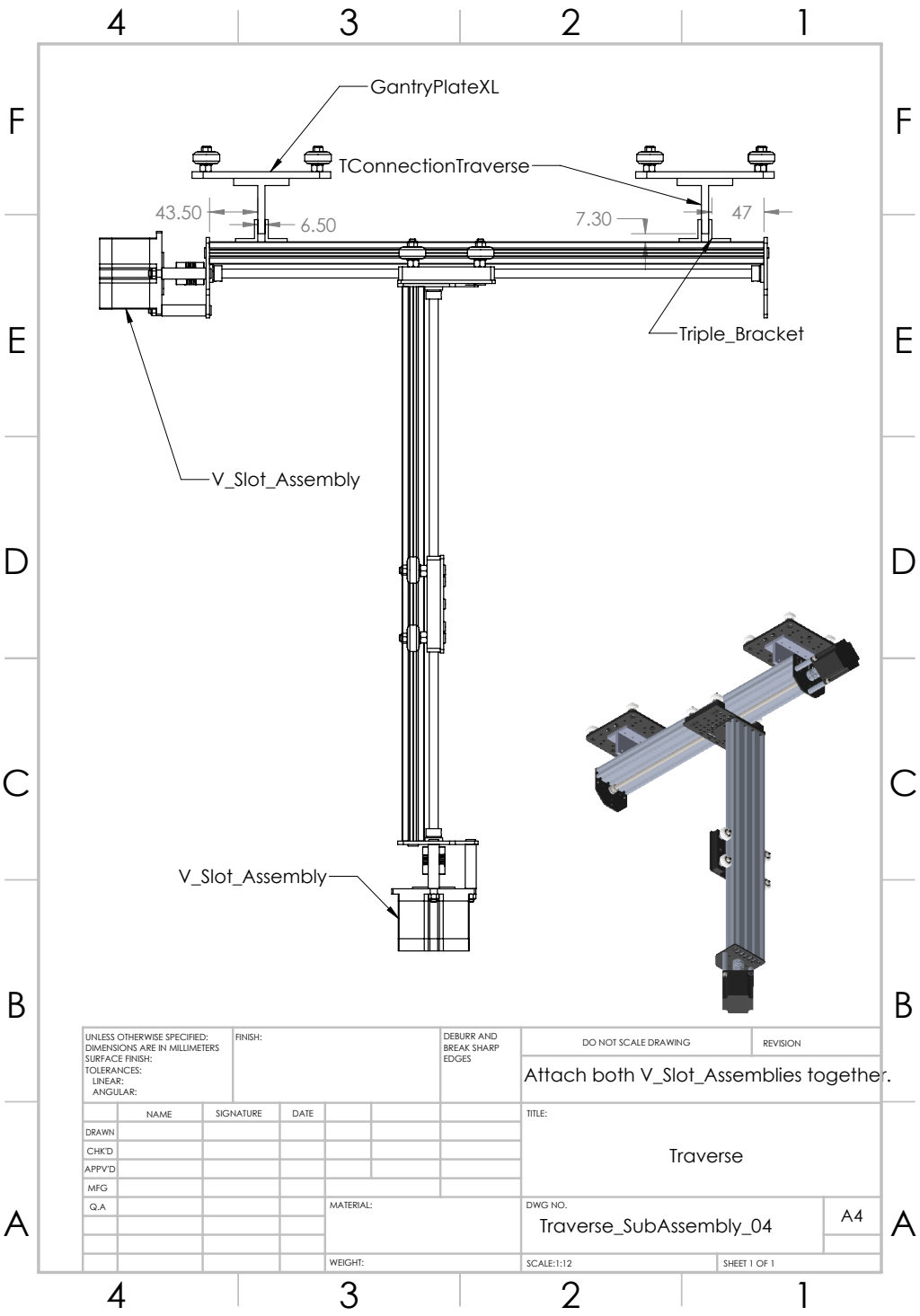

Figure B.16: Traverse Subassembly

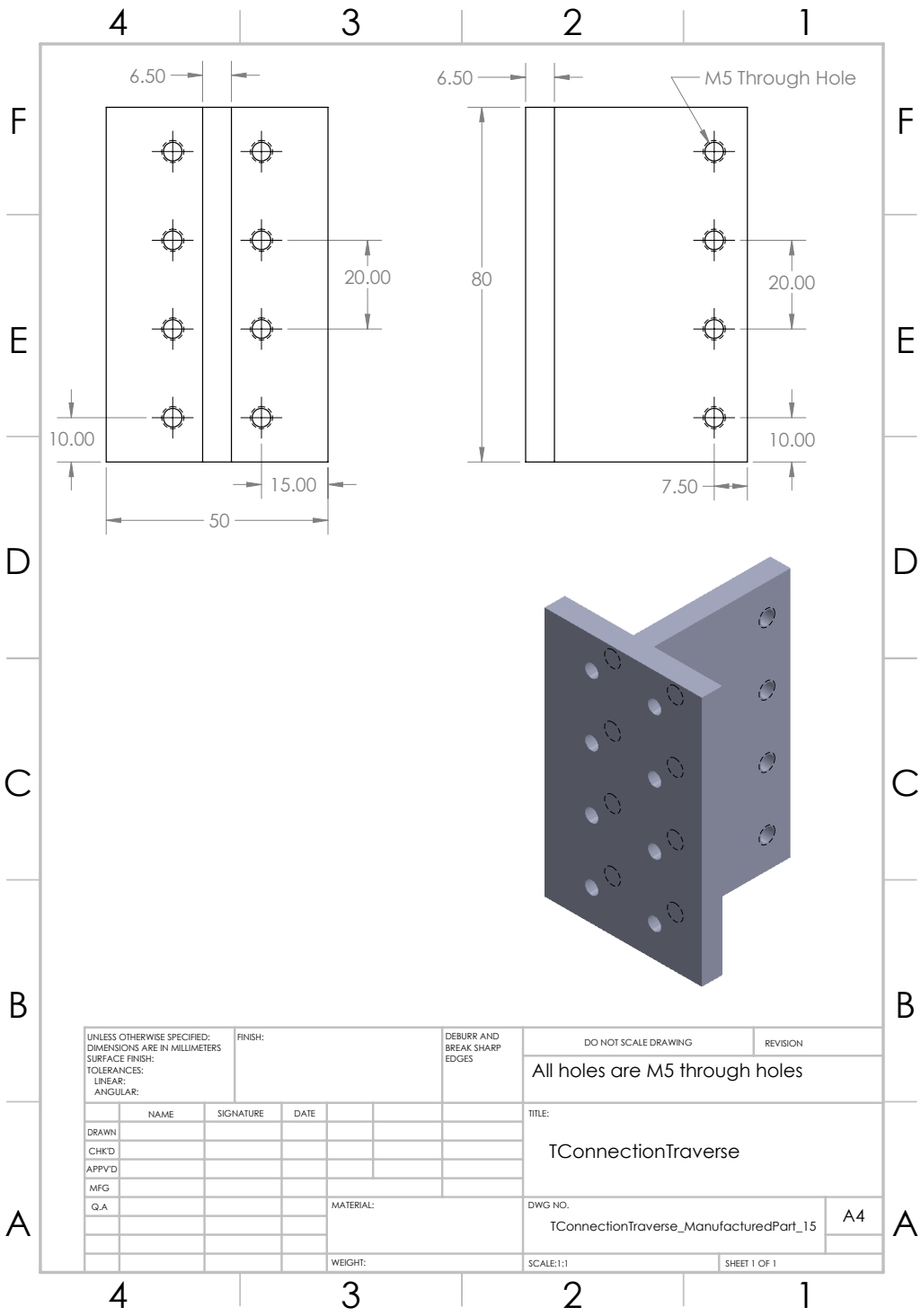

Figure B.17: T inner/outer connection traverse

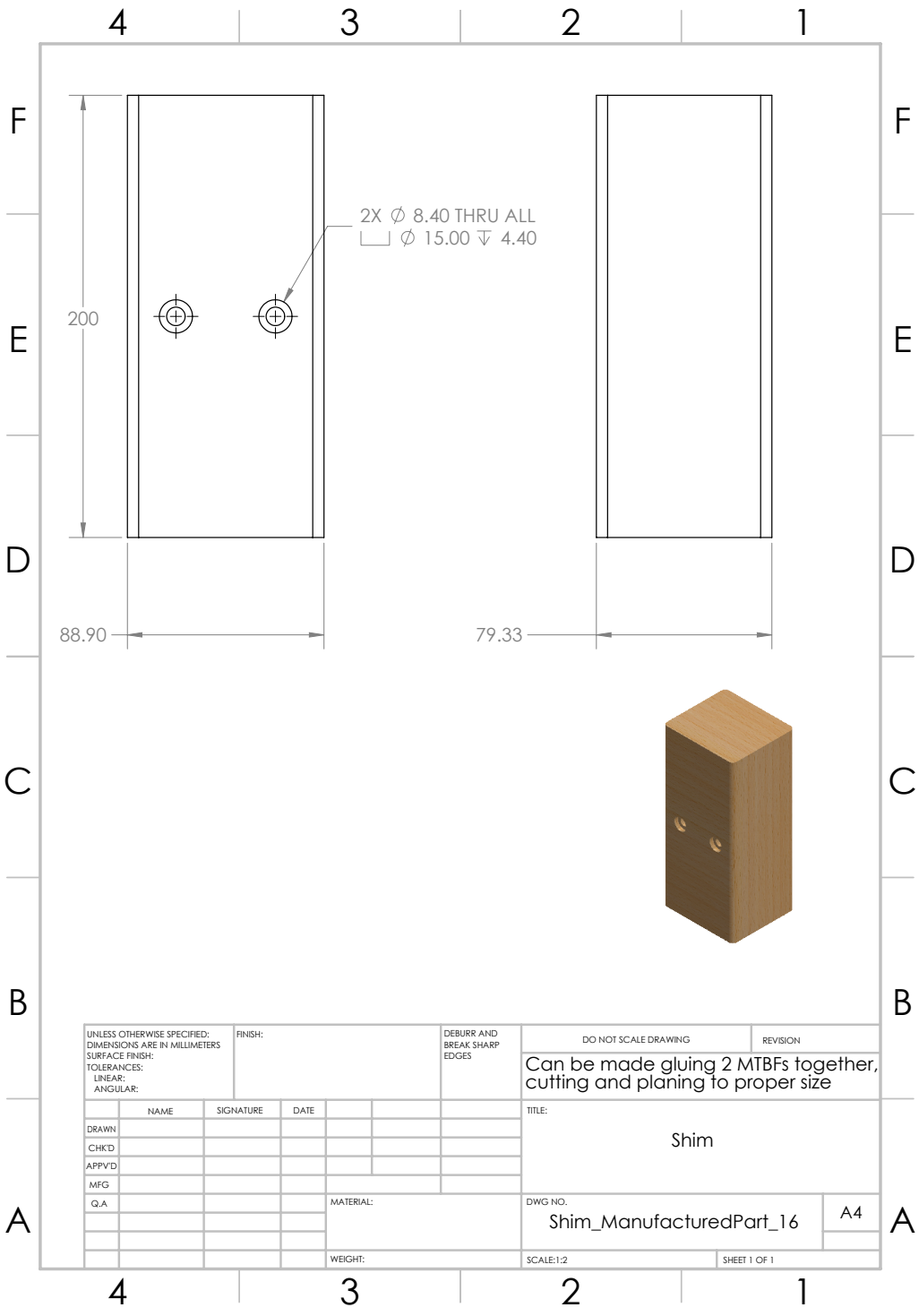

Figure B.18: Shim to support the ceiling pieces.

B.4 Wind Tunnel Assembly Instructions

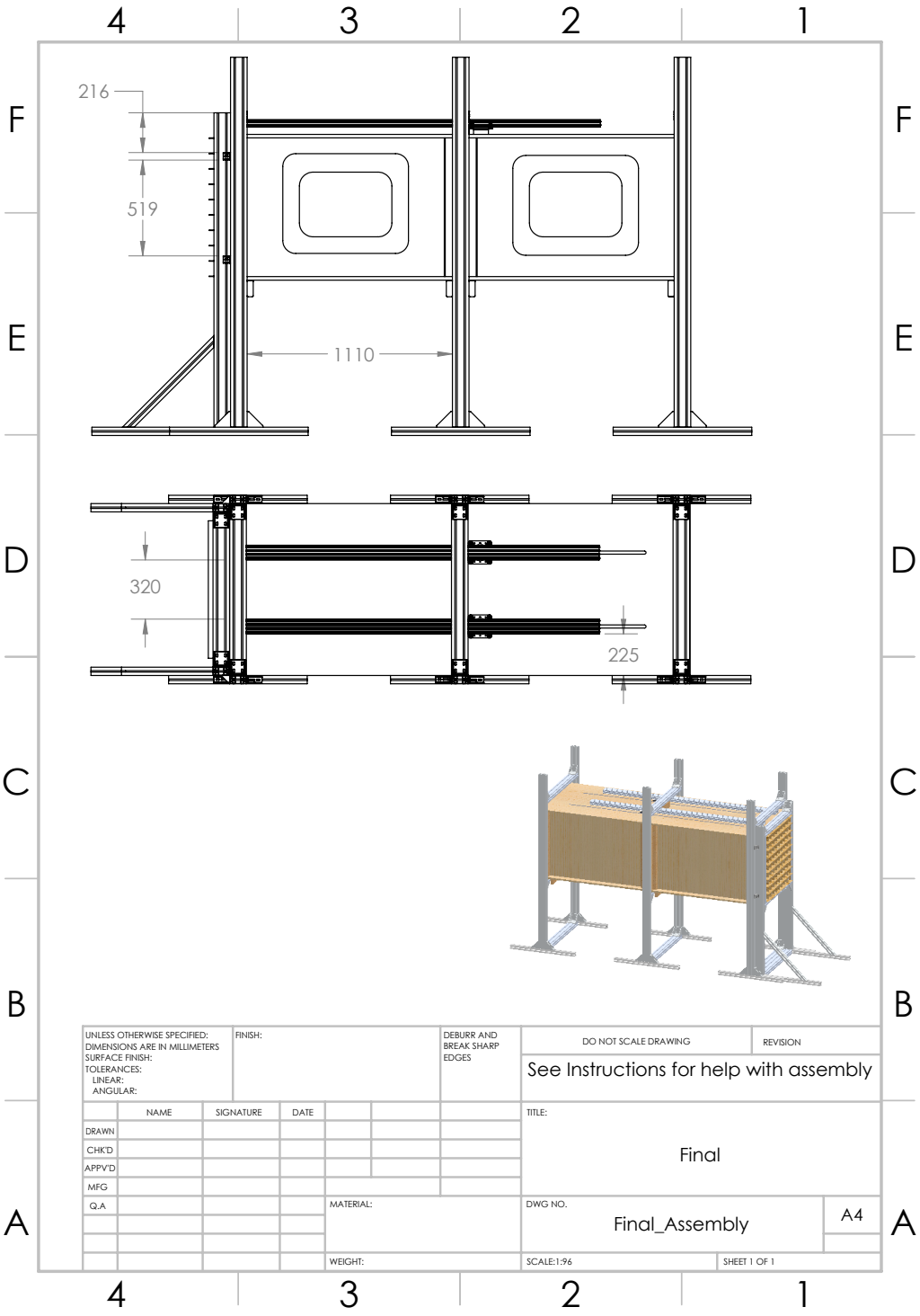

Figure B.19: Final Assembly

Wind Tunnel Construction Instructions

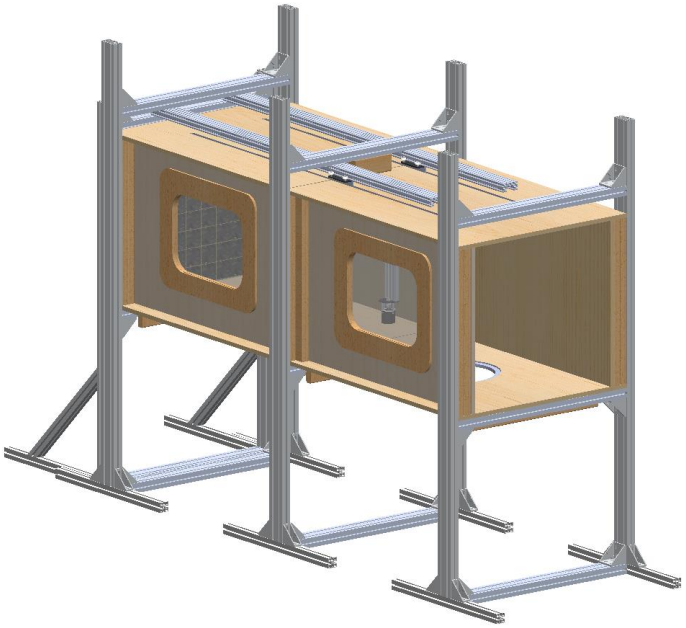

Frame Subassembly

1) Attach two ShortBeam750MM(Short Beam) to one MediumBeam930MM(Medium Beam). The Short Beam should be slid onto the POWER LOCK SF's(Power Lock) that are already attached to the Medium Beam, two Power Locks per side. Ensure the set screw of the Power Locks are accessible.

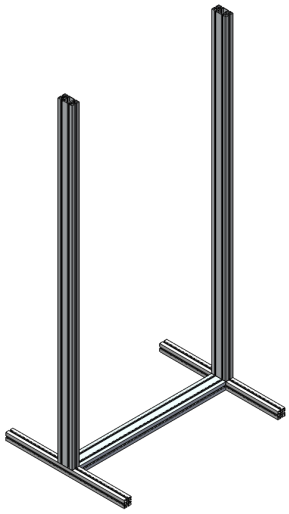

2) Attach two LongBeam2000MM(Long Beam) to the Short beams on the base. Two Power Locks should be attached to the bottom of each of the long beams. Note, since the long beams are not supported, they will likely be unstable; tilt the base from the previous step on its side so the long beam can be almost parallel to the ground during the installation.

3) Attach two ANGLE 90 brackets and four ANGLE 90X45 GD-Z brackets as shown. The nuts and bolts are M8 and are included with the brackets

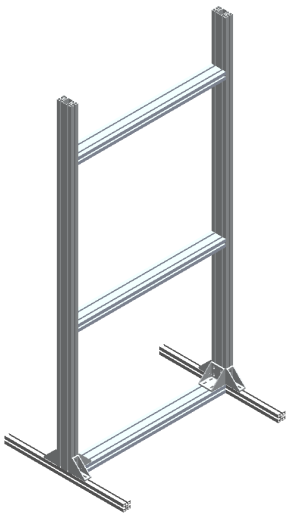

4) Slide two more Medium Beams from the top, also with power locks. On the middle Medium Beam, ensure the power locks are facing downwards and the power locks on the uppermost medium beam are facing upwards. See Frame_SubAssembly_01 technical drawing for spacing of Medium Beams.

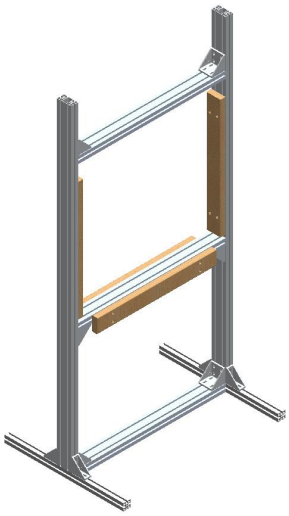

5) Attach four of the 90 ANGLE brackets as shown. Note that the top Medium Beam could be slid higher up during assembly to allow for easier installation of the Box assembly. Four of the MTBF(M2-by-4) must be attached as shown. The M8X40 SHCS and nuts should be used to attach the M2-by-4s to the frame. The two M2-by-4s attached to the center Medium Beam should be flush with the top of this beam; these M2-by-4s are to be used as anchors to attach the floor of the box assembly to the frame using wood screws.

Tunnel Footprint

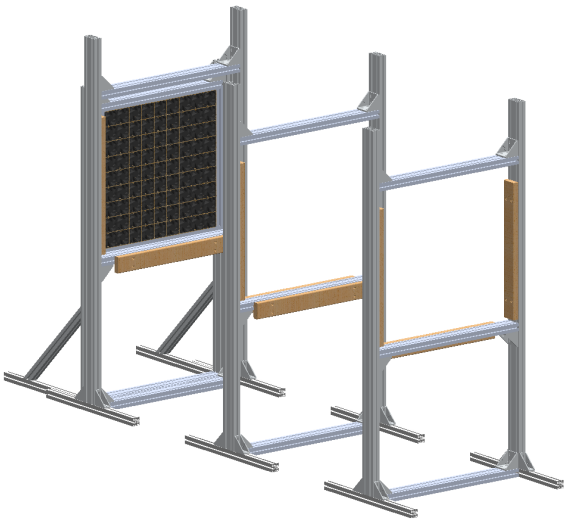

6) Construct three of the Frame subassemblies and place them in front of the wind tunnel as shown, refer to the Final_Assembly document for spacing dimensions. Note that only 3 M2-by-4s are required for the fames closest and furthest to the fan wall. The fan wall will fit exactly inside the short beams of the frame assembly. Four of the ANGLE 45 GD-Z brackets should be used to secure the fan wall to the closest frame, see image below.

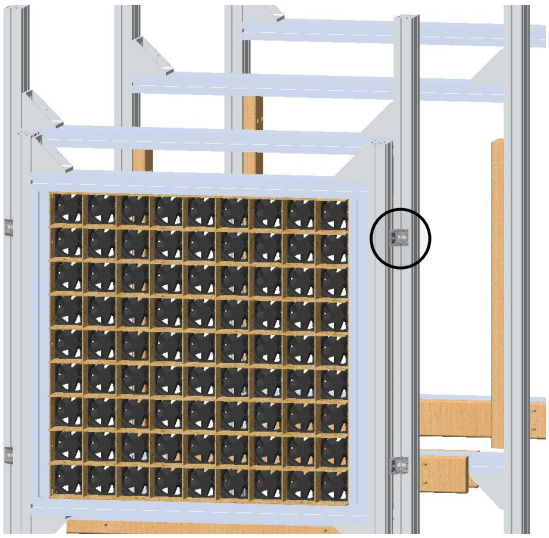

Box Subassembly

7) Place the Floor and/or Floor* pieces on top of the center Medium Beams. There should be no space between the vertical M2-by-4s and the Floor pieces. Do not screw down the Floor pieces until the walls are installed.

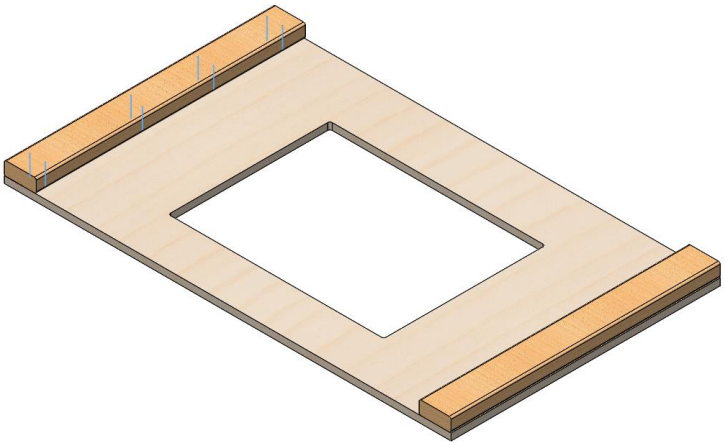

8) The Wall and Wall* pieces should be prepared as shown. A RTBF (R2-by-4) should be aligned with the edge of the Wall piece and screwed down using 8 2in. wood screws (see blue line in photo). A total of 8 R2-by-4s are required for the 2 Wall* and 2 Wall pieces, as well as 64 2in wood screws.

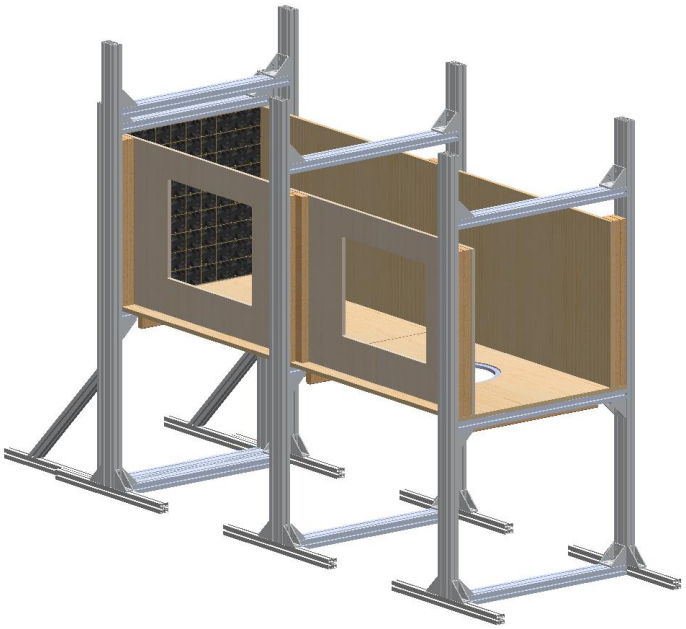

9) The prepared Wall and Wall* pieces can now be added. The R2-by4s should be screwed into the M2-by-4s using the 2in. wood screws.

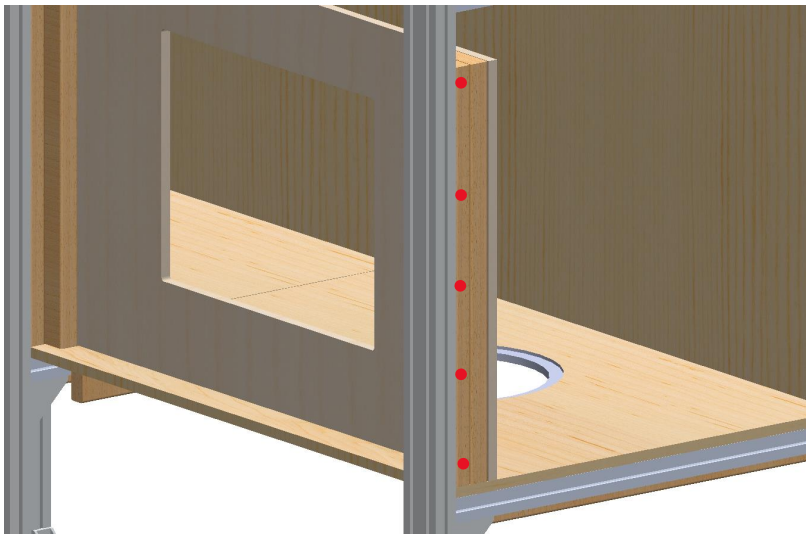

10) Five 2in. wood screws should be used in the positions illustrated by the red dots above. The screws must be driven in at an angle to securely attach the R2-by-4 and the M2-by-4 together.

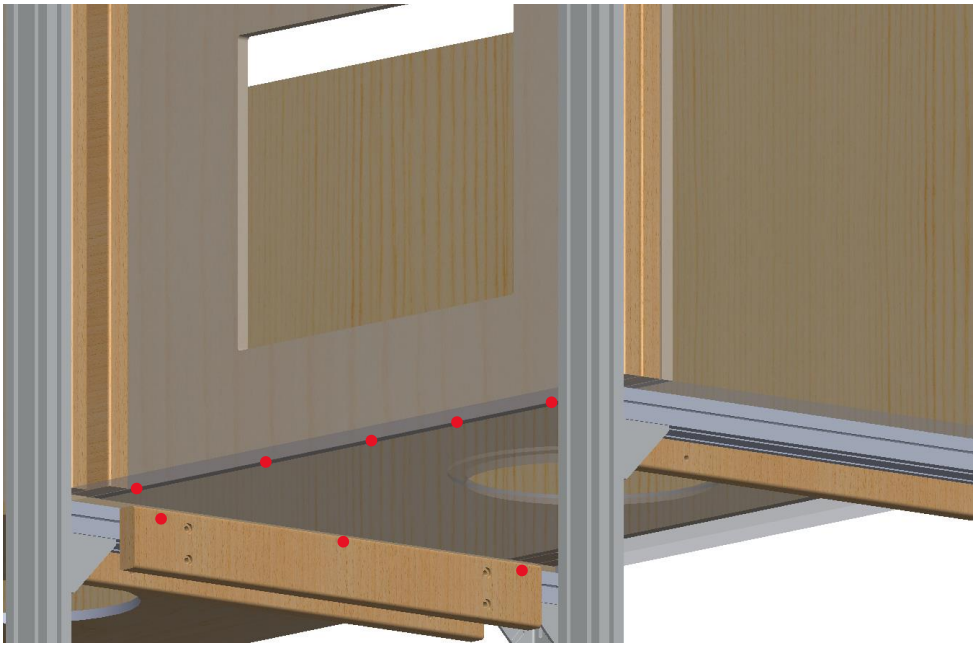

11) The Floor piece should now be fastened to the Wall pieces. The bottom view of the assembly uses a transparent floor to illustrate where to put the 1 in. screws, illustrated again by red dots. From the bottom, each screw should be driven into the Floor and the bottom edge of the Wall pieces. Pilot holes should be drilled prior to driving in the screws to avoid splitting the MDF. The floor itself should be secured to the bottom M2-by-4s of the frame assembly using 1 in. screws, also shown above using red dots.

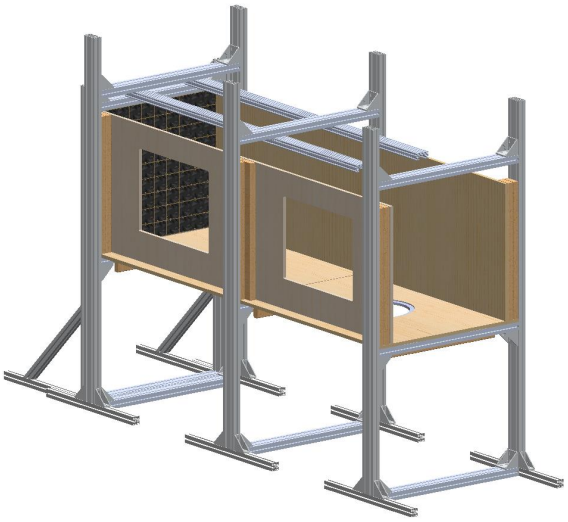

12) The two C_Beam(C-Beams) pieces should now be secured to the upper Medium Beams of the two closest frames to the fan wall. Four CBeamMount(C-Mounts) pieces should be used to mount each C-Beam. Each C-Mount uses 3 M5s and nuts to attach to the C-Beam and 2 M8s and nuts to attach to the bottom of the upper Medium Beam.

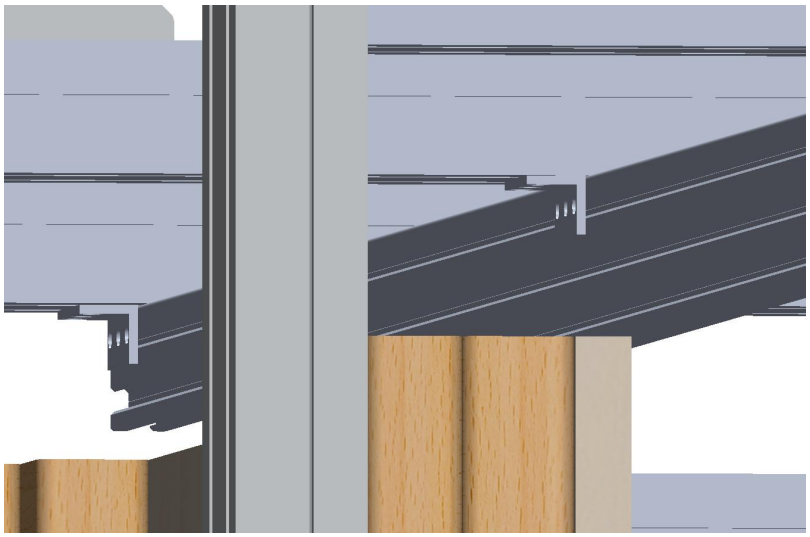

13) The end of the C-Beam should be flush with the uppermost Medium Beam closest to the fan wall.

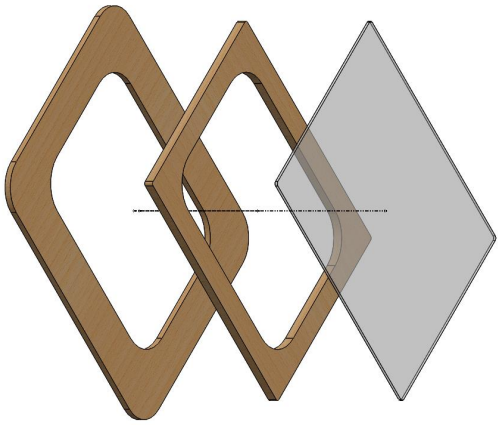

14) For the assembly of the window refer to Window_SubAssembly_03. The outer edges of the WindowAcrylic should be aligned with the outer edges of WindowSeal then the two pieces should be glued together using wood glue. The inner edges of the windowSeal should align with the inner edges of WindowOuter. Once all 3 pieces are glued together clamps should be used for 24 hours to allow the glue to set. The EPDM Foam Rubber Seal should be attached around the edge of the WindowSeal before installation.

Traverse Subassembly

15) Attach the two V_Slot linear rails together, by bolting the end plate of one V_Slot to the carriage of the other. The lead screw will protrude out of the end plate so the lead screw will need to be cut so it is flush with the outer edge of the end plate. Only 3sets of M5 bolts, spacers and nuts are needed to attach the two V_Slots together.

16) Four Triple_Brackets are positioned on the top of the horizontal V_Slot. See Traverse_SubAssembly_04 for spacing dimensions.

17) Two TConnectionTraverse(T-Connection) pieces can now be place in between each pair of Triple_Brackets. 3 sets of 5X20 bolts and nuts should be used to attach each T-Connection to the Triple_Brackets. The GantryPlateXL is then attached to each T-Connection using 4 sets of M5X25 bolts and nuts.

Final Assembly

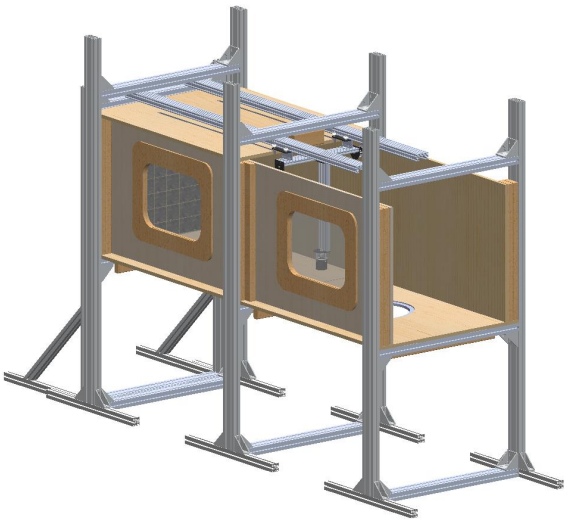

18) The first Ceiling piece can now be slid into place. Note that the center third of the Ceiling separated by the slots will deform if it is not supported. A spare 2-by-4 can be used to support the middle of the ceiling while construction is finished.
19) The Shim piece should be attached to the bottom of the upper Medium Beam using M8X80 bolts and nuts.
20) The Traverse should now be slid onto the C-Beams BEFORE the 2nd ceiling piece is installed.
21) The Windows can now be attached to the Wall pieces. Two Latches are used per Window.

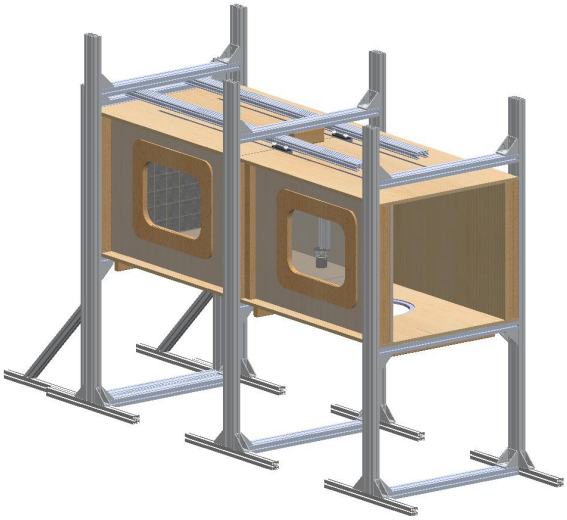

22) The second Ceiling can now be slid into place. The middle of this ceiling should also be supported so it does not deform. Both ceiling pieces should now be fastened to the Shim using 1in. wood screws. The Ceiling pieces can now be fastened to the top edge of the Walls using the same screw pattern used in step 11), this time driving the screws from the top down.

Appendix C

MATLAB Codes

C.1 Post Processing of Velocity Data, "PostProcessing.m"

```
clc;close all;clear;
```

EXTRACTION OF TURBULENCE PROPERTIES FROM HOT-WIRE DATA SETS

A. L'Ecuyer & J. Nedic

September 2021

Post processing of data to extract the main turbulence properties from hot-wire measurements. This code is specifically designed to analyze the turbulence data from one x-wire data set

==========

```
    runtime     = 60;                       %sixty second data sets
    corr_tol    = 10^-5;
    nu          = 1.5*10^-5;                % Viscosity of air [m^2/s]
    sf          = 75000;                    % Sampling Frequency [Hz]
    ff          = 30000;                    % Analogue low pass filter frequency [Hz]
    kf          = 1.3;                      % At what f_eta to apply the digital filter

%Do analysis on all .mat data in a specified folder
%ask User to select File
    myFolder = uigetdir(cd);
% Check to make sure that folder actually  exists.  Warn user if it doesn't.
if ~isfolder(myFolder)
    errorMessage = sprintf('Error: The following folder does not exist:\n%s\nPlease specify a new
folder.', myFolder);
    uiwait(warndlg(errorMessage));
    myFolder = uigetdir();  Ask for a new one.
    if myFolder == 0
         % User clicked Cancel
         return;
    end
end
%Determine number of data sets in folder
filePattern = fullfile(myFolder, '*.mat'); % Change to whatever pattern you need.
theFiles = dir(filePattern);
for k = 1 : length(theFiles)
```

```
    baseFileName = theFiles(k).name;
    fullFileName = fullfile(theFiles(k  ).folder, baseFileName);
    % Now do whatever you want with this file name,
    % such as reading it in as an image array with imread()
    xPos(k) = str2num(extractBefore(extractAfter(fullFileName,'xpos='),'_'));
    yPos(k) = str2num(extractBefore(extractAfter(fullFileName,'ypos='),'_'));
    zPos(k) = str2num(extractBefore(extractAfter(fullFileName,'zpos='),'_'));
    dat(k) = str2num(extractBefore(extractAfter(fullFileName,'dat'),'.'));
end

%Initalize variables
MaxNumberOfPositions=max(xPos)*max(yPos)*max(zPos);

Lint_u1=zeros(MaxNumberOfPositions,runtime);
ZZ1=zeros(MaxNumberOfPositions,runtime);

Lint_v1=zeros(MaxNumberOfPositions,runtime);
ZZ2=zeros(MaxNumberOfPositions,runtime);
MaxNumFiles=max(xPos)*max(yPos)*max(zPos)*max(dat);
pos=1:MaxNumFiles;

%Folder where data will be saved
status = mkdir(strcat(myFolder,'\ProcessedData'));

%Different cases of planar and stream wise data sets
%create the correct position variable
if max(yPos)==17
    if max(xPos)==5
        pos=[-160:20:160 -160:20:160 -160:20:160 -160:20:160 -160:20:160]; %[mm]
    end
    if max(xPos)==3
        pos=[-160:20:160 -160:20:160 -160:20:160]; %[mm]
    end
end

if max(zPos)==19
    if max(xPos)==5
        pos=[-100:20:260 -100:20:260 -100:20:260 -100:20:260 -100:20:260]; %[mm]
    end
    if max(xPos)==3
        pos=[-100:20:260 -100:20:260 -100:20:260]; %[mm]
    end
end
if max(zPos)==1 && max(yPos)==1
    if max(xPos)==24
        pos=[550:50:1700]; %[mm]
    end
    if max(xPos)==25
        pos=[550:50:1750]; %[mm]
    end
    if max(xPos)==35
        pos=[50:50:1750]; %[mm]
    end
end
```

```
if max(zPos)==19
    pos=[linspace(-100,260,19) linspace(-100,260,19) linspace(-100,260,19) linspace(-100,260,19)
linspace(-100,260,19)]; %[mm]
end

if max(yPos)==17
    pos=[linspace(-160,160,17) linspace(-160,160,17) linspace(-160,160,17) linspace(-160,160,17)
linspace(-160,160,17)]; %[mm]
end

%initalize couunters
k=1;
h=1;
for i=1:max(xPos)
    for j=1:max(yPos)
        for m=1:max(zPos)
            for n=1:max(dat)
```

```
 %%Take care of the order of data files

RVFileName=strcat(extractBefore(baseFileName,'__xpos='),'__xpos=',num2str(i),'_ypos=',num2str(j),
'_zpos=',num2str(m),'_dat',num2str(n),'.mat');
            fprintf(1, 'Now reading %s\n', RVFileName);
            load(strcat(myFolder,'\',RVFileName));

    %Filteer the data to remove noise
    [ut_in, vt_in, f_eta] = Post_Process_Filter(real(U),real(V),sf,ff,kf,'Recursive');


% Filter the low frequencies
    ut = ut_in;
    vt = vt_in;

  clear U V ut_in vt_in
```

---------- CROSS WIRE ----------

```
  U1_bar      =mean(ut);
  V1_bar       =mean(vt);
  up1         =ut-U1_bar;
  vp1         =vt-V1_bar;
  u1_rms(k)   =rms(up1);
  v1_rms(k)   =rms(vp1);
  uu1(k)      = mean(up1.^2);              % <uu>
  vv1(k)      = mean(vp1.^2);              % <vv>
  qq1(k)      = mean(up1.^2) + 2*mean(vp1.^2);   % Approximation for irrotational flow
  uv1(k)    = mean(up1.*vp1); % <uv>

   U1(k)       = mean(ut);
   V1(k)       = mean(vt);
```

---------- BLOCK INTEGRAL SCALE ----------

```
%Calculate 60 integral scales, one per 1 second time interval
%create .gif file of all 60 autocorrelation curve fits
jif = figure('Visible', 'off');
axis tight manual % this ensures that getframe() returns a biltwellconsistent size
filename = strcat('Autocorrelation at pos X=',num2str(550+50*(i-1)),'.gif');
SS=1;
h=1;
%runtime=10;
clear u_temp v_temp
u_temp=reshape(ut,[],runtime);
v_temp=reshape(vt,[],runtime);


 for SS=1:runtime
            [corr1,lag1]=autocorr((u_temp(:,h)-mean(u_temp(:,h))),10000);
            dt=1/sf;
            tau=lag1.*dt;
            tt1=tau.*mean(u_temp(:,h));

            [xData, yData] = prepareCurveData( tt1, corr1 );
            % Set up fittype and options.
                ft = fittype( 'exp(-b*x)', 'independent', 'x', 'dependent', 'y' );
                opts = fitoptions( 'Method', 'NonlinearLeastSquares' );
                opts.Algorithm = 'Levenberg-Marquardt';
                opts.Display = 'Off';
                opts.Robust = 'LAR';
                opts.StartPoint = [0.312655871482597];
            % Fit model to data.
            [AutoCorrFit, ~] = fit( xData, yData, ft, opts );
            coefficientValuesU = coeffvalues(AutoCorrFit);
            b1=coefficientValuesU(1);
            Lint_u1(k,h)= 1/b1;

            %CreateGif
            plot(tt1,corr1)
            hold on
            plot(tt1, AutoCorrFit(tt1))
            ylabel({'$r(\tau)$'},'Interpreter','latex','FontSize',16);
            xlabel({'$\tau$'},'Interpreter','latex','FontSize',16);
            title(strcat('Autocorrelation at pos X=',num2str(500+50*i),'--',num2str(SS),'out of
',num2str(runtime)))
            hold off
            drawnow
             % Capture the plot as an image
              frame = getframe(jif);
              im = frame2im(frame);
              [imind,cm] = rgb2ind(im,256);
              % Write to the GIF File
              if h == 1
                   imwrite(imind,cm,filename,'gif', 'Loopcount',inf);
              else
```

```
                imwrite(imind,cm,filename,'gif','WriteMode','append');
            end

            % NOW REPEAT EVERTHING for V1 component
            [corr2,lag2]=autocorr((v_temp(:,h)-mean(v_temp(:,h))),10000);
            [xData2, yData2] = prepareCurveData( tt1, corr2 );
            % Set up fittype and options.
                ft2 = fittype( 'exp(-b*x)', 'independent', 'x', 'dependent', 'y' );
                opts2 = fitoptions( 'Method', 'NonlinearLeastSquares' );
                opts2.Display = 'Off';
                opts2.StartPoint = [0.312655871482597];
            % Fit model to data.
            [AutoCorrFit2, ~] = fit( xData2, yData2, ft2, opts2 );
            coefficientValuesV = coeffvalues(AutoCorrFit2);
            b2=coefficientValuesV(1);
            Lint_v1(k,h)= 1/b2;
            %Increase counter
             h=h+1;
             clear corr1 corr2 tt1 tt2
 end
```

---------- DerivativeComponents ----------

```
        %2nd order spacial derivates estimated from the velocity
        %time series.
        [dudx1, dduu1] = finite_diff(ut,ut,sf,9);
        [dvdx1, ddvv1] = finite_diff(vt,ut,sf,9);
        %Use a correction method proposed by Burattini (2008)
        [dudx2_c, dvdx2_c,r11,
r21]=Burattini_XW_correction(0.8838/1000,1.25./1000,U1(k)./sf,dduu1,ddvv1);
        ddux_1(k) = mean(dduu1);
        ddvx_1(k) = mean(ddvv1);
```

---------- KOLMOGOROV SCALES ----------

HIT approximation

```
        epsiso1         =   15 * 0.00001568 * mean(dudx2_c);
        eps_iso1(k)    =   epsiso1;
        % XW approximation
        epsxw1          =    3 * 0.00001568 * (mean(dudx2_c) + 2*mean(dvdx2_c));
        eps_xw1(k)     =    epsxw1;
        %Use XW approximation
        eta1(k)        = (0.00001568^3./epsxw1).^(0.25);
        t_eta1(k)      = sqrt(0.00001568./epsxw1);
        u_eta1(k)      = real((0.00001568.*epsxw1).^(0.25));
```

---------- TAYLOR SCALES ----------

```
        lambdaiso1        = sqrt((15.*0.00001568.*mean(up1.^2))./epsxw1);
        lambda_iso1(k)    = lambdaiso1;
```

```
        Re_lambda_iso1(k) = (sqrt(qq1(k)./3).*lambdaiso1)./0.00001568;
        lambda_v1(k)      = sqrt((15.*0.00001568.*mean(vp1 .^2))./epsxw1);
```

---------- DISSIPATION COEFFICIENT ----------

```
        LU1 = mean(Lint_u1(k,:));
        Ceps_iso1(k) = (epsxw1.*LU1) ./((qq1(k)./3).^1.5);

        Ceps_iso1_McFadden(k) = (epsxw1.*LU1_McFadden) ./(qq1(k)./3).^1.5;
        f_eta1(k)  = U1_bar ./(2*pi*(0.00001568^3./epsxw1).^(0.25));

        dudt=mean(finite_diff_time(ut,sf).^2);
        lambda_Estimation(k)=(mean(ut).^2.*qq1(k)./(3.*(dudt))).^0.5;
        eps_Estimation(k)=10.*0.00001568.*qq1(k)./3./lambda_Estimation(k).^2;
        Ceps_Estimation(k) = (eps_Estimation(k).*LU1)./((qq1(k)./3).^1.5);
```

---------- Spectra Data ----------

```
        Cross_Correlation(k)=corr(ut,vt);
```

---------- PDF DATA ----------

```
          ut_T=Stat_Analyze(ut);

[~,u_var(k),u_Skewness(k),u_Kurtosis(k),u_Super_Kurtosis(k),u_Hyper_Kurtosis(k)]=Stat_Analyze(ut)
;

[~,dudx1_var(k),dudx1_Skewness(k),dudx1_Kurtosis(k),dudx1_Super_Kurtosis(k),dudx1_Hyper_Kurtosis(
k)]=Stat_Analyze(dudx1);

[~,v_var(k),v_Skewness(k),v_Kurtosis(k),v_Super_Kurtosis(k),v_Hyper_Kurtosis(k)]=Stat_Analyze(vt)
;

[~,dvdx1_var(k),dvdx1_Skewness(k),dvdx1_Kurtosis(k),dvdx1_Super_Kurtosis(k),dvdx1_Hyper_Kurtosis(
k)]=Stat_Analyze(dvdx1);
          %Increase counter
            k=k+1;
```

```
            end
        end
    end
end
%Save data as two files. Seperated into non-PDF intformation and PDF
%information.
 save_name=strcat('PROCESSED_',extractBefore(baseFileName,'__xpos'),'.mat');
 save(strcat(myFolder,'\ProcessedData\',save_name), 'pos', 'Ceps_iso1','ddux_1', 'ddvx_1',
'eps_iso1', 'eps_xw1','eta1','f_eta1', 'lambda_iso1','lambda_v1',...
     'Lint_u1','Lint_v1','ZZ1','ZZ2','qq1','Re_lambda_iso1','t_eta1','U1','V1','u1_rms','v1_rms',
'u_eta1','uu1','uv1','vv1','Cross_Correlation','Ceps_Estimation')

 save_name2=strcat('PDF_',extractBefore(baseFileName,'__xpos'),'.mat');
```

```
 save(strcat(myFolder,'\ProcessedData\',save_name2), 'pos',...
 'u_var','u_Skewness','u_Kurtosis','u_Super_Kurtosis','u_Hyper_Kurtosis',...
 'dudx1_var','dudx1_Skewness','dudx1_Kurtosis','dudx1_Super_Kurtosis','dudx1_Hyper_Kurtosis',...
 'v_var','v_Skewness','v_Kurtosis','v_Super_Kurtosis','v_Hyper_Kurtosis',...
 'dvdx1_var','dvdx1_Skewness','dvdx1_Kurtosis','dvdx1_Super_Kurtosis','dvdx1_Hyper_Kurtosis');

%Create graphs for quick data analysis
newBaseFileName=extractAfter(extractBefore(baseFileName,'__xpos='),'Velocity_');

close all
figure
scatter(pos,U1)
grid on
title(strcat('Mean Velocity'))
ylabel({'Velocity $[\frac{m}{s}]$'},'Interpreter','latex','FontSize',16);
% ylabel({'Streamwise Direction $[mm]$'},'Interpreter','latex','FontSize',16);
xlabel({'Streamwise Direction $[mm]$'},'Interpreter','latex','FontSize',16);
hold on
scatter(pos,V1)
leg0 = legend('$\bar{U}$','$\bar{V}$');
set(leg0,'Interpreter','latex');
set(leg0,'FontSize',16);
%  xlim([5 6])
% ylim([-1 3.5])
savefig(strcat(myFolder,'\ProcessedData\','Mean Velocity_',newBaseFileName,'.fig'))
close

figure
scatter(pos,u1_rms./U1)
grid on
hold on
scatter(pos,v1_rms./U1)
grid on
title(strcat('Turburlence Intensity'))
ylabel({'$I_{x},I_{y}$'},'Interpreter','latex','FontSize',16);
xlabel({'Streamwise Direction $[mm]$'},'Interpreter','latex','FontSize',16);
%
legend({'$\frac{u_{rms}}{\bar{U}}$'},'Interpreter','latex','FontSize',16,{'$\frac{v_{rms}}{\bar{U
}}$'},'Interpreter','latex','FontSize',16)
leg1 = legend('$\frac{u_{rms}}{\bar{U}}$','$\frac{v_{rms}}{\bar{U}}$');
set(leg1,'Interpreter','latex');
set(leg1,'FontSize',16);
savefig(strcat(myFolder,'\ProcessedData\','Turburlence Intensity_',newBaseFileName,'.fig'))
close

figure
scatter(pos,Ceps_iso1)
hold on
scatter(pos,Ceps_Estimation)
grid on
title(strcat('Dissipation'))
ylabel({'$C_\epsilon$'},'Interpreter','latex','FontSize',16);
xlabel({'Streamwise Direction $[mm]$'},'Interpreter','latex','FontSize',16);
```

```
savefig(strcat(myFolder,'\ProcessedData\','Dissipation_',newBaseFileName,'.fig'))
close

figure
scatter(pos,Cross_Correlation)
grid on
title('Correlation')
ylabel({'$\rho(u,v)$'},'Interpreter','latex','FontSize',16);
xlabel({'$Streamwise Direction$'},'Interpreter','latex','FontSize',16);
savefig(strcat(myFolder,'\ProcessedData\','CrossCorr_',newBaseFileName,'.fig'))
close

figure
scatter(pos,Re_lambda_iso1)
grid on
title(strcat('Turbulent Reynolds Number'))
ylabel({'$Re_\lambda$'},'Interpreter','latex','FontSize',16);
xlabel({'Streamwise Direction $[mm]$'},'Interpreter','latex','FontSize',16);
savefig(strcat(myFolder,'\ProcessedData\','TurburlentReynoldsNumber_',newBaseFileName,'.fig'))
close

figure
scatter(pos,u1_rms./v1_rms)
grid on
title('Anisotropy','Interpreter','latex','FontSize',16)
ylabel({'$\frac{v_{rms}}{u_{rms}}$'},'Interpreter','latex','FontSize',16);
xlabel({'Streamwise Direction $[mm]$'},'Interpreter','latex','FontSize',16);
savefig(strcat(myFolder,'\ProcessedData\','Istropy_',newBaseFileName,'.fig'))
close

msgbox('Done')
```

Bibliography

Adkins, K., Wambolt, P., Sescu, A., Swinford, C., and Macchiarella, N. D. (2020). Observational practices for urban microclimates using meteorologically instrumented unmanned aircraft systems. Atmosphere, 11(9).

Barlow, J. B., Rae, W. H., and Pope, A. . (1999). Low-speed wind tunnel testing. John Wiley & Sons, INC., New York.

Batchelor, G. K. (1953). The Theory of Homogeneous Turbulence. Cambridge University Press, Cambridge.

Batchelor, G. K. and Townsend (1948). Decay of isotropic turbulence in the initial period. Proceedings of the Royal Society of London, 193(1035):539–558.

Bellani, G. and Variano, E. A. (2014). Homogeneity and isotropy in a laboratory turbulent flow. Experiments in Fluids : Experimental Methods and their Applications to Fluid Flow, 55(1):1–12.

Bos, W. J. (2020). Production and dissipation of kinetic energy in grid turbulence. Physical Review Fluids, 5(10):1–26.

Browne, L. W. B., Antonia, R. A., and Chua, L. P. (1988). Calibration of X-probes for turbulent flow measurements. Experiments in Fluids, 7(3):201–208.

Burattini, P. (2008). The effect of the X-wire probe resolution in measurements of isotropic turbulence. Measurement Science and Technology, 19(11):1–13.

Cao, S., Nishi, A., Kikugawa, H., and Matsuda, Y. (2002). Reproduction of wind velocity history in a multiple fan wind tunnel. Journal of Wind Engineering and Industrial Aerodynamics, 90:1719–1729.

Carter, D. W. and Coletti, F. (2017). Scale-to-scale anisotropy in homogeneous turbulence. Journal of Fluid Mechanics, 827:250–284.

Comte-Bellot, G. and Corrsin, S. (1966). The use of a contraction to improve the isotropy of grid-generated turbulence. Journal of Fluid Mechanics, 25(4):657–682.

Finn E. Jørgensen (2002). How to measure turbulence with hot-wire anemometers - a practical guide. Dantec Dynamics, Denmark.

Goldman Sachs (2018). Drones: Reporting for Work, https://www.goldmansachs.com/insights/technology-driving-innovation/drones/.

Goto, S. and Vassilicos, J. C. (2009). The dissipation rate coefficient of turbulence is not universal and depends on the internal stagnation point structure. Physics of Fluids, 21(3):1–8.

Hangan, H., Refan, M., Jubayer, C., Romanic, D., Parvu, D., LoTufo, J., and Costache, A. (2015). Novel Techniques in Wind Engineering. In ICWE 2015, 14th International Conference on Wind Engineering, Porto Alegre.

Hearst, R. J. and Lavoie, P. (2014). Decay of turbulence generated by a square-fractal-element grid. Journal of Fluid Mechanics, 741:567–584.

Ikeda, H. and Ozono, S. (2013). Homogeneous turbulence generation by non-linear interferences between disturbances in a low wavenumber range (Characteristics of turbulence by a random-phase mode). Transactions of the Japan Society of Mechanical Engineers, 79(800):555–566.

Kang, H. S., Chester, S., and Meneveau, C. (2003). Decaying turbulence in an active-grid-generated flow and comparisons with large-eddy simulation. Journal of Fluid Mechanics, 480(1):129–160.

Kolmogorov, A. N. (1941a). Dissipation of Energy in Locally Isotropic Turbulence. Akademiia Nauk SSSR Doklady, 32:15–17.

Kolmogorov, A. N. (1941b). The Local Structure of Turbulence in Incompressible Viscous Fluid for Very Large Reynolds' Numbers. Akademiia Nauk SSSR Doklady, 30:9–13.

Larssen, J. V. and Devenport, W. J. (2011). On the generation of large-scale homogeneous turbulence. Experiments in Fluids, 50(5):1207–1223.

Lavoie, P., Djenidi, L., and Antonia, R. A. (2007). Effects of initial conditions in decaying turbulence generated by passive grids. Journal of Fluid Mechanics, 585:395–420.

Makita, H. (1991). Realization of a large-scale turbulence field in a small wind tunnel. Fluid Dynamics Research, 8:53–64.

Mehta, R. D. and Bradshaw, P. (1979). Design rules for small low speed wind tunnels. The Aeronautical Journal, 83(827):443–453.

Mydlarski, L. (2017). A turbulent quarter century of active grids: From Makita (1991) to the present. Fluid Dynamics Research, 49:1–20.

Mydlarski, L. and Warhaft, Z. (1996). On the onset of high-Reynolds-number grid- generated wind tunnel turbulence. Journal of Fluid Mechanics, 320:331–368.

Nedić, J. and Tavoularis, S. (2016a). Energy dissipation scaling in uniformly sheared turbulence. Physical Review E, 93(3):1–6.

Nedić, J. and Tavoularis, S. (2016b). Measurements of passive scalar diffusion downstream of regular and fractal grids. Journal of Fluid Mechanics, 800:358–386.

Nishi, A., Kikugawa, H., Matsuda, Y., and Tashiro, D. (1997). Turbulence control in multiple-fan wind tunnels. Journal of Wind Engineering and Industrial Aerodynamics, 27(3):271–285.

Nishi, A., Kikugawa, H., Matsuda, Y., and Tashiro, D. (1999). Active control of turbulence for an atmospheric boundary layer model in a wind tunnel. Journal of Wind Engineering and Industrial Aerodynamics, 83(1-3):409–419.

Nishi, A. and Miyagi, H. (1995). Computer-controlled wind tunnel for wind-engineering applications. Journal of Wind Engineering and Industrial Aerodynamics, 54-55(C):493–504.

Nishi, A., Miyagi, H., and Higuchi, K. (1993). A computer-controlled wind tunnel. Journal of Wind Engineering and Industrial Aerodynamics, 46-47:837–946.

Ozono, S. and Ikeda, H. (2018). Realization of both high-intensity and large-scale turbulence using a multi-fan wind tunnel. Experiments in Fluids, 59(12):1–12.

Ozono, S., Nishi, A., and Miyagi, H. (2006). Turbulence generated by a wind tunnel of multi-fan type in uniformly active and quasi-grid modes. Journal of Wind Engineering and Industrial Aerodynamics, 94(4):225–240.

Pope, S. B. (2000). Turbulent flows. Cambridge University Press, Cambridge.

Simmons, L. F. G. and Salter, C. (1934). Experimental Investigation and Analysis of the Velocity Variations in Turbulent Flow. Proceedings of the Royal Society of London. Series A, 145(854):212–234.

Takamure, K. and Ozono, S. (2016). Effects of inflow conditions on the turbulence generated by multiple fans. Journal of Wind Engineering (In Japanese), 41(149):148–151.

Takamure, K. and Ozono, S. (2019). Relative importance of initial conditions on outflows from multiple fans. Physical Review E, 99(1):1–9.

Tavoularis, S. and Karnik, U. (1989). Further experiments on the evolution of turbulent stresses and scales in uniformly sheared turbulence. Journal of Fluid Mechanics, 204:457–478.

Taylor, G. I. (1935). Statistical Theory of Turbulence. Parts 1-4. Proceedings of the Royal Society of London. Series A, 151(873):421–478.

Tennekes, H. and Lumley, J. L. (1972). A First Course in Turbulence. MIT University Press, Cambridge.

Teunissen, H. W. (1975). Simulation of the planetary boundary layer in a multiple-jet wind tunnel. Atmospheric Environment, 9(2):145–174.

Valente, P. C. and Vassilicos, J. C. (2011). The decay of turbulence generated by a class of multiscale grids. Journal of Fluid Mechanics, 687:300–340.

Valente, P. C. and Vassilicos, J. C. (2014). The non-equilibrium region of grid-generated decaying turbulence. Journal of Fluid Mechanics, 744(1):5–37.

Valente, P. C. and Vassilicos, J. C. (2015). The energy cascade in grid-generated non-equilibrium decaying turbulence. Physics of Fluids, 27(4):1–25.

Variano, E. A. and Cowen, E. A. (2008). A random-jet-stirred turbulence tank. Journal of Fluid Mechanics, 604(01):1–32.

Vassilicos, J. C. (2015). Dissipation in turbulent flows. Annual Review of Fluid Mechanics, 47:95–114.

Wakamatsu, Y., Ozono, S., and Shin, B. (2019). Observation of Turbulence Field near the Inlet of the Test Section. The Proceedings of Conference of Kyushu Branch, 72:E45.

Wang, J. Y., Meng, Q. H., Luo, B., Zeng, M., and Sun, B. (2015). Multiple-fan active control wind tunnel for outdoor near-surface airflow simulation. Chinese Control Conference, CCC, pages 5959–5964.